X-RAY ABSORPTION FINE STRUCTURE MEASUREMENTS OF THE LATTICE STRAIN IN MAGNETIC ULTRATHIN FILMS

by

Moyra Kathleen Mc Manus
B.Sc., Université de Montréal, 1990
M.Sc., Université de Montréal, 1993

THESIS SUBMITTED IN PARTIAL FULFILLMENT OF
THE REQUIREMENTS FOR THE DEGREE OF

DOCTOR OF PHILOSOPHY

in the Department
of
Physics

Simon Fraser University
December, 1996

Approval

Name: Moyra Kathleen Mc Manus
Degree: Doctor of Philosophy
Title of thesis: X-ray Absorption Fine Structure Measurements of the Lattice Strain in Magnetic Ultrathin Films

Examining Committee:

Professor R.F. Frindt, Physics Department, Chairman

_____

Professor E.D. Crozier, Physics Department
Senior Supervisor

_____

Professor B. Heinrich, Physics Department

_____

Professor M. Plischke, Physics Department

_____

Associate Professor S. Watkins, Physics Department
Internal Examiner

_____

Dr. S.M. Heald, External Examiner
Pacific Northwest National Laboratories

Date Approved: 20 December 1996

PARTIAL COPYRIGHT LICENSE

I hereby grant to Simon Fraser University the right to lend my thesis, project or extended essay (the title of which is shown below) to users of the Simon Fraser University Library, and to make partial or single copies only for such users or in response to a request from the library of any other university, or other educational institution, on its own behalf or for one of its users. I further agree that permission for multiple copying of this work for scholarly purposes may be granted by me or the Dean of Graduate Studies. It is understood that copying or publication of this work for financial gain shall not be allowed without my written permission.

Title of Thesis/Project/Extended Essay

X-Ray Absorption Fine Structure Measurements of the Lattice Strain in Magnetic Ultrathin Films.

Author: Moyra K. McManus
(signature)

Moyra Kathleen McManus
(name)

19 March 1997
(date)

Abstract

Fundamental studies of epitaxial and amorphous magnetic multilayers have been driven lately by their potential applications in magnetic recording technology. The use of magnetic multilayers is affected by their giant magnetoresistance and magnetic anisotropy. A clear understanding of interfacial magnetic anisotropy rests on the structural characterisation of these multilayers which, typically, consist of two ferromagnetically coupled (F) layers separated by a non-magnetic spacer. The coupling between the F layers changes from F to antiferromagnetic depending on the thickness of the spacer. Here, two Fe/Cu/Fe systems, grown by molecular beam epitaxy (MBE), were modified by inserting Cr in the Cu. The structures were grown on a single crystal substrate of Ag(001), and have the following numbers of monolayers: 8.7Fe/3Cu/6Cr/3Cu/5Fe/10Au or 8.7Fe/3Cu/3Cr/3Cu/5Fe/10Au. The structures of the multilayers were probed using x-ray absorption fine structure (XAFS). Polarized K-edge XAFS spectra were obtained from fluorescence measurements in the total reflection geometry with the electric vector parallel to the substrate for all films and with the electric field perpendicular to the substrate for the Cu K-edge of the 3ML of Cr film. In the first sample, the Cr and upper Fe layers were shown to be tetragonally distorted from their bulk body-centered cubic (BCC) structures, their ratios of c/a being respectively 1.020(±0.012) and 1.010(±0.012). The upper Cu was found to have a body-centered tetragonal (BCT) structure

(c/a=1.024±0.012), rather than its bulk face-centered cubic (FCC) one, though its atomic volume only decreased by 0.3%. In the second sample, the upper Cu had a BCT structure with c/a=0.969±0.012, and the Cr also assumed a BCT structure.

Two simpler structures were grown in order to characterise the growth of Fe and Cr on Ag(001); the first was comprised of 5ML of Fe, the second of 10ML of Cr, both grown at room temperature and passivated with 10ML of Au. Both the Fe and the Cr showed slight tetragonal distortions from their bulk BCC lattices, with a c/a ratio of 1.012(±0.012) and 1.022(±0.012) respectively.

Two amorphous samples, with the following number of monolayers: 9Co/5Re and 5Re/3Co/9Re, were deposited by radio frequency triode sputtering on SiO_2 substrates. Both the Co and the Re were found to be oxidized. A qualitative analysis of XAFS and x-ray photoelectron spectroscopy results are given for each sample.

Acknowledgements

Of those who contributed towards this work, I'd first like to thank my supervisor, Professor Daryl Crozier for sharing his knowledge of XAFS and for his enthusiasm for the experimental process.

I would also like to note the special contributions of Professor B. Heinrich's group: thank you to Pr. Bret Heinrich for making the MBE sample growths possible, to Ken Myrtle, Zbigniew Celinski, and Maciek Kowalewski for all their help. My thanks go also to Claus Schneider for many interesting discussions.

Within the XAFS group at SFU, I would like to thank Dr. De-Tong Jiang, whose timely return to SFU made the analysis of the data interesting and fulfilling. My thanks to Andrew Seary for all his help with the programming, and to Rudolf Bauchspieß for the generous use of his programs. The help of R.J. Drociuk in the preparation of the substrates is gratefully acknowledged.

I would like to thank Professor R.W. Cochrane for providing the use of his equipment as well as for his support.

I would like to thank my supervisory committee, Pr. M. Plischke, Pr. B. Heinrich, and Pr. D. Crozier for their efforts during my stay at SFU. I thank also all the administrative staff of the Department of Physics.

And last, but far from least, thanks to Christian, Mom, Dad, Sarah, Ian and Seamus. Des gros remerciements à tous mes amis qui ont chacun à leur façon contribué à ce projet: Christian et Richard, je vous suis reconnaissante pour toutes nos discussions, merci à Shauna, Karin, Marija, et Yves.

Finally, I gratefully acknowledge the generous financial support provided by Simon Fraser University, and the NSERC grant of Professor Crozier.

Table of contents

List of Tables

Appendix A

List of Figures

Chapter V

Chapter VI

CHAPTER I: Introduction

The experimental advances of ultra-high vacuum systems, which permit the growth of epitaxial magnetic metal films, and the progress in surface science techniques have provided knowledge of the surface chemistry and crystallographic structure of films a few atomic layers thick. The ability to grow different combinations of metals on different substrates has resulted in insight as to which crystal structure is likely to result from the growth of a specific metal on a specific substrate. In the case of magnetic metals this has permitted the engineering of the magnetic properties of thin films since they have several different crystallographic structures which possess different magnetizations. Epitaxial growth mimics the effect of temperature or pressure changes in phase transitions by imposing a force on the crystal film (either compressive or tensile) at the interface between the film and the substrate. The film is then free to relax perpendicularly to the interface, which it will do unless the lattice constant of the interface happens to correspond to a crystallographic phase of minimum total energy [1]. In general, the film will grow with a strain distortion which is perpendicular to the plane of growth in order to maintain a unit cell volume close to its bulk phase and thus minimize its energy. The uniaxially strained film will grow until it attains a thickness such that it has the energy required to introduce defects or break the interface bonds and relax to its bulk structure. An example of such growth, which has been well documented, is that of a structure growing on a (001) face which yields a tetragonal unit cell: such is

the strained cubic cell of Fe grown on Ag(001). Another case of tensile strains distorting a lattice is the case of FCC Cu which grows in a BCC structure on Fe(001) according to reference [2], and in a BCT structure according to reference [3]. In this case, the strain is accommodated elastically to approximately 10 monolayers (ML).

Substrate induced lattice strain in thin film geometries results in adlayer structures which fall into a few main categories: (1) a phase where the film adopts the same lattice as the substrate (pseudomorphs), (2) a phase which is different from both the substrate and the adlayers's own bulk structure but has the same lattice parameters *a* and *b* as the substrate (commensurate reconstruction); or, the opposite, a phase where the adlayer adopts its preferred bulk structure without regard to the substrate (incommensurate reconstruction), (3) the film grows in a phase containing periodic misfit-induced defects in its structure [4]. Theoretical studies using classical continuum models of rigid substrates and adlayers predict that pseudormorphic growth can occur for lattice mismatches between the substrate and adlayer of up to 9% [5]. Other models using anharmonic potentials predict an upper limit of 13.5% lattice mismatch for the growth of one-dimensional epitaxial films [6]. Lattice mismatches induce a strain, ε, which is related, at constant temperature, to the stress in the film in the following manner:

(1.1) $\sigma=Y\varepsilon$ where Y is Young's modulus, σ is the stress [7],

and the lattice mismatch, or misfit strain, is given by

(1.2) $\varepsilon=\Delta a=\frac{a_F-a_S}{a_F}$ where a refers to the lattice parameter of the substrate (S) or film (F).

The resulting structure of the thin film will influence both its physical and chemical characteristics and thus its magnetic and electronic properties due to the strain in the film and its repercussions on the band structure.

Interest in the properties of magnetic thin films has spurred research activity in fundamental science [8] and in applications, particularly in magnetic recording technology (information storage). The identification, in 1986, of the exchange interaction between ferromagnetic films across a metallic interlayer [9] and of the "giant" magnetoresistance effect (GMR) in 1988 [10] have led to a great deal of research by companies interested in the manufacturing of magnetic heads [11].

The theoretical interpretation of anti-ferromagnetic (AF) coupling and the GMR effect are related: both are thought to be due to the propagation of spin-polarized electrons between the ferromagnetic films across the interlayer. The role of the interface is being studied for both effects. In the case of the coupling, damped oscillations were found in the strength of the coupling with increasing interlayer thickness [12]. This led to fundamental studies using a variety of combinations of transition metals. Studies of the GMR effect in materials have led to combinations which demonstrate large magnetoresistance effects at room temperature (RT) and low

magnetic fields [13], and an overall better understanding of how GMR is associated with changes in the relative orientation of the magnetizations in the successive ferromagnetic (F) layers.

The basic research executed on epitaxially grown structures soon led to the sputtered specimens which are actually used by the recording manufacturers. Though fundamental experiences relating to the properties will continue to be done on MBE grown films, for large scale production of magnetic recording heads and media the high throughput of sputtering techniques is necessary.

In this thesis the structural properties of two sets of magnetic multilayers are investigated using x-ray absorption fine structure (XAFS). The first series of samples consists of MBE grown ultrathin Fe/Cu/Cr/Cu/Fe layers and the second of radio frequency (RF) sputtered Co/Re bilayers. MBE allows the probing of structures with selected growth orientations, as well as permitting the creation of artificial phases (BCC Cu and Co) and the *in situ* characterization of surface and film structure during growth using, for example, reflection high energy electron diffraction (RHEED). RHEED oscillations give convincing evidence that it is possible to grow in a layer-by-layer mode where only one layer is growing at a time and there aren't too many holes in the underlayer, or too many atoms present on the overlayer [14]. RHEED streak splittings of Fe grown on Ag(001) at room temperature show the average minimum separation between atomic islands to be 60Å, providing in-plane information [15,16]. After deposition of one layer of Cu on this surface the Cu atomic terrace increases to that of the underlying Ag(001) indicating a separation of more than 400Å between terraces. The BCC stacking

sequence of the Cu is maintained up until 12 ML of Cu have been deposited [2,16].

The structure of the resulting films, whether they were grown by MBE or sputtering, must be characterized both in-plane, and out of plane due to the importance of the strain in all three dimensions of the films. The use of grazing-incidence x-ray scattering permits measurements of the in-plane elastic strain associated with the growth of Cu(001) on Fe(001), and Fe(001) on MgO(001), for example [3,17]. The geometry of the growth in the first case makes it very difficult to distinguish the BCC structure from the FCC one (every reflection in the <001> zone of BCC corresponds to an FCC one), but in-plane strain measurements allowed the tetragonality to be inferred.

Studies using LEED (low energy electron diffraction) show the growth of tetragonally distorted BCC Cu(001) on BCC Fe(001)[18]. However, since LEED fails to differentiate between Cu and Fe, low coverage structural analysis is not possible.

A study of sputtered Co/Re multilayers using x-ray diffraction at low and high angles led to an inferred out-of-plane expansion of the Co(002) layer [19]. Once again, not all the information contained in the films is being measured, and the in-plane measurements are used to judge out-of-plane changes. In order to provide information about the vertical spacing during growth, the technique of x-ray photoelectron or Auger forward scattering is starting to be used [20]. It provides information as to whether growth is layer-by-layer: 1ML Fe deposited on Cu(001) agglomerates and intermixes [21].

XAFS, which is element specific and local, has the potential to detect the small changes in local structure in-plane and out-of-plane required to evaluate the effects on magnetic, or other, properties. The general rule is that elements are distinguishable using XAFS when they are separated by four elements in the periodic table (ie. Z can be differentiated from Z+5). However, as will be pointed out in this thesis, there remains ambiguity in the results when Cr and Cu are layered.

Total reflection, or surface, XAFS [22] has been used to determine the crystallographic structure of a variety of MBE grown thin films [23-27]. The parameters obtained from such analysis include the lattice parameter parallel and perpendicular to the surface of the film, the mean-square relative displacement between the atoms, as well as the coordination numbers of each shell of atoms in the sample.

The contents of this thesis are divided into six sections. In the second chapter the theoretical foundation of XAFS are outlined and aspects related to extracting structural information from an XAFS spectra are discussed. The third and fourth chapters contain information pertaining to the preparation of the substrates and samples, as well as the experimental set-up used for total reflection XAFS. The fifth and sixth chapters contain the results of the data analysis for, in Chapter V, the MBE films, and, in Chapter VI, the RF sputtered films. The actual procedure used for curve fitting the data is given in Appendix A, in order to not overburden the main text. Chapter VII gives the conclusions and discussion of the structural analysis of the MBE samples.

CHAPTER II: The XAFS Equation

This chapter covers the theoretical aspects of XAFS which are necessary to explain the experimental spectra. All the techniques used in acquiring structural information from the spectra will be described; the background removal, the Fourier transform technique, and the modelling done in order to curve fit the experimental data.

2.1. Theory of XAFS

An x-ray absorption spectrum can be measured when electrons in occupied levels are excited to unoccupied states due to the absorption of x-ray photons [1]. The dominant absorption mechanism is the photoelectric effect. The states to which the core electrons are promoted on absorption will vary from bound states near the Fermi level to unbound continuum states as the energy of the incident x-rays is increased. At the transition from bound to continuum final states an absorption edge with its large increase in x-ray absorption will be observed in an x-ray absorption spectrum.

The following equation (Eq. 2.1) governs the energy exchanges of electronic transitions:

$$h\nu = E_f - E_i \tag{2.1}$$

where E_i (lm state) is the initial state and E_f ($l'm'$ state) is the final state. In the case of absorption, $h\nu > 0$. The minimum photon

energy, $h\nu_0$, required to eject an electron out of an atomic state into the continuum is called the threshold energy, E_0, and corresponds to the binding energy of the electron. The absorption which will be discussed here is the contribution to the x-ray absorption coefficient, $\mu(E)$, due to deep core level excitations.

The pre-edge, absorption edge and x-ray absorption fine structure (XAFS) regions shown in Fig. 2.1 cover a typical spectrum of energies about the edge. As the energy of the monochromatic x-rays incident upon the sample is increased, the absorption decreases throughout the pre-edge region because the cross section for absorption decreases as E^{-n} (n~3) with increasing energy [1], and, as is depicted by the electronic process shown below, the transition from a core level still is not possible at low energies. In this pre-edge region, the absorption coefficient has as its source other shells of the same atom, or other elements which are also present in the sample. At the edge energy, the binding energy of the electron, a core electron can be ejected and the absorption coefficient increases dramatically. The sudden increase in absorption is called an absorption edge. In a very narrow region about the edge, the absorption coefficient reflects the availability of empty states around the Fermi level. The transition will show some structure which evidences the existence of these unoccupied states.

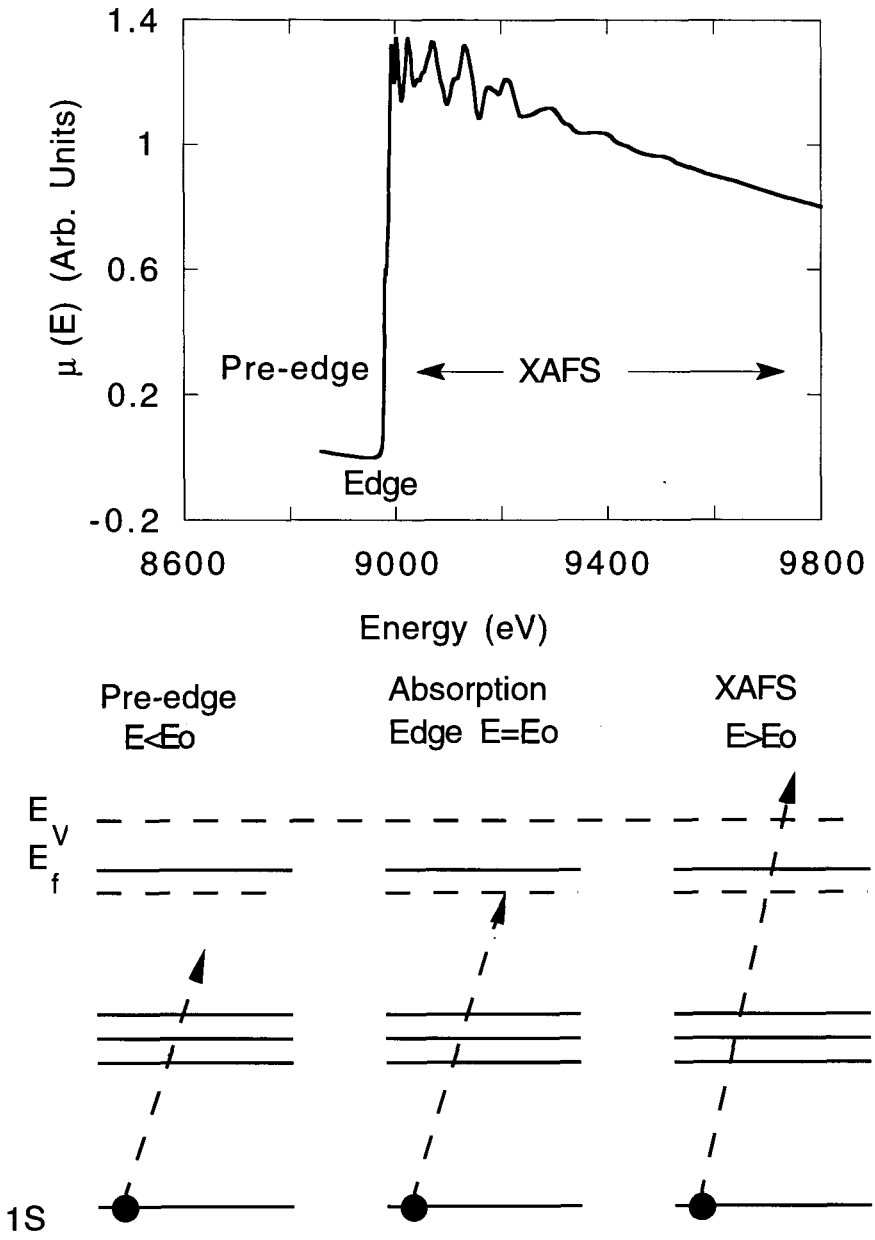

Figure 2.1. Absorption Spectrum showing the pre-edge, absorption edge and XAFS regions of a typical spectrum of bulk Cu for the 1s electron (K edge.) In the electronic processes depicted in the lower part of the figure E_v is the vacuum level, E_f the Fermi level, and the work function of the material is $\phi = E_v - E_f$. The dashed lines below the Fermi level represent localized bound electronic states.

Following this abrupt increase, the absorption will decrease (as the cross section for absorption decreases) until the x-rays' energy reaches that necessary to eject a core electron from another orbital of higher binding energy. In this domain, from a few electron volts (eV) to some hundreds of eV beyond the edge, the coefficient shows modulations which decrease in intensity with increasing energy of the incident photons: this is the region of XAFS. It is from this range of energies that one obtains information concerning the interatomic distances, near neighbour coordination numbers as well as a description of the correlated motion of the atoms of which the material is comprised. In the case of a monatomic sample, such as an isolated atom, the decrease in $\mu(E)$ above the edge is a smooth function showing no modulations ($\mu(E)\alpha E^{-n}$, n~3 [1]). In earlier years, the XAFS was divided into two distinct regions. The XANES, which extends from the edge to ~50eV above the edge, depends strongly on the stereogeometry of the sample whereas the XAFS, which begins ~50eV above the edge, provides radial information.

XAFS spectroscopy refers to the measurement of the x-ray absorption coefficient μ, as a function of photon energy above the threshold of an absorption edge. In the electric dipole approximation, deep core level excitations can be related to the transition rate per unit photon flux, $1/\tau$, by using Fermi's Golden rule [2], in the following manner:

$$\mu(E) \propto \frac{1}{\tau} \propto \sum \left| \langle f | e\vec{\varepsilon} \cdot \vec{r} | i \rangle \right|^2 \delta\left(E_i - E_f + \hbar\omega\right) \rho(E) \qquad (2.2)$$

Here, e is the charge of the electron, E_i and E_f are the energy of the initial and final states respectively, such that $E_f = E_i + \hbar\omega$, $\vec{r}$ is the position vector of the electron, and $\vec{\varepsilon}$ is the polarization unit vector of the electric field. The δ is the Dirac delta which insures the conservation of energy during the absorption process. The absorption edges examined in this thesis are K edges which correspond to a transition from 1s to an empty p state.

The relaxation mechanisms which allow the atom to readjust to the core hole are the following: fluorescence, emission of Auger and secondary electrons, shown in Fig. 2.2.

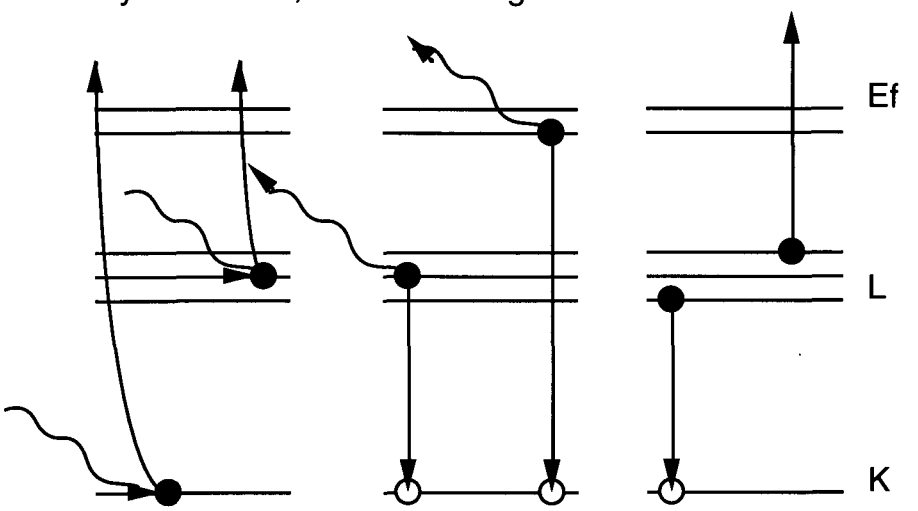

Figure 2.2. Electronic transitions of fluorescence and Auger emission.

The fluorescent yield increases with increasing atomic number reaching the yield of the Auger electrons at about Z=30. We will

measure the radiative fluorescence since it has a relatively high yield for K-shell excitations, and a better signal to background ratio than secondary electron yield for the ultrathin films studied here. The energy of the fluorescent radiation is the difference in energy between the two shells involved in the transition, and is thus characteristic of the absorber.

The modulations in the absorption, or fine structure, are due to the scattering of the outgoing photoelectron by the neighbouring atoms. In the absence of other atoms (isolated atom), the final electron state is an outgoing wave which remains a monotonic function of the photon energy above threshold. In a solid, the interference is as depicted in Fig. 2.3. The outgoing photoelectron of energy E, and deBroglie wavelength λ, will be backscattered from the neighbouring atoms thus producing an incoming wave which can interfere either constructively (the total distance between the atoms, $2R_j$, is a half integral multiple of λ) or destructively ($2R_j$ is an integral multiple of λ) with the outgoing wave resulting in the oscillatory behaviour of the absorption shown in Fig. 2.1.

The type and number of atoms surrounding the absorbing atom will determine the amplitude of this variation, whereas the distance to the neighbouring atoms will affect its frequency, hence the local sensitivity of XAFS.

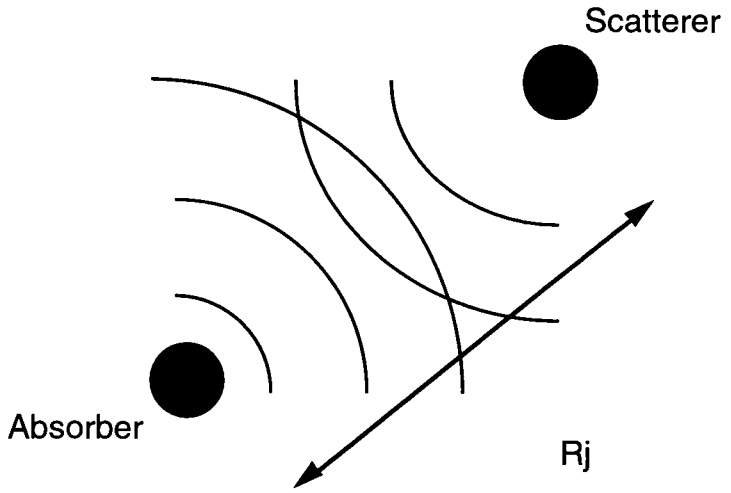

Figure 2.3. Interference between the outgoing and scattered (incoming) photoelectron wave.

The XAFS function, $\chi(E)$, is defined as the oscillatory part of the absorption, $\mu(E)$, normalized to the total absorption, and is given by Eq.2.3.

$$(2.3)\quad \chi(E) = \frac{\mu(E)-\mu_0(E)}{\mu_0(E)}$$

Here, $\mu_0(E)$ is the smoothly varying part of the absorption past the edge (ie the absorption of the isolated atom). The energy of the emitted photoelectron is given by the difference between the energy of the absorbed photon, E, and the binding energy of the core electron, E_0. The photoelectron's energy can thus be related to its wave vector by the expression:

$$(2.4)\quad k = \left[\frac{2m_e}{\hbar^2}(E-E_0)\right]^{1/2} = \left[0.2625(E-E_0)\right]^{1/2}$$

where k is in $Å^{-1}$ and E in eV.

Approximating the spherical waves of Fig. 2.3 by plane waves leads to the simplest approximation for the XAFS interference function $\chi(k)$ given in Eq. 2.5.

(2.5) $$\chi(\pi,k) = A_j(\pi,k)\ \sin(2kR_j + \Phi_{Tj}(\pi,k))$$

$A_j(\pi,k)$ is the amplitude of the photoelectron backscattered from neighbouring atom a distance R_j away from the absorber, and Φ_{Tj} is the sum of the phase shift which occurs as the photoelectron leaves the potential of the absorber and returns, plus the phase shift $\phi_j(k)$ upon backscattering from the neighbour: $\Phi_{Tj}(\pi,k) = 2\delta^c(k) + \phi_j(\pi,k)$. And, giving the terms in Eq. 2.5 explicitly:

(2.6) $$\chi(\pi,k) = \sum_j F_j(\pi,k)\frac{S_0^2}{kR_j^2} N_j e^{\frac{-2R_j}{\lambda}} e^{-2k^2\sigma^2} \sin\left[2kR_j + \phi_{Tj}(\pi,k)\right].$$

The term S_0^2 is a dimensionless variable which describes the reduction of $\chi(k)$ due to multiple excitation effects [3]. As the absorption process occurs, the ionized atom presents a different potential to its surroundings with the removal of the effective shielding provided by the core electron which has been ejected. The increase in the attraction of the nucleus for the passive electrons

causes a relaxation to a lower energy, accounted for by the overlap factor, S_0^2, which takes into account the overlap between the initial and final states of the passive electrons. It varies, in general, from 0.6 to 1.0.

The backscattering amplitude, $F_j(k)$, is the magnitude of the backscattering of a photoelectron by an atom situated a distance R away from the central absorbing atom. It can either be extracted from reference data, or calculated from first principles as will be described in the modelling section of this chapter (Sect. 2.3.3). A damping term, $e^{-2R_j/\lambda}$, is included and accounts for the loss of amplitude (as the photoelectron moves from the absorber to the scatterer and back) due to the limited mean-free path (MFP), λ, of the photoelectron in the solid. The term $e^{-2k^2\sigma^2}$ is the Debye-Waller term, and $\sigma^2=\langle(\vec{r_j}-\vec{R_j})^2\rangle$ is the mean square variation in bond length [15].

The $\chi(\pi,k)$, as described so far, is the first term of a perturbative expansion. Higher terms include scattering paths in which the photoelectron scatters from two (or more) atoms before returning to the absorber. The double scattering terms, are depicted in Fig. 2.4 for a triangular path involving three atoms. The triangular paths are important for quantitative analysis of the first and second nearest neighbours of BCC or BCT metals.

It is possible to include the spherical wave nature of the photoelectron and yet retain the simple plane wave form [4]. The backscattering amplitude and phase shifts must be replaced by R-dependent forms: $A_j(k,R)$, $\Phi_{Tj}(k,R)$.

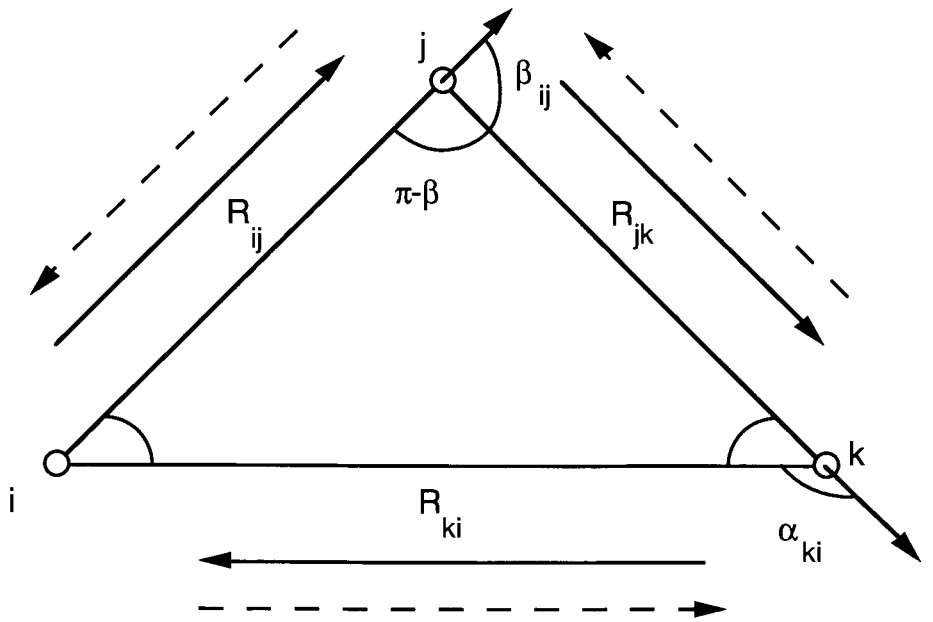

Figure 2.4. Multiple scattering event with path length $2R=R_{ij}+R_{jk}+R_{ki}$. The path "ijki"can be covered in both directions starting from the absorber (placed here at i). In single scattering the photoelectron is backscattered through an angle π returning directly from j to i.

The amplitude term $A_j(\pi,k)$ becomes $A_j(\beta_{ij},kR_{ij},kR_{jk})$ for all scattering angles β_{ij} through R_{ij} to the first scatterer and R_{jk} to the next scatterer (as is shown in Fig. 2.4). The scattering path depicted here involves the wave leaving i to scatter from j towards k, then scattering back to the absorber through the angle α_{ki}. The path may also be covered by moving in the opposite direction. In the same way, $\Phi_{Tj}(\pi,k)$ is adapted to include the influence of the scattering angle β_{ij}. This path technique proves accurate where MS contributions to the $\chi(k)$ are weak. However, only low-order scattering terms can be found without time consuming calculations.

As the distance R from the absorber increases the number of MS required increases: for face-centered-cubic (FCC) Cu and R~12.78Å there are 10^9 independent paths. John Rehr [4] has developed a computationally efficient method of estimating and ranking the contributions of the paths. For example, there are only the 56 paths outlined in Table 2.1 that have an effective amplitude contribution greater than 10%. For the FCC structure a linear triangular path involves scattering within a face. Triangular scattering refers to scattering from a corner of the cube, to the center of one face, then to the center of an adjacent face, and finally back to the absorber. The term focussing refers to scattering events along the face diagonal of the FCC structure, from the corner of the cube through the face-centered atom to the atom on the opposite corner and then back to the absorber (equivalently, along the body diagonal of the BCC structure). A dogleg path consists of scattering from an absorber on the corner of the cube to the face center position and then to another non-diagonal corner of the cube contained within the same face. The path is then reversed to return to the absorber. Quadrilateral paths are four-legged scattering paths.

The expression in Eq. 2.6 can be rewritten for each path as:

$$(2.7)\quad \chi^{\Gamma}(k) = \sum_{\Gamma} F^{\Gamma}(k) S_0^2(k) \frac{e^{\frac{-2R}{\lambda}}}{kR^2} e^{-2\sigma_{\Gamma}^2 k^2} \sin\left[2kR + \phi_T^{\Gamma}(k)\right].$$

Table 2.1. Path analysis for FCC Cu. The 56 important paths are sorted by type, and their relative importance is given, along with their degeneracy. The amplitude difference between calculating 1215 paths (out to R=12.78Å), or the 56 given, is 9.5%.

N	Weight (%), Type
15	46.19, SS (single scattering)
15	24.23, focusing
17	20.67, triangular
2	2.28, linear triangular
4	4.40, other linear
2	1.48, dogleg
1	0.73, quadrilateral
1159	9.5%, all others

Here, the tag Γ refers to each individual path, and signifies that each parameter is path-dependent.Taking into account the polarization of the incoming light involves considering the polarization dependence of the XAFS interference function. From the polarization dependence of Fermi's Golden rule as expressed in Eq. 2.2, the number of atoms at a distance R_j (K shells) can be expressed, for single scattering, as [16]:

$$(2.8)\quad N_j^* = 3\sum_{i=1}^{N_j}\cos^2(\alpha_i)$$

where α_i is the angle between the electric vector $\vec{\varepsilon}$ and the direction vector from the x-ray absorbing atom to the scatterer, and N_j is the total number of atoms in the j^{th} shell. For polycrystalline samples the average over α_i in three dimensions gives N_j. Using the formalism of John Rehr (Eq. 2.7), the effects of polarization can be included in a straightforward manner since his treatment allows for the separation between the matrix element and the MS path-scattering factors [4]. The polarization is expressed in terms of a tensor for general elliptical polarization:

$$\mu(E)=\mu_0(E)\left[1+\sum_{\alpha\beta}(\varepsilon_\alpha)^*\varepsilon_\beta\chi_{\alpha\beta}(E)\right] \tag{2.9}$$

where μ_0 is independent of polarization (the central atom scattering potential is assumed to be spherically symmetric), $\vec{\varepsilon}$ is the x-ray polarization vector, and $\chi_{\alpha\beta}=\Sigma_\Gamma(\chi^\Gamma{}_{\alpha\beta})$ is the XAFS tensor which is obtained from Eq. 2.7.

This curved wave multiple scattering, polarization-dependent approach is used to find the theoretical amplitudes and phases calculated for the least-squares fitting to the experimental results.

2.2 Asymmetric Distribution Functions

The XAFS interference function for a single atomic species is given by [5]:

$$(2.10)\quad \chi(k) = F(k)S_0^2(k)\int P(r)\frac{e^{\frac{-2R}{\lambda}}}{kR^2}\sin\left[2kR+\Phi_T(k)\right]dr$$

where P(r)dr is the probability of finding an atom in the range from r to r+dr, and $\int P(R)dr=N$, the number of atoms in a shell. In all systems with increasing temperature anharmonic contributions to the vibrational displacements of atoms can no longer be neglected and the pair distribution function P(r) becomes asymmetric. P(r) may also be asymmetric due to static disorder. Assuming that the pair potential U(r) is harmonic and P(r) is Gaussian yields incorrect structural parameters: interatomic distances and coordination numbers are too small. For example, at room temperature in strongly covalent systems anharmonicity in the nearest neighbour distances can be neglected, but in systems with weaker bonding, such as Cu, the apparent contraction is ~0.02Å and, as the melting point is approached, coordination numbers can be too small by a factor of two.

Expanding Eq. 2.10 in cumulants (C_n) to fourth order gives [6, 7]:

$$k\chi(k)=A(k)\sin\delta(k)$$

$$(2.11)\quad A(k)=S_0^2F(k)N\frac{e^{\frac{-2R}{\lambda}}}{R^2}e^{-2C_2k^2}e^{(2/3)C_4k^4}$$

$$\delta(k)=2k\left[R-\frac{2C_2}{R}(1+R/\lambda)\right]-\frac{4}{3}C_3k^3+\Phi(k)$$

where C_4 can be neglected at room temperature for the systems in this thesis, and C_3 is given by $C_3 \approx 2\alpha\sigma^2 RT$ [5,17,18], and $C_2=\sigma^2$.
We assume, for the time being, that the MFP is much longer than the R_j (easily fulfilled in a metal, where λ is of the order of 10 times the interatomic distances) and that the variations in the atomic positions, σ_j^2 are small (low disorder, or $\sigma_j^2 < 10^{-2}\text{Å}^2$) as compared to the squares of the atomic distances. In this case Eq. 2.11 simplifies to Eq. 2.12 which is valid for a polycrystalline, one component system measured with unpolarized x-rays and assuming single scattering.

$$(2.12)\quad \chi(k) = \frac{S_0^2}{k} \sum_j F_j(k) \frac{N_j}{R_j^2} e\left(-\frac{2R_j}{\lambda}\right) e^{-2\sigma_j^2 k^2} \times \sin\left(2kR_j + \Phi_{Tj}(k) - \frac{4}{3}C_3 k^3\right)$$

2.3. Data Analysis

Once the absorption spectra data have been collected they can be averaged in order to improve the signal to noise ratio. The following analysis is performed on the averaged data sets. The first step involves removing the background from the spectrum. The normalized raw spectra can then be compared to those of known structures for a quick qualitative appraisal of the sample's unknown

structure. Fourier transforming the raw spectra leads to more knowledge of the sample. Direct inspection of the Fourier transforms (FT) gives us information relating to the radii of the various shells, their amplitudes, and the level of disorder in the system. The only method available for determining all structural parameters with a high order of precision when two shells are present under a single peak is that of curve fitting. This entails the use of the parametrized equation given earlier (Eq. 2.7) and theoretical amplitudes and phases obtained from the program FEFF 6.10 [4].

In the following, the first sub-section describes the background removal program used here. It is followed by a description of the Fourier transform technique, the modelling program FEFF6.10, and the curve fitting program EXAFIT [8].

2.3.1 Background Removal

The XAFS interference function $\chi(k)$ was obtained from the measured fluorescence yield using the background removal program AUTOBK [9]. This algorithm separates the XAFS from the fluorescence according to Eq. 2.3, where $\mu_0(E)$ is the absorption of the isolated atom, which is assumed to be a more smoothly varying function of energy than the XAFS itself. In a first step the pre-edge background is removed by fitting a straight line to the pre-edge region, then the data is placed on a per atom basis by normalizing to the edge jump. This is followed by a post-edge background removal (see Fig. 2.5). In this last step, the absorption of the isolated atom

is approximated by a series of cubic splines. The background is defined as being the part of the measured absorption which does not contain any structural information: the low-R behaviour of the FT (explained in Sect. 2.3.2) is specifically targeted and minimized. The definition of background is used by the program in an iterative approach, as shall be seen soon.

Other schemes use cubic splines (4th order polynomials with knots which have one degree of freedom each) to approximate the background. The value of the spline and its first two derivatives are required to be continuous at the knots, while the third derivative is allowed to be discontinuous. The spline is kept from following the absorption spectra too closely by limiting the number of knots. Descriptions of different background removal schemes can be found in the literature [10,11,19]. They have proven useful in the extended part of the spectrum, but can be unreliable near the absorption edge.

The technique used here was chosen for its reliability at low k, and its ease of use. A good background removal will give a FT which contains almost no low-R components aside from leakage from the first shell. Since the partial pair-correlation function is small below the first-neighbour distance, the XAFS signal must be small at low R. Here, a fourth-order polynomial spline with knots equally spaced in k-space is subtracted from the data, the data is transformed and the low-R portion is examined. The spline is allowed to vary until the low-R region is optimized. In this technique a $\chi(R)$, FT of $\chi(k)$ calculated from a theoretical model, can be used to give an idea of the leakage into the low-R region that is to be expected, or, the program can simply minimize the $\chi(R)$ over a

low-R region specified by the user where the XAFS is expected to be small. The maximum number of knots in the spline [9] is given by Eq. 2.13, where R_{bkg} is the upper limit of the low-R region over which the background is to be minimized, and Δk is the range of available data.

$$N_{knots} \leq \frac{2R_{bkg}\Delta k}{\pi} \tag{2.13}$$

Typically, R_{bkg} will be about half of the distance to the first shell peak. To minimize R components higher than R_{bkg} in the background, the knots are set to be equally spaced in k-space, so that R_{bkg} can be thought of as the Nyquist frequency, above which no signal can be measured.

As an example, AUTOBK was used to subtract the background from the absorption collected by transmission through a Cu foil, shown in Fig. 2.5. In this case, the background was removed by minimizing the low R behaviour with respect to a standard $\chi(k)$ obtained from theory (FEFF6.10) for the first shell of Cu FCC. A 10% Gaussian window (Eq. 2.14.b) was used, and the edge energy allowed to vary. A pre-edge region was specified to be from 150 to 20 eV below the edge.

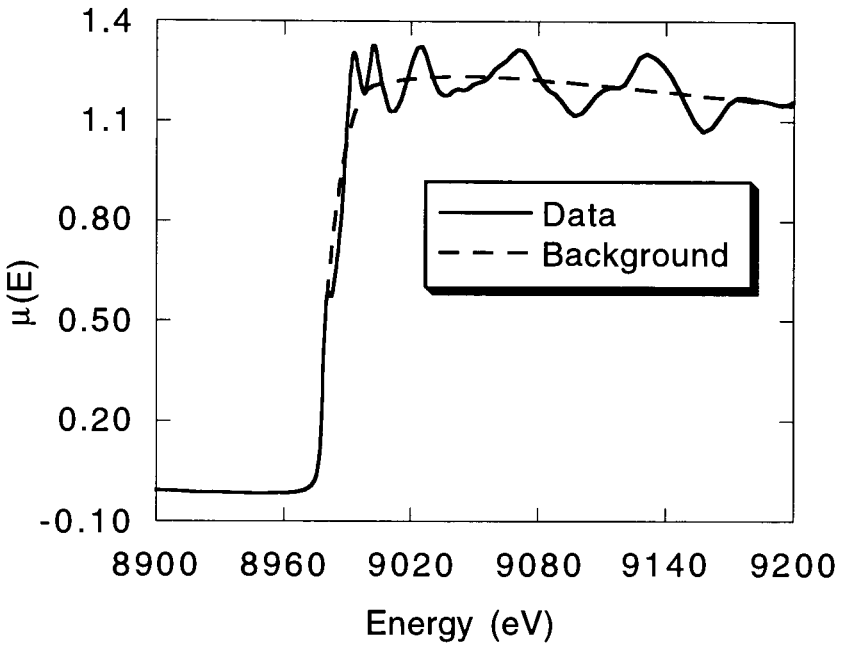

Figure 2.5. Low-energy part of XAFS of Cu FCC at RT. The solid line shows the data, and the dashed line shows the background obtained from AUTOBK.

The resulting $\chi(k)$ is given in Fig. 2.6 where it is compared to that obtained by the standard technique of polynomial background removal above the edge region [12]. Note that the use of AUTOBK results in a background removal to lower k, a region which was generally considered to lack reliability due to large uncertainties in the background function through the edge region. In this fashion it has been possible to access $1 Å^{-1}$ more of usable data, which is particularly useful for systems lacking long range order, or systems presenting a short range of usable data.

A good *a priori* estimate of E_0 is necessary since AUTOBK does not vary the edge energy unless a standard is specified. When a suitable standard was not available the edge energies for the spectra were

first evaluated from the position of the first inflection point of the raw data. This point corresponds to the maximum of the derivative of the data with respect to energy, and is chosen as the E_o for reproducibility. The edge energy input to AUTOBK was then fixed at this value and the program used to remove the background from the averaged data sets.

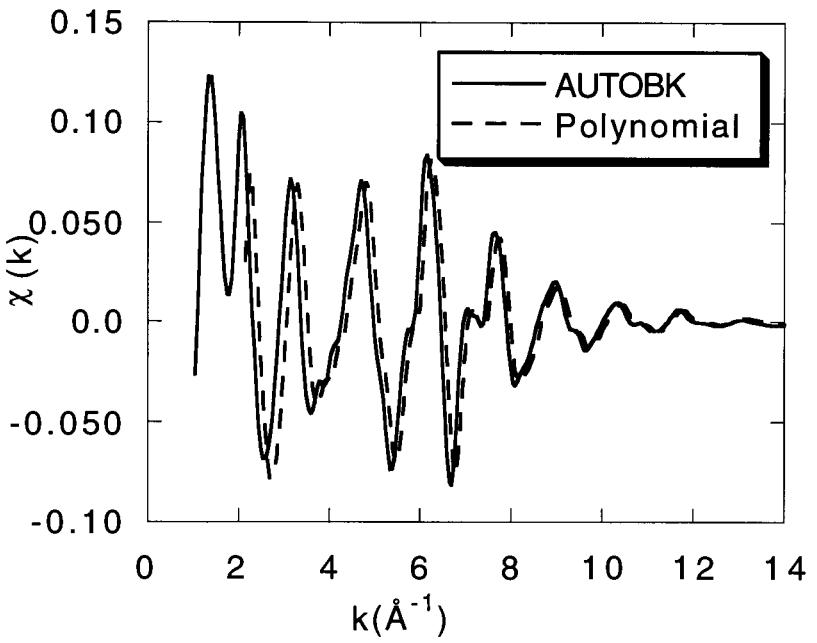

Figure 2.6. XAFS interference function obtained using AUTOBK (solid line), and a polynomial background removal (dashed), for Cu FCC taken in transmission at room temperature. The polynomial spectrum has been shifted by 0.25Å^{-1} in order to aid viewing.

2.3.2 Fourier Transform Technique

The radial distribution function, g(r), describes the R dependence of the number density of the atomic species. It is

obtained from $\chi(k)$ by performing a Fourier transform over an infinite interval of k values. Due to the limited range of data in k space, it is necessary to use a transform window, w(k), in order to minimize transform artefacts. The functional form of the FT is shown in Eq. 2.14.a, where k_{MIN},k_{MAX} represent the limits of the data.

$$(2.14.a)\quad FT = \frac{1}{\sqrt{2\pi}} \int_{k_{MIN}}^{k_{MAX}} w(k)\, k^p\, \chi(k)\, \exp(2ikR_j)\, dk$$

Here w(k) is a window function which is real and even, and p is the power of k by which we wish to multiply the data in order to weight the range we wish to emphasize, and thus take full advantage of the Z dependence of the backscattering amplitude. In order to emphasize light elements a k^1 transform will weight the high amplitude at low k. For heavier elements a k^3 transform will emphasize the higher end of the spectrum.

The window functions used in this thesis are the following:

$$(2.14.b)\quad w_G = \exp\left[\left(\frac{2(k-k_{mid})}{\Delta k}\right)^2 x \ln(0.1)\right]$$

$$w_H = 0.1 + 0.9\cos\left(\frac{2\pi(k-k_{mid})}{\Delta k}\right)$$

where the subscript H refers to the Hanning window (a 10% Hanning), G to the Gaussian (a 10% Gaussian). The interval of data is defined as $\Delta k = k_{MAX} - k_{MIN}$, and k_{mid} is the middle point of the range.

2.3.3 Modelling with FEFF6.10

The structures to be analysed were, to a first approximation, BCC. As a result, the first and second nearest neighbours ($R_1=a\sqrt{3}/2$, $R_2=a$) shells were present under the first peak of the FT. In order to analyse the data and obtain structural parameters it was therefore necessary to do a non-linear least squares fit to the data. The theoretical amplitudes and phases were calculated using the program FEFF6.10 [4]. The reliability of the amplitudes and phases was tested on known structures (FCC Cu, BCC Cr, BCC Fe) taken under conditions identical to those used during the data acquisition of the multilayers studied here. As a result of modelling BCC Cr it was noted that the triangular paths[1] were necessary in order to simulate the data. This was not the case for BCC Fe or metastable BCC Cu, where the triangular multiple scattering paths cancel one another due to a difference in phase. For Fe, the triangular paths are 0.68% of the curved wave amplitude of the single scatterers (first nearest neighbours), and for Cu they represent less than 2%.

---

[1] The triangular multiple scattering paths are, for a BCC or BCT structure, paths leading from the absorber to a body center, then to a corner and back to the absorber, or, from the absorber to a body center, then to another body center one lattice parameter away, and back to the absorber.

2.3.4 Curve Fitting Method

The curve fitting technique used here is a multi-shell non-linear least-squares fitting technique.

The program used is called EXAFIT [8] and it was used to fit polycrystalline materials to the following curved wave expression:

$$\chi(k) = S_0^2 \sum_j \frac{1}{k} A_j(k,R) \frac{N_j}{R_j^2} e\left(-\frac{2R_j}{\lambda}\right) e^{-2\sigma_j^2 k^2 x} \sin\left(2kR_j + \Phi_{Tj}(k,R) - \frac{4}{3} C_{3j} k^2\right) \tag{2.15}$$

where $A_j(k,R)=F_j(k,R)S(k)$.

The sum in Eq. 2.15 is over all the j coordination shells. The backscattering amplitude is $A_j=S(k)F_j(k,R)$, where S(k) is the reduction factor which accounts for the total central atom loss factor ($S(k)=\exp(-Im(2\delta_c))$ where $Im(2\delta_c)$ is the imaginary part of twice the phase shift as the photoelectron leaves the absorber). Both A_j, the phase, Φ_{Tj}, and the MFP, λ, were calculated using FEFF6.10. The value of S_0^2 was set to be equal to the value for the bulk elements. The photoelectron wave vector, k, is shifted where necessary by the fitting parameter ΔE_j to account for the fact that the potential used by FEFF6.10 was not calculated self-consistently. FEFF6.10 imposes a muffin-tin potential and the possible charge

transfer effects are neglected. In this thesis ΔE_j has been assumed to be equal for all shells that have the same scatterers (ie $\Delta E_1=\Delta E_2=\Delta E_3=...$), and where it is linked to the k-scale of the measured XAFS by:

$$(2.16) \qquad k_j=\left[k^2-\frac{\Delta E_j}{\gamma}\right]^{1/2} \qquad \text{where } \gamma\equiv\frac{h^2}{8\pi^2 m_e}=3.809.$$

The effect of the monochromator resolution function can also be included by multiplying Eq. 2.15 by M(k) where

$$(2.17.a) \qquad M(k)=\exp\left(\frac{-(2R_j+s_j)^2\tau^2}{8\gamma^2 k_j^2}\right).$$

In it a Gaussian form was assumed for the spectrometer function [13], where s_j is the mean slope of the total phase of shell j. The width of this Gaussian is τ, and it is related to the FWHM by $\tau=FWHM/2\sqrt{2\ln 2}$. The contribution from the divergence of the x-ray beam is given by $\Delta E/E=\cot\theta\Delta\theta$, where $\Delta\theta=d/L$ with d the width of the slit in front of the monochromator which is located L=20m away from the x-ray source. The FWHM is therefore linked, using Bragg's law, to the width of the spectrometer function by Eq. 2.17.b.

$$(2.17.b) \quad FWHM=\frac{d}{L}(E_0+\gamma k^2)\sqrt{\left(\frac{E_0+\gamma k^2}{E_{MIN}}\right)^2-1}$$

E_{MIN} depends on the diffracting crystals used in the monochromator, and represents the minimum energy at which it can be operated. Here, E_{MIN}=1977eV for the Si(111) monochromator that was used. The γ is given in Eq. 2.16, and E_o is the edge energy of the edge being studied.

The fitting parameters are generally R_j, the radius of the shell with coordination number N_j, and σ_j^2 the mean square relative displacement (the sum of the thermal and static disorder). The term C_{3j} is the asymmetry term due to deviations from a Gaussian distribution function. Its values were approximated using α, the thermal expansion coefficient of the bulk metal at room temperature, R, the radius of the corresponding shell, T, the temperature at which the data were taken (room temperature in all cases): $C_3 \approx 2\alpha\sigma^2 RT$ [5,17,18]. The values of C_{3j} were fixed during the fitting. The correction term $-(2C_2/R)(1+R/\lambda)$ is of the order of 0.009Å for the first shell of Cr, and corresponds to 0.36% of the R value and was not used as fitting parameter but subtracted from the data after the fitting was complete.

The fits were performed in R space over the range of the first peaks of the FT unless otherwise specified. The FT of the data and the model are calculated using the Fast Fourier Transform [14], therefore any transform artefacts will be equally present in both the data and the model.

The program simultaneously fits $Re(FT(k^p\chi(k)))$ to $Re(FT(k^px))$ and $Im(FT(k^p\chi(k)))$ to $Im(FT(k^px))$ where Re and Im denote the real and imaginary parts of the FT, and x=y(k) represents the data. As was mentioned in section 2.3.2, the data can be multiplied by a power of k (p=1, 2, 3) in order to compensate the decrease of the backscattering amplitude with increasing k.

The goodness of fit is determined by the residual sum of squares, χ^2:

$$(2.18) \qquad \chi^2 = \frac{n_{free}}{n_{free}-1}\frac{1}{2M_R} x \sum_{i=1}^{M_R}\left(\left[Re(FT(k^px))-Re(FT(k^p\chi(k)))\right]^2+\left[Im(FT(k^px))-Im(FT(k^p\chi(k)))\right]^2\right).$$

In Eq. 2.18, M_R refers to the number of points available in R-space. n_{free} is the maximum number of parameters that can be varied for a given interval in k-space and R-space. It is given by Eq. 2.19:

$$(2.19) \qquad n_{free} = 1 + \frac{2\Delta k\Delta R}{\pi}\frac{\frac{k_{max}}{\Delta k}}{\left[\frac{k_{max}}{\Delta k}\right]}$$

where $\Delta k \equiv k_{max}-k_{min}$, the limits of the usable range of data in k-space, and ΔR is the interval in R-space used for the fitting. The square brackets in Eq. 2.19 refer to the largest integer not exceeding the term in the brackets.

In the MBE samples the polarization dependence cannot be neglected. They are oriented in a linearly polarized x-ray beam and because of their finite thickness are intrinsically anisotropic. They were fit to Eq. 2.7 where each path was modeled using FEFF6.10. Once the first peak of the FT had been fit, higher order shells were simulated by running FEFF6.10 with the parameters obtained from the polarization-independent fitting of the first peak and taking into consideration the polarization of the incoming x-rays. This proved to be an accurate way of simulating BCT structures which are, by definition, polarization dependent.

2.3.4.1 Curve Fitting Procedure

The procedure followed is outlined in detail in Appendix 1. The following is an abridged version which brings to light the main points. In a first instance, the value of S_0^2 was determined by fitting the data from known structures (bulk elements, taken in transmission) while allowing the product $S_0^2 x N_j$ to vary. The values obtained in this fashion gave the coordination numbers of the bulk elements to within 10%, and values for S_0^2 which were between 0.75 and 0.85, in concordance with the literature [3]. During the fitting of the unknown samples this value was set and fixed at that of the corresponding element. The value of ΔE_0 was also found by fitting known reference structures, and remained fixed at this value during the fitting of the unknown samples.

Once the model was multiplied by S_0^2 and shifted by ΔE_0, the fitting could begin. In order to find minima in parameter space for the remaining variables, a plot of χ^2 was drawn for each parameter while all the others varied. A subset of coincidental minima were found for any highly correlated variables, for example N_j and σ_j^2. The values of the parameters were then moved to the minima, and their range of possible values limited. The program was then used to find the least squares fit of the model to the data. The error bars were found by finding the range of each parameter which doubled the residual sum of squares, while allowing all variables to vary.

CHAPTER III: SAMPLE PREPARATION

This chapter contains information concerning the samples that were grown, both by MBE and by RF (radio frequency) sputtering. A section is dedicated to the preparation of the substrates before growth; single crystal Ag(001) in the case of the epitaxially grown samples, and SiO_2 for the sputtered ones. The lattice mismatches of pseudomorphic epitaxial layers are calculated for each material grown, and a quick overview of their consequences is given, alongside any pertinent information found in the literature concerning the growths. The growth parameters are outlined for each set of samples, and the reflection high energy electron diffraction (RHEED) patterns of the MBE grown films are discussed. This first portion of the chapter contains the particulars of the MBE films, the second those of the RF sputtered films.

3.1. MBE Films

3.1.1. Substrate Orientation (Ag single crystals)

The Ag(001) single crystal substrates were cut from a boule of crystal supplied by the Monocrystals Company, Ohio, USA. They were sliced at a very slow rate (0.5-1.0 mm/hour) from the 19mm diameter boule using a FORM 20 spark cutter, from Charmilles Technologies, Switzerland. Small slits were cut parallel to the plane (001) surfaces, for mounting purposes, about half way through the thickness of the slice (5mm) . Both faces of each slice were

electropolished in order to orient the crystal using the Laue diffraction technique. Once this first orientation determination was complete, one side of each crystal was polished on silicon carbide pads using a polishing jig, in a first attempt at bringing the face to within 0.5 degrees of misorientation (measured with respect to the normal to the sample). This represents a relatively large amount of material since the boule as a whole showed a misorientation of roughly 3 degrees, which was transferred to the original slices. The crystals were then flipped, and the same procedure was repeated on the back sides.

The whole process of electropolishing, orientation and mechanically polishing was then repeated. This second step of polishing, which aimed to bring the sample from 0.5 degrees of misorientation, to less than 0.25 degrees, was accomplished using a slurry of aluminium oxide and purified water on nylon pads [1]. The procedure consisted of a first polish using 9 micron powder for 30 minutes. The whole polishing surface, jig and crystal were then minutely cleaned with alcohol in order to eliminate all 9 micron sized debris. The next step was to polish the crystal in a 5 micron slurry, for 30 minutes, and to repeat the cleaning procedure. The last mechanical polishing was performed with a 1 micron powder, until the surface changed colour, from a dull silver to a shiny gray, indicating a change in surface roughness. The sample was then cleaned again, and electropolished [2] for about 5 minutes in a cyanide free solution, to prepare for Laue orientation. The alignment and polishing procedure were repeated on both surfaces of the

crystal, until the faces were parallel, with a misorientation of not more than 0.25 degrees.

Shortly prior to the growth, the substrates were electropolished one last time to remove any traces of the 1 micron powder, as well as surface damage of submicrometer size caused by mechanical polishing. The crystals were then cleaned with acetone and dried with dry nitrogen, to a clean mirror-like finish, devoid of any traces of electropolish. At this point the substrates were mounted on their molybdenum (Mo) MBE holders using clips inserted into the slits on their sides.

The misorientation ($\Delta\Theta°$) of the sample with respect to the [001] direction is given in Table 3.1. The $\Delta\Theta°$ was determined by Laue diffraction with the sample situated ~20cm from the x-ray source. The terrace sizes on the crystals were calculated from the misorientation and are roughly 400Å (±50Å) to 1000Å (±150Å) long on each substrate, based on a step height corresponding to half the lattice parameter of Ag.

Table 3.1. List of substrates and samples, where the integers refer to monolayers. The samples are detailed in Fig. 3.1.

Substrate	$\Delta\Theta°$ ±0.07°	Samples
X1	0.25	Fe/Cu/1 Cr/Cu/Fe 10 Cr/10 Au
X3	0.10	Fe/Cu/3 Cr/Cu/Fe 4 Cr/10 Au
X4	0.20	Fe/Cu/6 Cr/Cu/Fe 5 Fe/10 Au

3.1.2. UHV Cleaning procedure

In order to prepare the surface for growth, all traces of electropolish solution, indicated by the presence of sulfur, must be eliminated, as well as any adsorbed species, especially oxygen and carbon.

A substrate was mounted and placed in the introductory chamber of the MBE, where an initial outgassing took place. The sample was then positioned under the electron gun beam where its surface was analysed using Auger electron spectroscopy. The Auger spectra of the surface, taken from various regions, were used as an evaluation of the progress during the sputtering and annealing cycles of the substrate. The sputtering removes any adsorbed species (O, C, etc) while the annealing removes any surface damage caused by sputtering, as well as facilitating the segregation of sub-surface contaminants by bringing them to the surface where they will be sputtered away. Thus, the procedure was forcibly cyclic:

1. Argon sputter at room temperature (RT) at a rate of one monolayer per minute (1ML/minute) and an argon pressure of $P=2x10^{-5}$Torr for thirty minutes at 5 positions on the substrate in order to cover the entire surface of 290 mm^2. (Note: each sputtering cycle is done at all five positions on the sample in order to allow the full surface to be covered.)
2. Anneal at 550°C for 2 hours, until the sample has outgassed to a residual pressure of less than $P=1x10^{-9}$Torr.
3. Sputter while annealing at $T_1=550°C$, for 15 minutes.

4. Sputter while annealing at T_2=500°C, for 5 minutes.
5. Sputter while annealing at T_3=450°C, again 5 minutes.
6. Sputter while annealing at T_4=400°C, again 5 minutes.
7. Turn off sputtering and continue to anneal for 10 minutes, at 400°C.
8. Cool the substrate to RT.

When the composition of the top 30Å of the surface, as measured by AES, was exempt of S, O, and C, the substrate was deemed ready for growth, and moved into position for low energy electron diffraction (LEED) images to be observed. A simple qualitative LEED evaluation was done on the substrates, for comparative purposes during growth. The substrates were then transferred into the growth chamber and characterised using the reflection high energy electron diffraction (RHEED) technique. The RHEED patterns of the crystals showed well-defined streaks with a precisely defined specular spot: all surfaces showed a precisely defined (001) structure.

3.1.3. Lattice Matching

The samples grown for XAFS analysis fall into three categories. The first was a series of bilayers grown epitaxially by MBE at room temperature directly on the Ag substrate in order to examine the interface between Cr and Ag, in one case, and Fe and Ag in the other. Two samples of Cr were grown on Ag, one of 4ML, the other of 10ML. In the other case, a single 5ML thickness of Fe was deposited on Ag.

The second series, also grown by MBE, consisted of multilayers of varying compositions. The following schematic, Fig. 3.1, shows a pictogram of all the MBE samples. The third series was comprised of two radio frequency sputtered multilayers of Co and Re which were grown on SiO_2 wafers (see Section 3.2 for details).

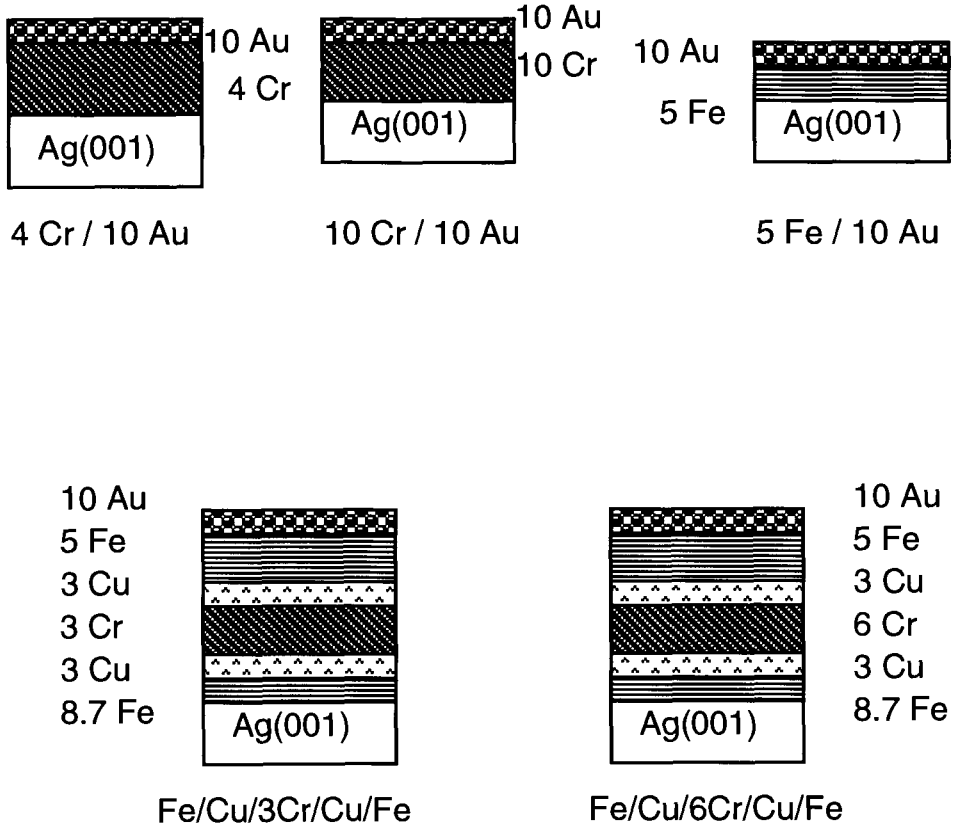

Figure 3.1. Cross sections of MBE samples.

The theoretical lattice matching possibilities are examined in the following section, and a brief overview of similar growths is given.

a. Lattice matching: Fe on Ag.

With a 45 degree rotation, the Fe BCC lattice adjusts to the Ag FCC lattice with a lateral mismatch of less than 1% [3].

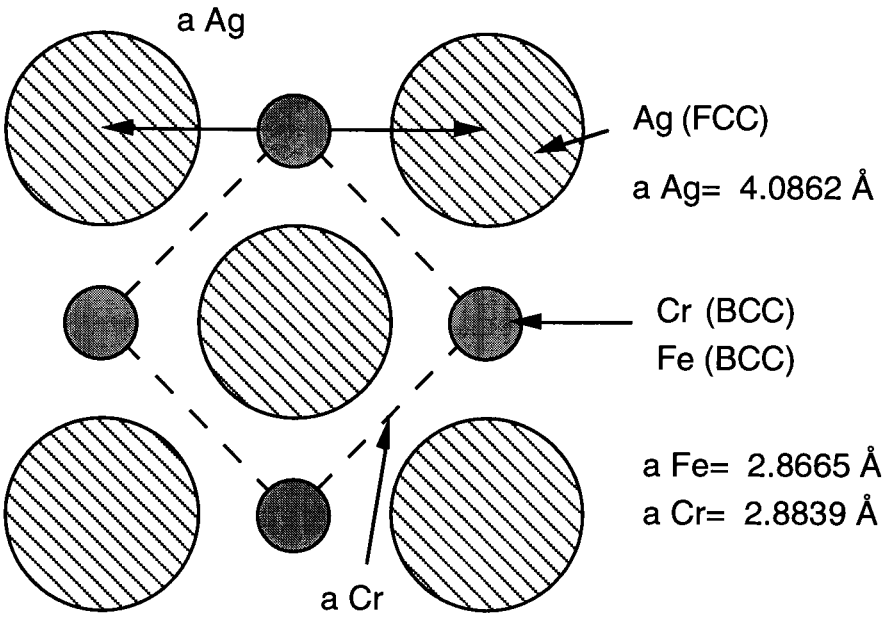

Figure 3.2. Lattice matching of Fe or Cr on Ag(001).

Within a few layers of Fe growth, this mismatch becomes completely negligible for the horizontal direction and the lattice parameter becomes that of bulk Fe [5]. The vertical mismatch of the lattices, which is 17%, is smoothed out within about 5ML of growth of Fe on Ag. This has been verified by the disappearance of what are known as Henzler streaks present in the RHEED pattern of the growth of any mismatched substrate-overlayer system, such as Fe on Ag [5]. Studies of the growth of Fe on Ag(001) have shown that the initial growth is rough. Mossbauer spectroscopy of the first monolayer of Fe^{57} deposited on 3ML of Fe at RT demonstrated that one in five Fe^{57}

atoms was in contact with the Ag(001) substrate [6]. The same technique was used with a base of 4ML of Fe and it was found that the Fe^{57} then occupied sites in the 4th or 5th layer.
Any residual roughness of the Fe growth is counteracted here by a "heat treatment" outlined in section 3.1.4 on MBE sample growth.

b. Lattice matching: Cu on Fe.

Bulk copper normally exhibits the FCC structure. However, with a 45 degree rotation with respect to the Fe BCC lattice there is an 11% mismatch (a_{Fe}=2.8665Å, a_{Cu}=2.55Å) which nonetheless permits epitaxial BCC growth. Because the Cu lattice does not match the Fe one, large strains are expected in a pseudomorphic layer. Pseudomorphy refers to a situation where the overlayer material adopts a crystal structure and lattice constant which differ from their normal bulk values but with the in-plane lattice constants matching those of the underlying substrate. However, RHEED oscillations are generally observed during the initial stages of growth of Cu on Fe. The amplitude of the oscillations decreases until 12 layers have been deposited, at which point superlattice streaks [7] become apparent on the RHEED pattern. This is evidence of a transformation from BCC stacking, to a more FCC like structure [8]. It was concluded [8] that fewer than 12 ML of Cu deposited on Fe gives a structure which is BCC, but is expanded by 1% in-plane relative to Fe BCC, according to calculations on RHEED patterns [4].

c. Lattice matching: Cr on Cu.

Bulk Cr has the BCC structure with a_{Cr}=2.8839 Å: it should therefore grow epitaxially on the BCC Cu (a=2.87Å) surface described above without any important lattice mismatch [3]. For thick films, the growth of Cr on Cu(001) (FCC) at RT has been seen to exhibit ordered BCC domains about 10 lattice parameters in size [9]. Below 3ML the structure was found to be quite deviated from a BCC structure with an in-plane distortion and expansion, and an interlayer contraction along Cr(110). The initial growth mode was deemed to be by islands. It took 4ML to achieve 90% coverage.

d. Lattice matching: Cr on Ag.

As was the case in the growth of BCC Fe on FCC Ag, BCC Cr grows on the FCC Ag lattice rotated in plane by 45 degrees, giving a mismatch of less than 1% [3]. As seen in Fig. 2, Ag(001) should be a good template for the epitaxial growth of Cr in its BCC lattice; the in plane-lattice parameter is essentially the same as that of bulk Cr.

However, from a thermodynamical point of view, the surface energy criterion for wetting, $\gamma_s - \gamma_c - \gamma_I > 0$, where γ_s and γ_c are the surface free energies of the substrate and condensate respectively, is not met [9]. For Ag [10], γ_s=1250 mJ/m^2, γ_c=2400 mJ/m^2, and γ_I~450 mJ/m^2, where γ_I is the interface free energy. This wetting criterion assumes thermodynamic equilibrium as well as the immiscibility of the elements.

Since the Cr-Cr interaction is much stronger than the Cr-Ag one, 1ML deposited at RT results in an inhomogeneous layer which consists of incomplete monolayer and bilayer platelets: the growth is not layer-by-layer at RT. A single layer has proven to be metastable [9]. The bonds to the surface are much weaker than those between Cr atoms chemisorbed to the Cr monolayer.

The second and third levels begin to grow before the first monolayer is complete. Islands of Cr are thus formed on the Ag substrate, and further growth shows a strong tendency toward 3D islands [9,11]. Elsewhere [11], it was found that the strong in-plane antiferromagnetism stabilized the first layer into a monolayer, however, this stability is reduced by the growth of more Cr since it is energetically more favorable for the additional Cr to agglomerate into 3D clusters. In general, the growth mode of Cr on Cr [11] is attributed to the magnetic properties of the monolayer, which are heavily dependent upon its growth history (temperature, rate, etc.)

The literature contains diffraction results which have shown that for Cr coverages higher than 7ML the structure is BCC [11]. Low coverages (1-3ML) have been associated with a distorted BCC structure [9]. Both results were of a qualitative nature. In order to assist in the study of the magnetic properties of multilayers of Cr, the structural parameters of 4ML of Cr on Ag, as well as those of 10ML of Cr on Ag, will be measured using XAFS.

3.1.4. Sample Growth

As was mentioned earlier, five samples were grown by MBE, in a Physical Electronics Molecular Beam Epitaxy System. They were all grown under the same conditions, as described in the following paragraphs.

The residual pressure of the growth chamber was in the low 10^{-10} Torr range for all the MBE growths. The thickness of the deposited films was monitored by an in-situ RHEED calibration system, which gives some structural information, as well as by a crystal thickness monitor (Mathis model TM-100, allowing for an accuracy of ±0.5ML), placed above the substrate. A qualitative analysis of the LEED patterns of the samples was undertaken after the growth of each different element.

The substrate temperature during cleaning and growth was monitored using a standard chromel-alumel thermocouple. The thermocouple is mounted on a Cu block to which the Mo sample holder is attached. It provides a reference point for subsequent growths and was not intended to give the exact temperature of the substrate. Unless otherwise noted, samples were grown at room temperature.

3.1.4.1. Analysis of the RHEED oscillations for the MBE films.

The existence of three growth modes is generally recognized in crystal growth [12]: Frank-Van der Merwe (FV), Stranski-Krastanov (SK), and Volmer-Weber (VW) growths. FV growth is a layer-by-layer growth, whereas VW shows the nucleation of three-

dimensional crystallites as soon as growth is initiated. SK is a combination of the other two: a few monolayers adsorb layer-by-layer, then three-dimensional clumps appear. No persistent RHEED oscillations occur for SK or VW growth [12].

The intensity of the specular spot from a RHEED gun, in Anti-Bragg conditions, will oscillate as the degree of coverage of the substrate changes. The maxima of the parabolically shaped oscillations correspond to a complete layer, whereas the minima correspond to a half-filled layer. The oscillations are observed because a half filled layer scatters more high energy electrons than does a complete layer. In perfect layer-by-layer growth, the oscillations will provoke perfect cusps between each parabola. A substrate with large terraces, such as an Fe whisker, shows near perfect oscillations during homoepitaxy (Fe on Fe) [13].

Imperfect growths, those which occur when the topmost layer is only partially covered before the next begins to grow, will generate RHEED patterns with damped oscillations and cusps which are much less pronounced. The continued presence of oscillations indicates a semi layer-by-layer growth mode in which the simultaneous growth of two layers occurs.

In the cases studied here there was evidence at the onset of growth that the second layer started to build before the first was complete. However, the subsequent layers exhibited a measurable and steady period of oscillations.

In order to minimize the number of figures showing RHEED oscillations not all growths will be outlined. The oscillations for

certain representative layers will be given in detail. Where it is deemed useful some of the more important graphs will be overlaid.

a. RHEED from 8.7 Fe/3 Cu/1 Cr/3 Cu/5 Fe sample

The insert of Fig. 3.3 shows the growth of 1ML of Fe deposited at the rate of 1ML/minute, on Ag(001). This growth was deemed to be too fast, so the furnace was closed. The following 4.7ML of Fe at RT were grown at the slower rate of 1ML/ 3 minutes. A film terminated in this manner is supposed to provide the best surface for further growth of Fe [4,6]. As was noted earlier, the first oscillations are irregular, both in intensity and period. This corresponds to the initial non layer-by-layer growth mode which occurs due to the vertical mismatch between the lattices. In order to ensure a fully complete top layer of Fe, 3ML are grown at 150°C, over the 5.7ML grown at RT which act as a diffusion barrier (to the Ag) at this higher temperature. Strong oscillations during the growth of the 3ML at 150°C can be observed in Fig. 3.4, and indicate a smooth substrate for the subsequent deposition of Cu.

At the end of the first room temperature growth of Fe, the Henzler streaks were no longer in evidence, indicating that all strain due to the vertical mismatch between the Ag lattice and the Fe had been relaxed. The RHEED intensity increased upon deposition of Fe at 150°C as the growth became more layer-by-layer like, and the surface was considered to be smooth [4,6].

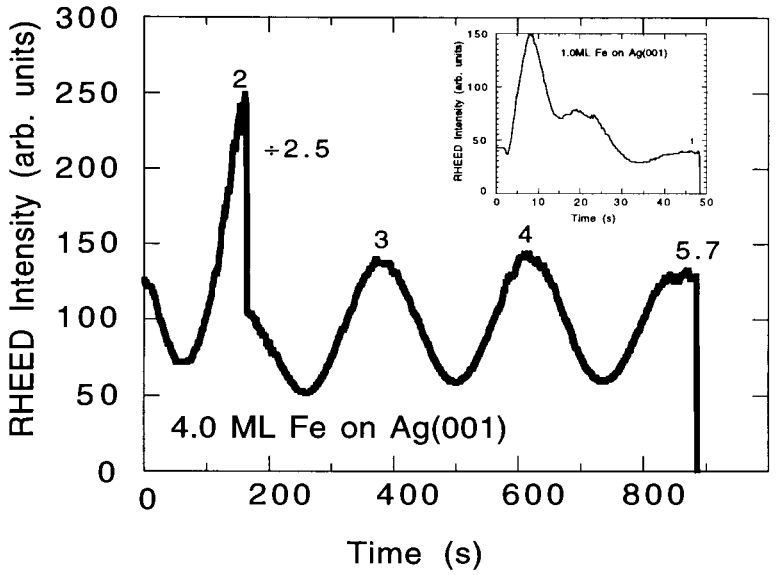

Figure 3.3. Growth of 5.7 ML of Fe at RT on Ag(001). At the end of the second layer of Fe growth the scale was decreased by 2.5. The inset shows the RHEED oscillations of the first layer of Fe grown (at RT) on the Ag(001) substrate.

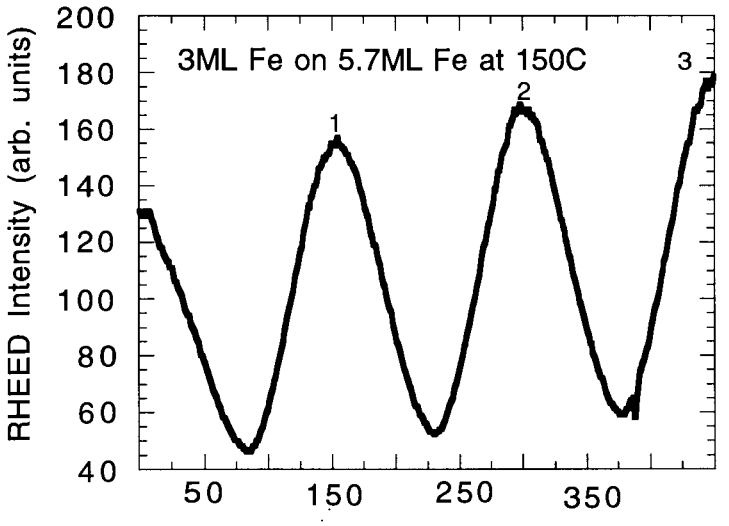

Figure 3.4. Growth of 3ML of Fe at 150C on 5.7ML of Fe.

The resulting surface has been studied elsewhere [4] and is believed to be flat within ± 1ML. The growth of Cu on this flat Fe surface showed large RHEED intensity oscillations from the start, indicating a layer-by-layer mode of growth, as shown in Fig. 3.5. The period of the oscillations was relatively constant at 10 seconds throughout the whole growth. The Cu retains the in plane symmetry of the Fe(001), which indicates a BCC structure. After the growth of the first three layers the amplitude of the oscillations is seen to decrease. The structure is relaxing towards the bulk structure which it will assume after the critical thickness of 12 ML is reached [14]. The size of the clusters in each layer decreases as the film thickens.

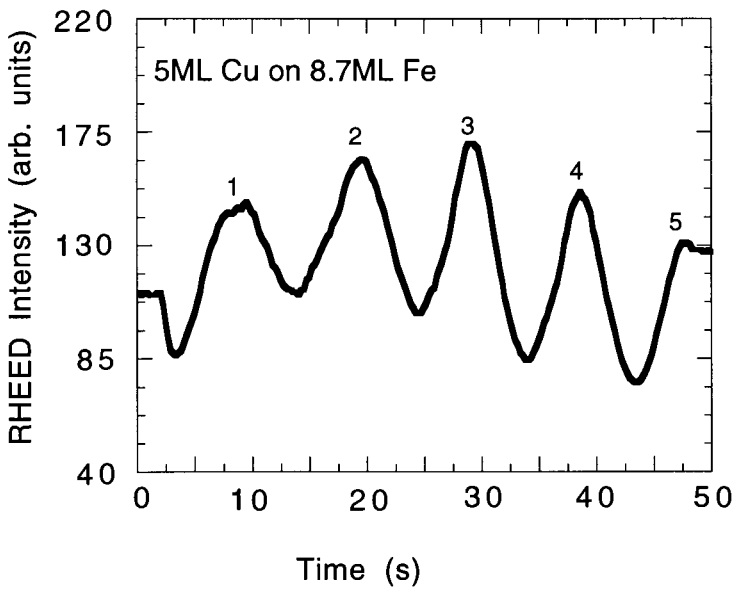

Figure 3.5. Growth of 5ML Cu on 8.7ML Fe at RT.

b. RHEED from the 8.7 Fe/3 Cu/3 Cr/3 Cu/5 Fe sample

The growth of 3ML of Cr on 3ML of Cu is observed in figure 3.6. The Cr grew at a rate of one layer every 50 seconds. Though the oscillations lose amplitude, they remain clear and distinct, as was the case for both the 1ML and 6ML Cr sample growths. The shape and decay of the oscillations is indicative of a growth mode where the second layer begins to grow before the first is terminated.

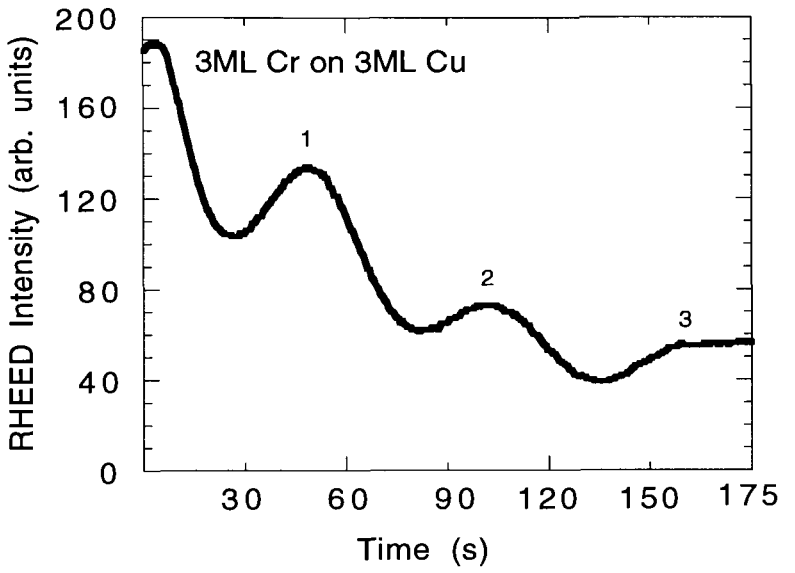

Figure 3.6. Growth of 3ML Cr on 3ML Cu at RT.

After the deposition of Cr, during which the RHEED intensity decreased, though the oscillations are marked, the RHEED pattern sharpened upon the growth of the first layer of Cu.

c. RHEED from the 8.7 Fe/3 Cu/6 Cr/3 Cu/5 Fe sample

Figures 3.7 and 3.8 show examples of the subsequent layers of the structures. In Fig. 3.7, 3ML of Cu are deposited on 6ML of Cr. The figure shows distinct oscillations, indicating that the underlying structure of 6ML Cr was terminated by a smooth layer of Cr, further guaranteeing the "quality" of the growth of Cr. The oscillations are, however, irregular due to an uneven growth rate caused by the furnace. In Fig. 3.8, the deposition of 5ML of Fe (on 3ML of Cu) is shown to be regular (steady rate, and smooth growth).

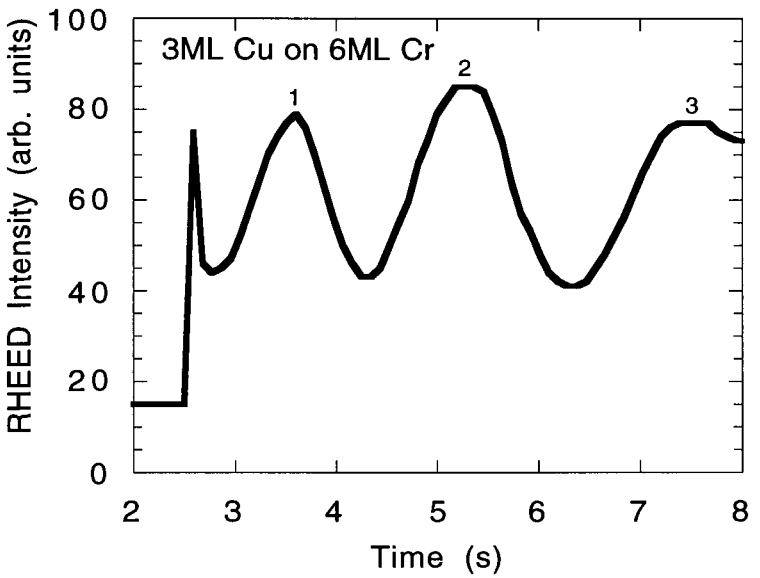

Figure 3.7. Growth of 3ML Cu on 6ML Cr.

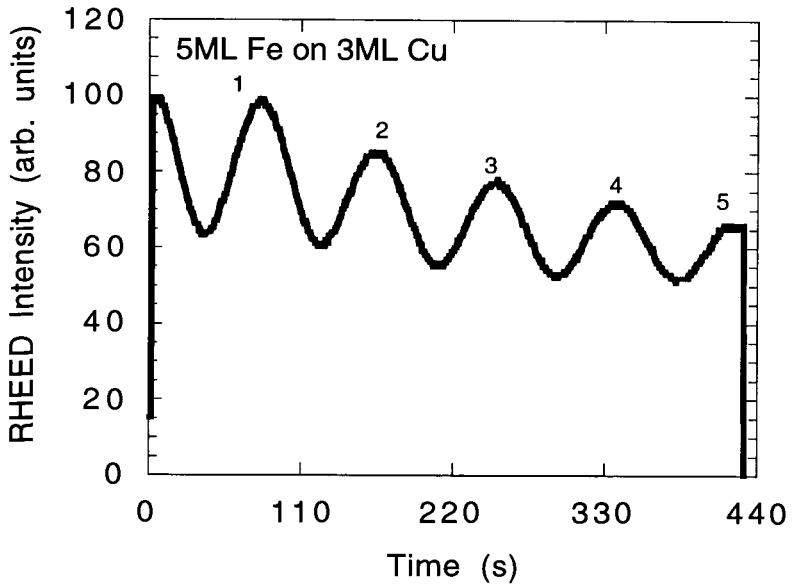

Figure 3.8. Growth of 5ML Fe on 3ML Cu.

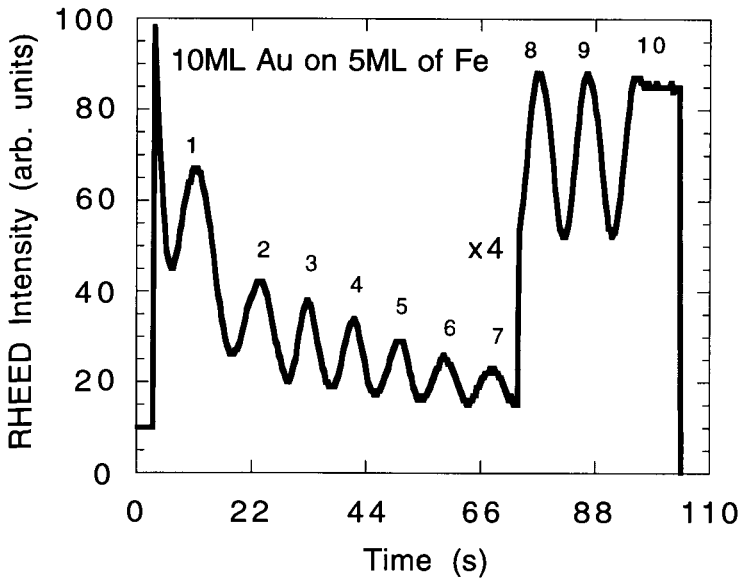

Figure 3.9. Growth of 10ML Au on 5ML Fe at RT. After 7ML of growth the scale was increased by a factor of 4 in order to follow the growth of the following layers of Au.

All the MBE structures were passivated by a deposition of 10 layers of Au. Fig. 3.9 shows the RHEED oscillations of one such growth. This cap of Au prevents the oxidation and other contamination of the structure below, safeguarding the sample for ex-situ XAFS analysis.

d. 5ML Fe/ 10 Au

A previous analysis of the growth of Fe(001) at RT on Ag(001) film templates (as opposed to single crystal substrates) showed that 4ML of Fe are needed to palliate the vertical mismatch between the Fe and Ag lattices [4]. It is known that the oscillations become regular within a few layers, as was the case in this growth. Thus, 5ML of Fe were grown on a silver substrate at RT, and capped with 10ML of Au in order to determine the degree, if any, of alloying between the Fe and Ag.

e. 4ML Cr/10 Au and 10ML Cr/10 Au

As was mentioned earlier, two samples of Cr grown directly on Ag(001) were prepared in order to examine the interfacial intermixing which occurs for RT growths. In both cases RHEED oscillations were observed, though they decayed rapidly after 4ML of deposition.

3.2. Radio frequency sputtered films

Two bilayer samples of Co and Re were deposited on SiO_2 wafers, using a RF triode sputtering source [15].

3.2.1. Substrate preparation

The oxidized Si(100) wafers were degreased [15] using the cleaning cycle described below:

1. Cleaned with purified water and soap (for degreasing Si).
2. Soaked in purified water for 5 minutes.
3. Soaked in tricholoroethylene for 15 minutes, at 40C.
4. Rinsed with acetone.
5. Rinsed with propanol.
6. Dried using argon.

This ex-situ pre-growth cleaning leaves a surface which is 99.9% SiO_2 [16].

3.2.2. Lattice matching

Co and Re crystallize in an HCP structure (Mg type) with lattice parameters a=2.507Å and c=4.069Å, for the α-Co , and a=2.76Å, c=4.458Å, for Re. As a result, for multilayers oriented in the [002] direction (ie. along the c-axis), there is a lattice mismatch of 9.2% between the two lattices. On the other hand, the Co/Re system has a small positive heat of mixing [17] and the alloy phase diagram shows

a continuous solid solubility of the two elements [18]. Crystalline interfaces are thus expected in the bilayer systems studied here.

Nature provides us with two structures of Co, the HCP and the FCC lattices. The BCC structure does not appear on the phase diagram of Co, but exists as a metastable phase. Epitaxial growth of single crystal films, deposited in thin layers, can produce the BCC structure. It is a simple question of energetics: the interfacial energy generated by forcing the Co on to the underlying substrate gives the possibility of creating this metastable phase. Energy calculations show the BCC phase to be metastable, with 0.6 eV/atom more energy than the minimum calculated for the FCC phase, which is 0.3 eV/atom higher than the lowest possible energy phase, HCP.
Studies done using low-angle x-ray diffraction show 2 to 3ML of interfacial mixing when Re is deposited on Co, and a very sharp interface for Co deposited on Re. An out of plane expansion (*c* axis) of the Co layers was observed [19]. The XAFS studies were motivated by these diffraction results.

3.2.3. Sample deposition

The Co/Re bilayers shown below (in Fig. 3.10) were prepared using a modified single source RF triode sputtering system [15]. Two separated targets of 20mm diameter (99.999% Co and Re) were clamped to a water-cooled target support (the cathode) powered by a single RF power supply. Beam confinement and isolation shields were fixed over the targets to prevent intermixing of the fluxes of sputtered atoms. Tests done elsewhere, using x-ray photoelectron

spectroscopy, show that the plasmas remain well separated [16]. Adherence tests done over a period of many years give the ranges of Ar sputtering gas pressure, RF frequency and power necessary to grow good quality films. Deposition rates of each element were measured individually with a quartz-crystal monitor (OMNI III from SLOAN) prior to the growths, at the eventual position of the substrate, and were precisely calibrated using x-ray reflectivity measurements [16]. The thickness of the layers can then easily be determined from the exposure time, using a computer controlled shutter.

The base pressure, prior to sputtering, was always less than $1x10^{-7}$ Torr. The targets were sputtered clean for 20 minutes in order to clear their surfaces of any impurities. During deposition, the pressure of the Ar gas was maintained at 4.0 mTorr, and the substrate temperature rose to 40°C. The deposition rates were 0.7Å/s for Re, and 0.4Å/s for Co at a RF power of 87.5W and a substrate-target distance of 9.2cm.

For sample 1, 69.2Å of Co were sputtered on the SiO_2 over which 40.2Å of Re were deposited, while for sample 2, 75.8Å Re were deposited on the substrate, followed by 24.4Å of Co capped by a layer of 44.6Å of Re, as is shown in Fig. 3.10.

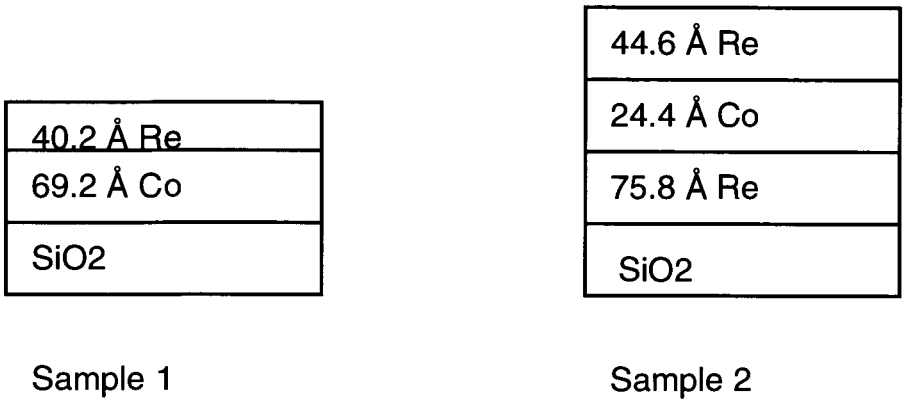

Figure 3.10. Cross Sections of the RF films.

CHAPTER IV: Experimental set-up for total reflection XAFS

This chapter contains an overview of the experimental aspects pertaining to doing total reflection XAFS on ultrathin magnetic multilayers. The total reflection geometry is used in order to confine the electric field of the x-ray beam to the penetration depth of the evanescent wave (~30Å). As the glancing angle of incidence exceeds the critical angle φ_c (of the order of 6 mrad for an air-metal interface) the penetration depth rapidly increases, becoming a few microns at $3\varphi_c$. That is, the x-rays probe the bulk rather than the surface region. The ultrathin films in this thesis are buried beneath absorbing overlayers, and to obtain spectra with a good signal-to-noise ratio the total reflection mode must be used. The important parameters of the set-up will be discussed, as well as the signal detection and acquisition.

The samples we wish to analyze are composed of elements with K edges varying from 5900 eV to 9000 eV, and L edges up to 12000 eV. Synchrotron radiation coming from a wiggler and passing through a Si(111) double-crystal monochromator will accommodate this range of energies. The experiments were carried out at the Stanford Synchrotron Radiation Laboratory (SSRL) on the wiggler side station beamline IV-I.

4.1. Experimental Set-Up

The arrangement of the experiment is shown in Fig. 4.1.

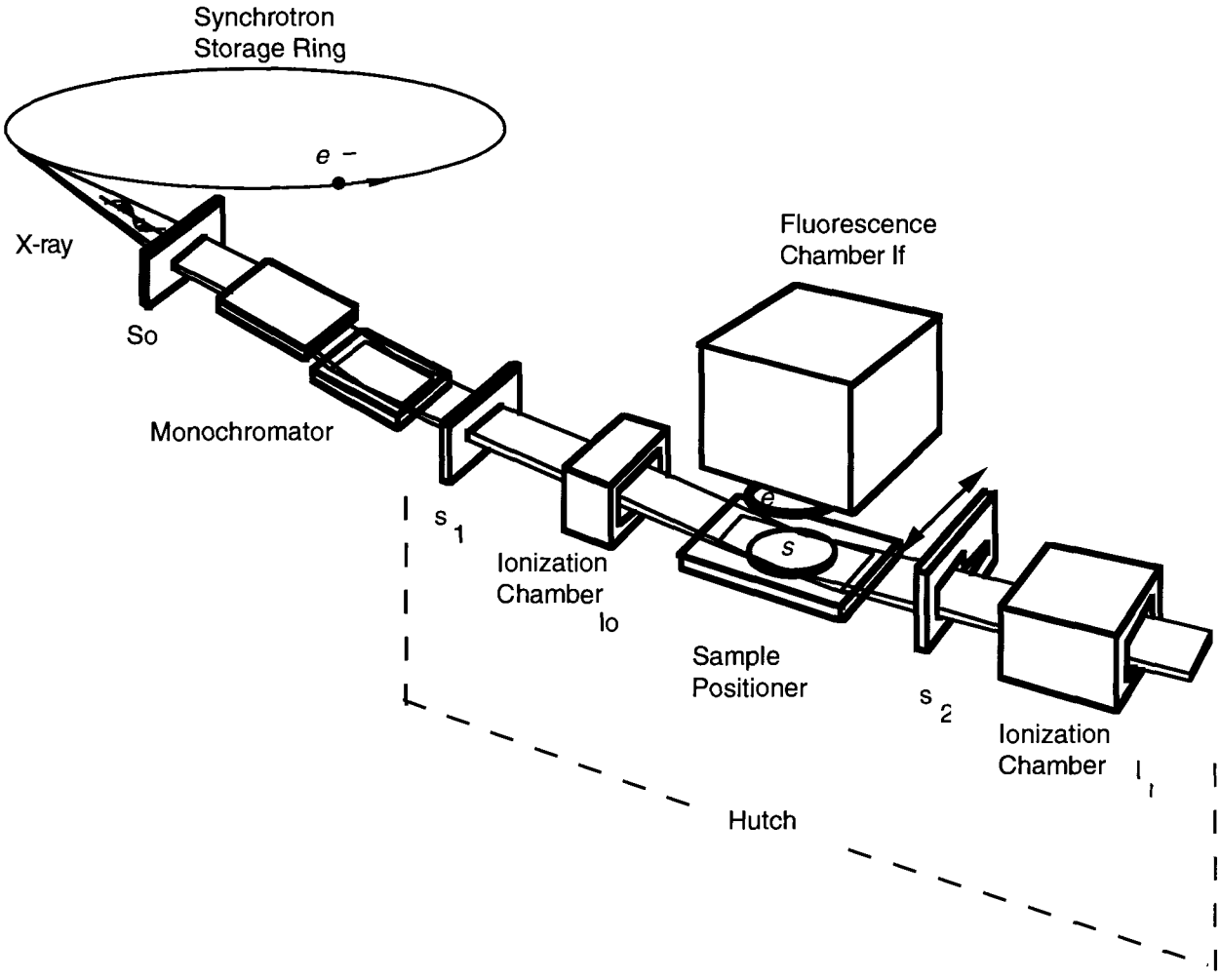

Figure 4.1. Experimental set-up for a total reflection XAFS experiment [2], not to scale.

Following the path of the beam from when it leaves the SPEAR (synchrotron storage) ring, it is first collimated by an entrance slit, S_o, with a vertical aperture of 1mm. The beam passes through the Si(111) double-crystal monochromator, then is once more

collimated, this time by a Huber slit, S_1, with its opening set to 6mm horizontally and 50μm vertically for the total reflection geometry of the experiment. The beam has its electric vector parallel to the sample (as shown in Fig. 4.1).

The Huber slit is mounted on a motor driven rotary stage furnished with an Oriel Encoder MIKETM Actuator (Model 18212) micrometer with digital readout to 0.05μm which allows it to be set parallel to the sample's surface. The intensity of the collimated beam is then detected by an ionization chamber (standard SSRL 6" chamber with N_2) in order to give us I_o. The beam hits the sample at an angle of a few milliradians, measured with respect to its surface. After passing through another Huber slit, S_2, the reflected beam from the sample enters the reflectivity ionization chamber, I_R, placed in the beam's path.

Figure 4.2 shows the sample holder which can be inserted into the positioner which is detailed in Fig. 4.3. The sample was mounted on a heavy brass disk which was fixed to another disk by the means of three screws and ballbearings, as shown in Fig. 4.2. Once the sample had been mounted on the upper disk, a He-Ne laser was used to verify that the surface of the sample proved to be parallel to the top of the positioner, and thus parallel to the beam. The laser was used to check the reflection from the surface of the sample ($\theta_i \sim 20^\circ$) at a distance of 6m. The sample was rotated about its axis and the position of the reflections of each position (1,2,3) were noted. By adjusting the screws it was possible to align the reflected spots from each orientation until they coincided. The normal to the sample

and the axis of the rotation stage are then collinear to within 0.5μrad.

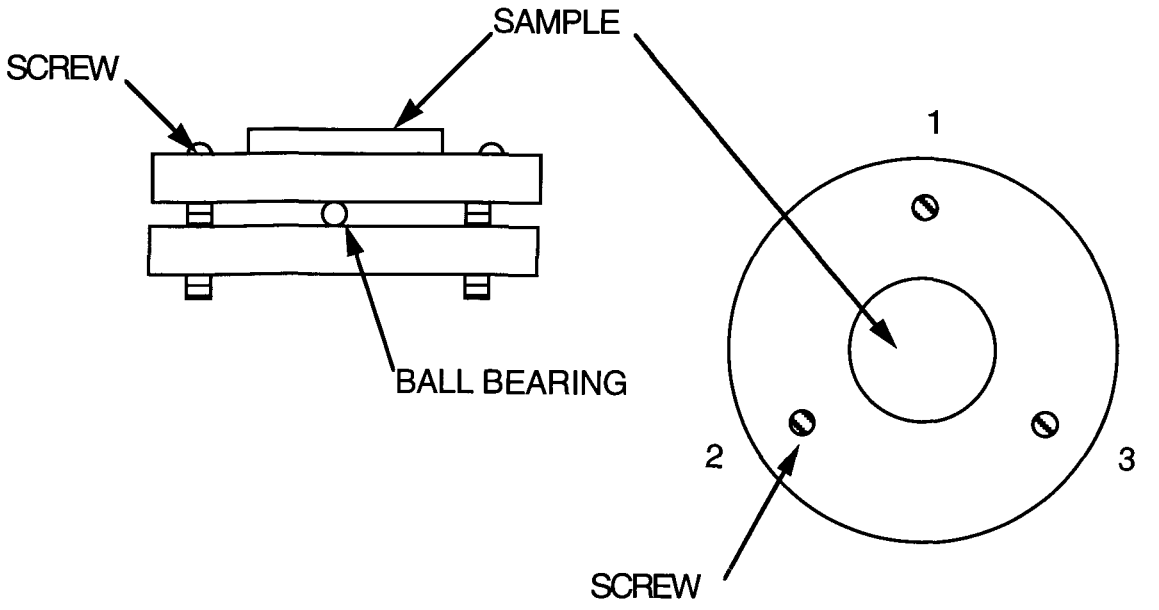

Figure 4.2. Sample holder.

4.2. Sample Positioner

The sample positioner, shown in Fig. 4.3, was designed for glancing incidence XAFS in the hard x-ray region [1]. With this in mind, it was made of a plate of aluminium (a) sitting on two micrometers (b) each placed an equal distance from its center where the sample mount is located (e). The micrometers (40 turns/in, either up or down) are both attached to an aluminium disk (c) which is joined to another by three posts. The lower disk is attached to a stepping motor (d) which provides 200 steps/turn and a holding

torque. In this manner the driving force is transmitted to the micrometer, avoiding any backlash. The platform can thus be tilted (by moving one end up, the other down) at a glancing angle φ, relative to the incident beam, through steps of 13.5μrad. The stepping motors are driven by electronics controlled by a computer which is located outside the hutch.

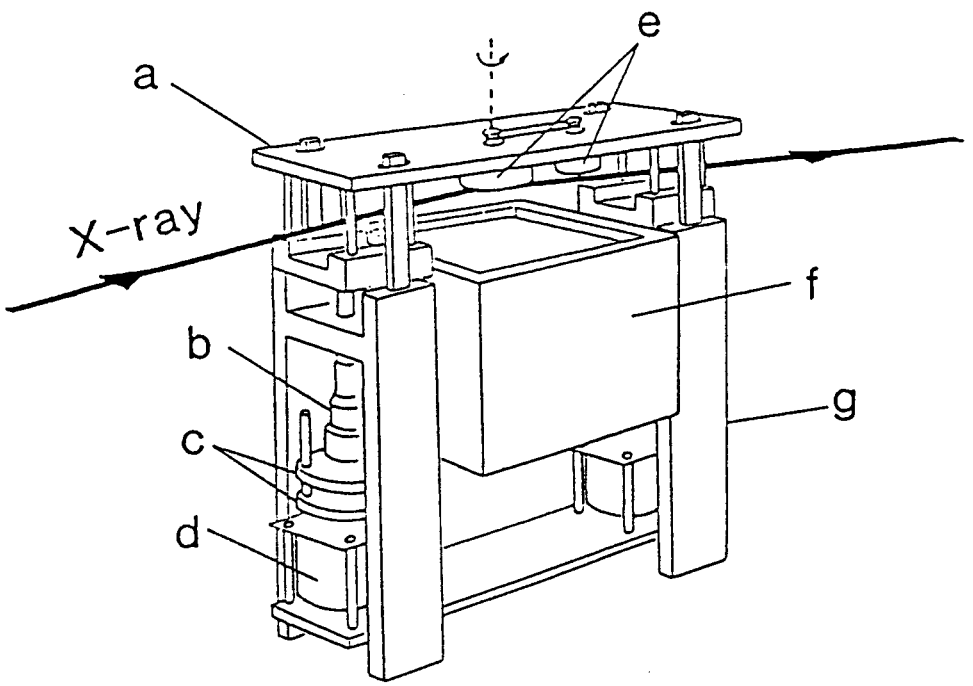

Figure 4.3. Sample positioner used for total reflection XAFS (description given in text) [2].

The positioner is mounted on an aluminium frame (g) which allows it to be laid on its side by 90° (from the upright position shown in Fig. 4.2) in order to perform XAFS with the electric vector of the incident beam perpendicular to the surface of the sample. The

positioner was designed so that the sample could be placed (even in the perpendicular configuration) in the center of the beam path which passes a few centimeters from the hutch wall on this side station.

The fluorescence chamber (f) is an ion chamber which is described in section 4.4.1.

4.3. Alignment Procedure

4.3.1 Defining the beam path

The sample is considered aligned when the slits S_1 and S_2 define a beam path such that the effect of the wedge angle of the substrate has been reduced until it is considered negligible (as will be described in this section), and the Bragg peaks in the fluorescence signal have been minimized.

We define a beam path by setting S_1 (see Fig. 4.1) to 100μm vertically and 6mm horizontally, with the sample surface parallel to the electric field vector of the beam. In order to reduce the wedge angle between the sample and S_1, the sample was tilted by an angle φ such that both the straight through beam and the reflected beam were visible on a ZnS fluorescent screen located in front of S_2. S_1 was then rotated (by tilting the platform) until the wedge angle was minimized (S_1 is made parallel to the sample's surface). Keeping φ constant, the sample was then raised out of the beam. S_2 was rotated (about its axis parallel to the beam) until it was parallel to

S_1 at which point the reflectivity signal reaches its maximum. S_2 is then lowered (the beam stop side first) into the beam in order to cut the reflectivity signal to only 1% of the direct beam, and further insure that only the reflected signal is being measured.

Once the beam path was optimized in this manner, the sample was lowered back into the beam. By iteratively stepping the motors and tilting the sample positioner's platform, the surface of the sample is brought parallel to the beam. This is achieved by determining the tilt angle at which the reflected beam just vanishes. This position was defined to be the $\varphi=0$ position. For $\varphi>0$ the intensity of the reflected beam increases, for $\varphi<0$ the reflected beam is blocked by the sample.

4.3.2. Finding the critical angle

In order to determine the critical angle, φ_c, for any given absorption edge, the sample was tilted through a series of angles (from 0 to ~14 mrad) while the fluorescent and reflectivity signals were recorded at each glancing incidence angle, as is shown in Fig. 4.4. The data were taken at a fixed value of x-ray energy, E_0+200 eV, to reduce the effect of anomalous dispersion as discussed in section 4.5.

The critical angle corresponds to the maximum in the fluorescence signal.

The angle of incidence was chosen to be $\varphi=0.75\varphi_c$ in order to maximize both signals (obtain reasonable counts for both the reflectivity and the fluorescence), and to minimize any effects due to anomalous dispersion of the amplitude or phase of the ultrathin samples [2,3].

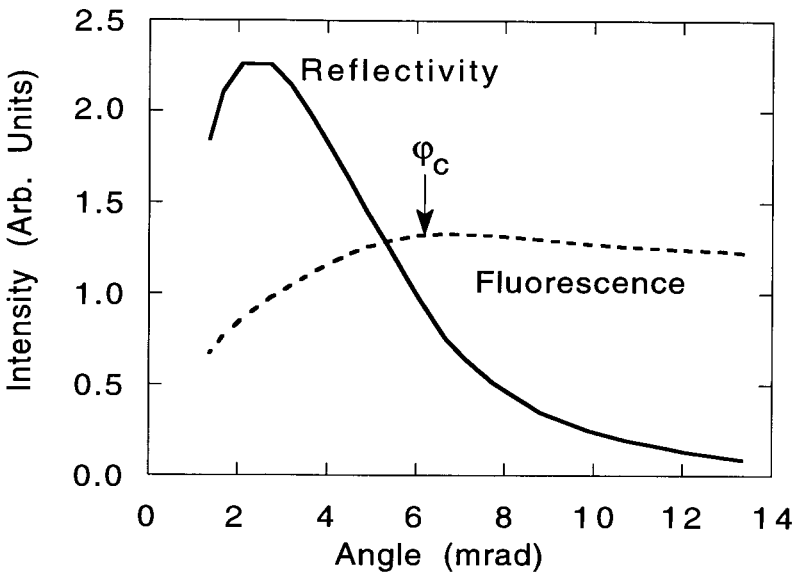

Figure 4.4. Intensity of the fluorescence and the reflectivity as a function of angle of incidence at E_0+200 eV.

4.4. Fluorescence Detection

4.4.1. Fluorescence Detector

A large aperture gas ionization chamber [4] placed about 5cm from the sample (giving a solid angle of about 130°) was used to measure the fluorescence signal leaving the thin layer of interest in the sample. Figure 4.5 shows a schematic view of the detector. It was designed to work as an ionization chamber, and took into account the need for high sensitivity when measuring ultrathin layers. The fluorescence photons enter the chamber from the thin aluminized mylar aperture and ionize the N_2 or Ar_2 gas molecules in the chamber. The resulting ions move towards and are collected by the biased Ni mesh which makes up the detection part of the chamber. They then generate a current pulse in the preamplifier, which is converted by a voltage to frequency converter, whence the signal will be recorded by the computer.

The ionization chamber used for the reflectivity measurements was placed about 60cm from the sample. It was built in the same fashion as the fluorescence chamber described above, but detected only photons reflected from the surface of the sample.

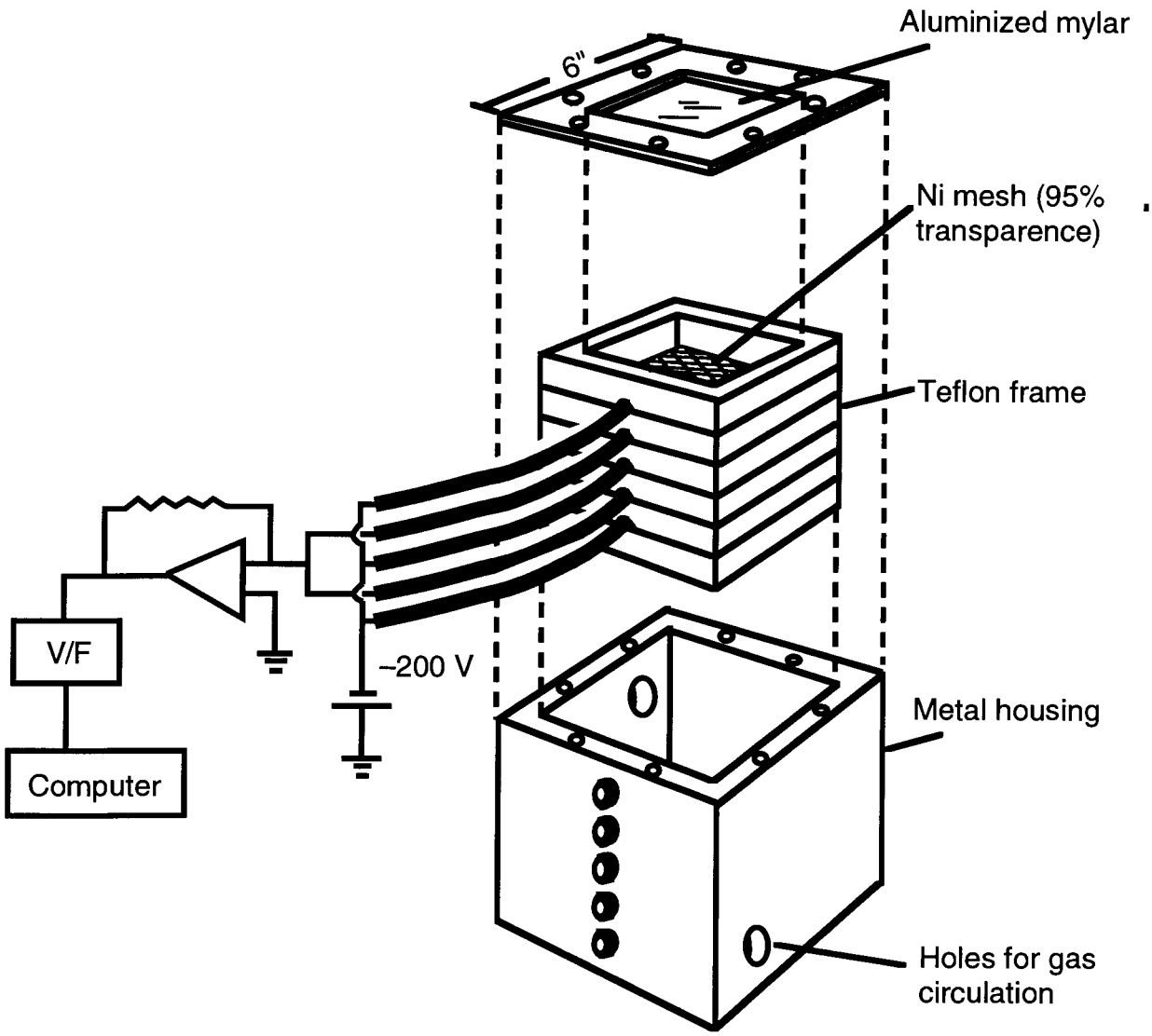

Figure 4.5. Fluorescence detection chamber [2].

4.4.2. Bragg peak elimination

Sudden peaks in the photon counts were observed as the energy was increased each time the conditions for Bragg's law were satisfied within the solid angle of detection. These peaks are not

part of the XAFS spectrum though they are inherent to the crystal substrate and epitaxial layers. The geometry of the set-up, including the azimuthal angle with which the beam crosses the sample's surface, may be changed slightly in order to inhibit certain reflections (or peaks). The peaks that cannot be eliminated in this manner must be dealt with in other ways.

In one instance, it is possible to block all radiation which satisfies Bragg's law as it leaves the sample. In order to do so we determined at what energy the peak occurred (one verifies that it is indeed a Bragg peak by noting its absence from the reflectivity spectrum) and placed an x-ray film (Polaroid 52) in front of the sample, exposing it at that energy. The areas of the film which were exposed correspond to the areas of the detector that must be blocked with lead (Pb) tape. To this end a clear mylar window in an aluminium frame was placed above the detector shown in Fig. 4.3.

This avoids having to put lead tape directly on the detector, which would unnecessarily diminish the solid angle available at other absorption edges. The film could be mounted just under this window (by sliding it into the frame), and the positions of the pieces of tape that were required to block the Bragg radiation are thus determined.

Another technique for eliminating Bragg peaks is to remove them from the raw data [5]. If data is available for several tilt angles of the sample, or several azimuthal angles, it will be possible to remove the peaks by interpolating a straight line with the appropriate background through the data signal. This works because

the energy positions of the peaks changes with changing angle of incidence. It is once again necessary to double check their absence in the reflectivity spectrum.

In this fashion, the samples were aligned and the spectra deemed free of Bragg peaks. Once the range of energies appropriate to the edge in question have been determined, one simply acquires as many spectra as are necessary to reduce the noise by signal averaging.

4.5. Model calculations of the fluorescence

In order to measure the XAFS of ultrathin multilayers a total reflection geometry was used. As a result, the x-rays are incident on the sample at an angle which is inferior to the critical angle of the material. An expression of the dispersion of the radiation in the material in terms of its electric field will provide the intensity of the fluorescence emanating from the sample. It proves useful to calculate the penetration depth of the radiation and to insure that the films of interest are close enough to the surface of the multilayer to give a significant fluorescence.

Assuming the velocity of the electron to be non-relativistic, the effect of the magnetic vector of the incoming x-rays will be neglected. The thin films are therefore considered to be non-magnetic (μ=1) and the effect of the electric field of the radiation is of primary concern. Adopting a simple model of the solid, fixed independent neutral atoms where the electrons are bound, the

complex dielectric constant of the radiation can be expressed as [6,7]:

$$(4.1)\quad \varepsilon = 1 + \sum_{q} \frac{4\pi n_q e^2}{m\left[\omega_q^2 - \omega^2 + i\gamma_\omega \omega\right]}$$

where n_q is the number of q type electrons per unit volume, $\gamma_\omega = 2e^2/3mc^3$ is the radiation damping term, ω_q is the natural frequency of the electron (q=K,L,M, etc), m the mass of the electron, and q its charge, and ω the frequency of the exciting radiation. The index of refraction is then $n=\sqrt{\varepsilon(\omega)}$, and rewriting in terms of the atomic-scattering factor $f=f_0+f'+if''$ [6,7], where f_0 is equal to the atomic number (the number of electrons in the isolated atom) in the coherent forward-scattering case, and f' and f'' are the real and imaginary anomalous scattering corrections gives:

$$(4.2)\quad n = 1 - \delta - i\beta$$

In Eq. 4.2, the values of δ and β are given by:

$$(4.3.a)\quad \delta = \frac{N_0}{2\pi} \frac{e^2}{m_e c^2} \frac{\rho}{M} \lambda^2 \, (f_0 + f')$$

$$(4.3.b)\quad \beta = \frac{N_0}{2\pi} \frac{e^2}{m_e c^2} \frac{\rho}{M} \lambda^2 \, f''$$

where ρ is the mass density of the material, N_0 is Avogadro's number, λ is the wavelength of the incoming x-rays, M the atomic weight, e the charge of the electron, and m_e its mass. The anomalous scattering factors f' and f'' were computed with the Cromer and Liberman anomalous scattering factor program [8-10]. The values of the critical angle for total reflection can be calculated using Eq. 4.3:

(4.4) $\varphi_c=\sqrt{2\delta}$

This gives the critical angles shown in Table 4.1 at the K-edges of the multilayer sample containing 6ML of Cr (Fe/Cu/6 Cr/3 Cu/5 Fe)

Table 4.1. Critical angles calculated at 200eV above the K-edge, for the 8.7 Fe/3 Cu/6 Cr/3 Cu/5 Fe sample.

EDGE	φ_c(mrad)
Fe	8.8
Cu	7.0
Cr	10.2

The critical angles correspond to the maxima in the plots of the fluorescence intensity as a function of angle shown in Fig. 4.6 for the various edges, calculated at the K-edge energy E_0, and E_0+200eV, for the entire multilayer structure.

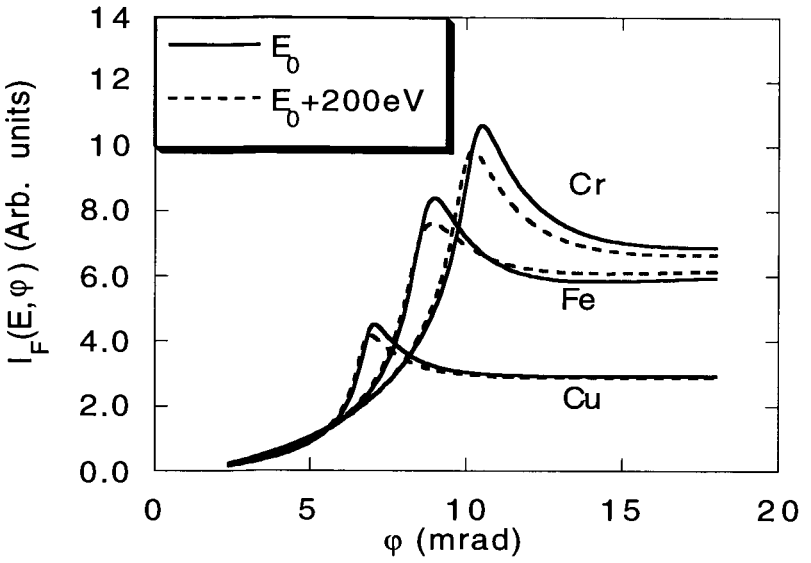

Figure 4.6. Fluorescence as a function of angle of incidence for E_0 and E_0+200 eV for the Cu, Fe and Cr edges in the 8.7 Fe/ 3 Cu/6 Cr/3 Cu/5 Fe sample.

The value of the intensity of the fluorescence was found by integrating the magnitude of the electric field throughout the sample [7,11]:

$$(4.5)\quad I_F(\lambda,\varphi) \propto \int_0^{\infty} \sum_j \eta_j(z)\mu_{\rho j}(z)\rho(z)|E_{total}(\lambda,\varphi,z)|^2 dz.$$

The amplitude of the electric field in a stratified system was obtained from the work done by D.T. Jiang [7,11]; μ_ρ and ρ are the mass absorption coefficient and mass density respectively, η is the fluorescent yield which is the probability that a core-hole results in a fluorescence event. The summation in Eq. 4.5 is over different

absorption edges. We have set $\eta_j(z)$ equal to unity. The attenuation of I_F along the escape path from the sample was neglected. This is justified by the fact that most of the photons entering the fluorescence detector travelled less than 100Å while leaving the sample. This is much less than the bulk absorption length of a few microns.

In this manner it was found that the intensity of the total electric field in the sample had dropped sufficiently by the time the x-rays reached the lower layers of Cu that any fluorescence emanating either from the lower Cu, or Fe layers could be neglected.

In Fig.4.7, the experimental curve of the fluorescence is compared to the calculated one. The experimental curve has its peak at ~8.7 mrad, which is comparable to the calculated value of 8.8mrad. The data were taken at 0.75 of the experimental value, 6.5mrad. This appears to be at a rather low value of the calculated fluorescence intensity, though not on the experimental curve. The intention was to avoid any anomalous dispersion, caused by the frequency dependence of δ, which occurs near the critical angle.

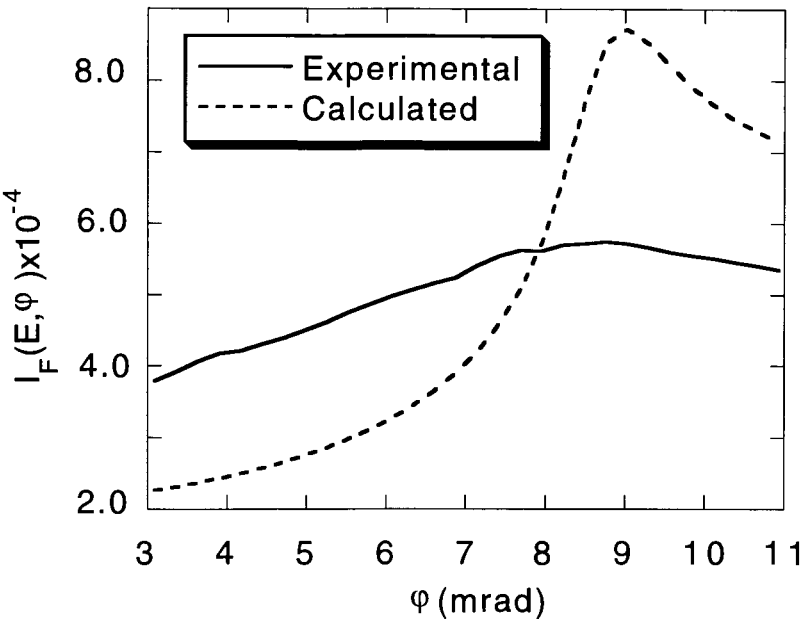

Figure 4.7. Comparison of the Fe experimental fluorescence and the calculated as a function of angle of incidence at E=7112+200eV.

CHAPTER V: DATA ANALYSIS OF MBE FILMS

This chapter on the data analysis of MBE grown films is divided in four main sections. In the first the x-ray absorption near-edge structure (XANES) of the K-edges in the 8.7 Fe/3 Cu/6 Cr/3 Cu/5 Fe MBE sample are discussed.

In the second section, the interference function $\chi(k)$ and its Fourier transform, (FT($k\chi(k)$), for the various absorption edges of the samples, are compared to corresponding functions for reference structures, BCC or FCC as the case warrants. This comparison permits a first approximation to the structures. The data for the reference structures were obtained by the transmission of the x-rays through a thin (close to an absorption length) metal foil. Through beating analysis of the first peak of each Fourier transform, it was determined whether this peak was formed by the interference of one or two shells of atoms. From the same analysis, the separation (in Å) of the shells was estimated.

In the third section the fitting of the data from the MBE films is described. The data which was fit in the thesis as a whole can be divided into three categories. There were the foils, which are bulk polycrystalline samples of Cu, Cr and Fe, taken in transmission and for which the polarization of the x-rays is not important. They were fit, as outlined in Appendix A, to Eq. 2.15 for which Eq.2.8 (N_j^*) averages out to N_j. The second series is that of the RF sputtered films. They were also fit to Eq. 2.10 as they are polycrystalline, and the fit results are detailed in Chapter VI. The third set of samples are the MBE samples which are oriented single crystals, which were

analysed with the electric vector of the x-rays parallel to the Ag(100) axis. The first neighbours peaks of their FT were fit in R-space, to Eq. 2.7, using a non-linear least-squares program called EXAFIT [1]. The samples were first fit to a polarization independent model $\chi(k)$ which was later refined to include the polarization dependence of their structures. Since the films are seen, in Section 1 and 2 of this chapter, to be close to BCC the amplitudes and phases for the BCC structures are used to fit the first neighbour peaks. In a perfect BCC structure there is no effect of polarization dependence on the amplitudes and phases. In the more refined fitting scheme the results of the polarization-independent fits are used as input for a polarization dependent model. The polarization of the electric field of the x-rays was parallel to the Ag(001) surface as is shown in Fig. 5.1. The polarization dependence was included for all the body-centered tetragonal (BCT) MBE films using FEFF6.10 with the E vector in the <110> direction. This direction coincides with the "*a*" axis of the substrate, the <110> axis of the films, since the first layers of BCC Fe grow with a 45° rotation with respect to the underlying Ag(001) substrate, as is shown in Fig. 5.1.

Polarization-dependent modelling of the various shells is outlined in the fourth section.

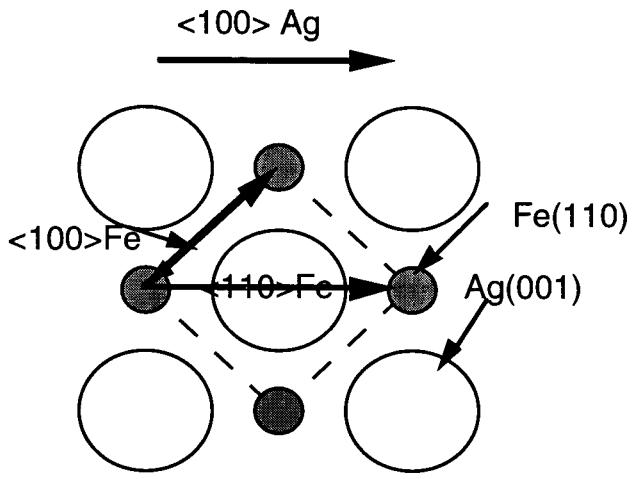

Figure 5.1. The polarization direction of the electric field. The $\vec{E}$ vector is along Ag(100) and parallel to the <110> of the films.

5.1. X-ray absorption near-edge structure of the 8.7 Fe/3 Cu/6 Cr/ 3 Cu/5 Fe MBE sample

The XANES, obtained in fluorescence mode, of the Cr K-edge in the 8.7 Fe/3 Cu/6 Cr/3 Cu/5 Fe sample and its normal BCC phase in a foil are plotted in Fig. 5.2.(a) Here the element which is underlined refers to the K-edge being probed. In Fig. 5.2.(b) the XANES of the Fe edge is compared to normal BCC Fe (foil) whereas in Fig. 5.2.(c) the Cu edge is compared with normal FCC Cu (foil). The Cr resembles the BCC Cr in the main features of the XANES, though they are somewhat attenuated in the thin film. Fe shows the main edge features present in the bulk. In the case of Cu it is quite obvious that the structure is not FCC as it is in the bulk, but resembles BCC.

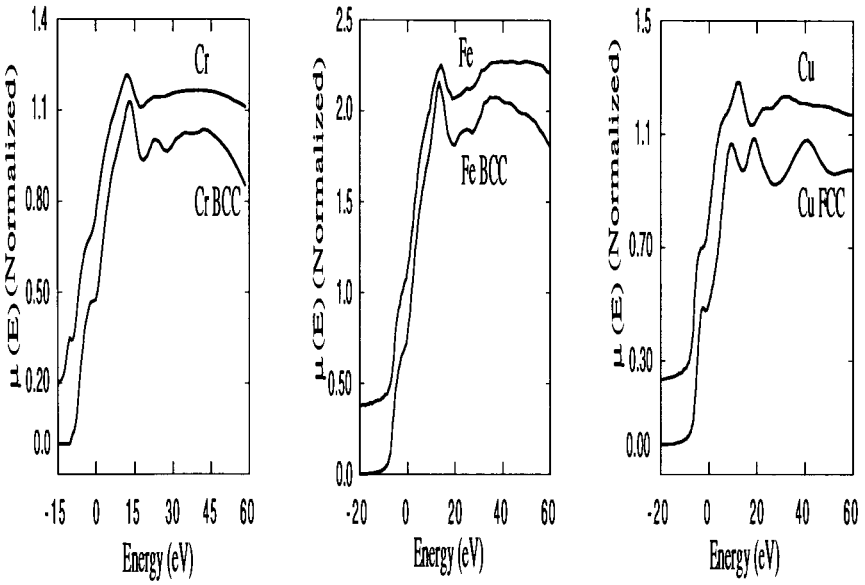

Figure 5.2. The XANES of 6 ML Cr and Cr BCC (a), 5 ML Fe and Fe BCC (b), 3 ML Cu and Cu FCC (c). The 8.7 Fe/3 Cu/6 Cr/3 Cu/5 Fe sample is compared to the bulk elements.

5.2. Comparison of the $\chi(k)$ and FT($k\chi(k)$) and Beating Analysis

The spectra have been divided into two groups. The first involves the two samples of multilayers composed of Fe/Cu/Cr/Cu/Fe multilayers. The second section contains the results of the three films grown at room temperature directly on Ag (5ML Fe/ 10 Au, 4ML Cr/10 Au and 10ML Cr/10 Au).

5.2.1. The 8.7 Fe/3 Cu/6 Cr/3 Cu/5 Fe and 8.7 Fe/3 Cu/3 Cr/3 Cu/ 5 Fe samples

The signature of a BCC structure is contained in the region between 4 and 6$Å^{-1}$ in the XAFS interference function where two

distinctive peaks occur. Quickly comparing the XAFS interference functions of Fe BCC, shown in Fig. 5.3, and the upper 5ML of Fe in the 8.7 Fe/3 Cu/6 Cr/3 Cu/5 Fe (denoted Fe 6ML corresponding to the uppermost 5ML of Fe of the multilayer shown in Chapter III, Fig. 3.1) we see that all the main features are present in the film. Some minor structures, such as the small bump on the side of the peak between 2 and 4Å^{-1}, are also present in the $\chi(k)$ of the film. There is less amplitude in the overall spectra of the film. It can be seen, comparing with the interference function of Cu FCC in the lower part of Fig. 5.5, that the Fe 6ML is very different from an FCC structure. The Fe grew in a BCC structure, and, since the frequency of $\chi(k)$ is similar to that of the foil, the positions of the atoms will be close to those of BCC Fe.

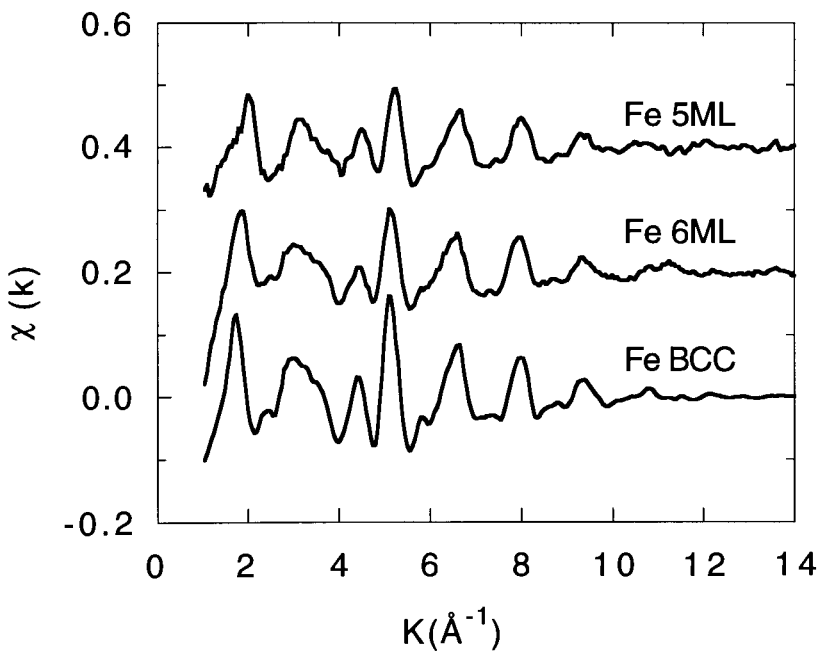

Figure 5.3. $\chi(k)$ of Fe BCC, Fe 6ML edge in 8.7 Fe/3 Cu/6ML Cr/ 3 Cu/5 Fe sample, and Fe 5ML edge in 5ML Fe/10 Au sample.

The spectrum corresponding to 5ML of Fe deposited at RT on Ag(001) also shows all the main BCC features. It greatly resembles the interference function obtained for the Fe edge in the 8.7 Fe/3 Cu/ 6 Cr/3 Cu/5 Fe sample, indicating once again a BCC structure with lattice parameters close to those found in bulk Fe.

The interference spectra from the Cr edge of the 8.7 Fe/3 Cu/3 Cr/ 3 Cu/5 Fe and 8.7 Fe/3 Cu/6 Cr/3 Cu/5 Fe films are shown in Fig. 5.4 alongside that of BCC Cr. As was the case for the Fe edge in the 6ML Cr sample, there are two peaks present in the region from 4 to 6$Å^{-1}$, indicating a BCC structure. Most of the other BCC features are present in the spectra though they are heavily attenuated in the case of the 3ML Cr (for example, the peak from 2 to 4$Å^{-1}$ is flattened possibly implying some different structural contributions). In the low k region both films exhibit a larger amplitude oscillation than that of the bulk BCC foil. Though the features of a BCC structure are present, they are distorted, and the frequencies are different from those of the BCC spectra. We would therefore expect a distorted BCC structure. The possibility that the interference changes are associated with the Cu over- and underlayers is considered in section 5.3.1.a. The peak at 8$Å^{-1}$ in the 3ML of Cr is not a Bragg Peak: it is present in the $\chi(k)$ from data for three different azimuthal angles and two different angles of incidence. The same holds true for the region from 10.2 to 12$Å^{-1}$, in both the 3ML and 6ML of Cr data.

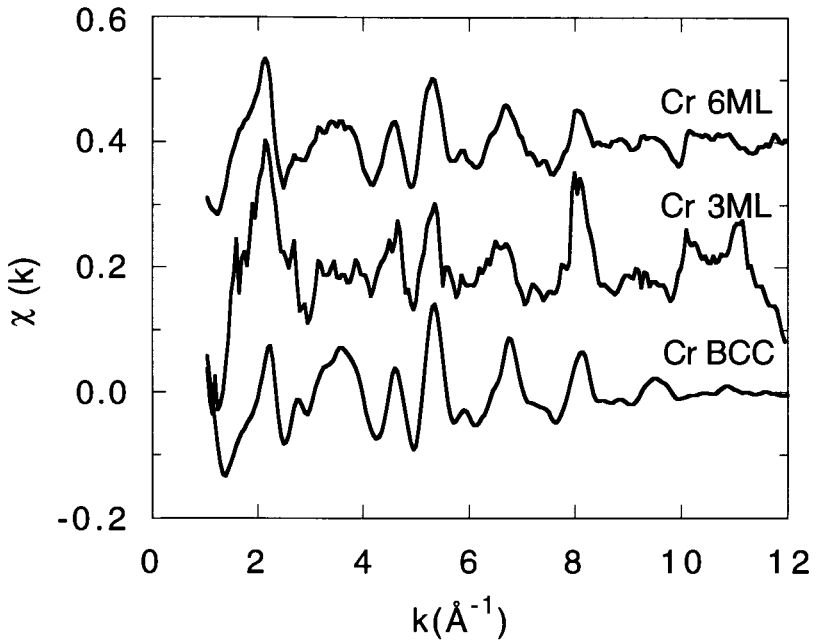

Figure 5.4. χ(k) of Cr BCC, Cr edge in 8.7 Fe/3 Cu/6 Cr/3 Cu/5 Fe, and 8.7 Fe/3 Cu/3 Cr/3 Cu/5 Fe samples.

The lower spectrum of Fig. 5.5 shows the interference function from a bulk FCC Cu foil. In this spectrum there is only one peak in the region from 4 to 6Å^{-1}. The Cu in both films (Cu edge in 8.7 Fe/ 3 Cu/6 Cr/3 Cu/5 Fe sample, and 8.7 Fe/3 Cu/3 Cr/3 Cu/5 Fe sample) shows two distinct peaks in this region, as is the case for the BCC Fe standard shown above. There are some similarities to the Fe foil, though the overall amplitude is greatly diminished. An important difference is this low k region, where the films resemble each other but neither the Cu FCC nor the Fe BCC foils. A quick analysis leads to the conclusion that the structure is a distorted BCC.

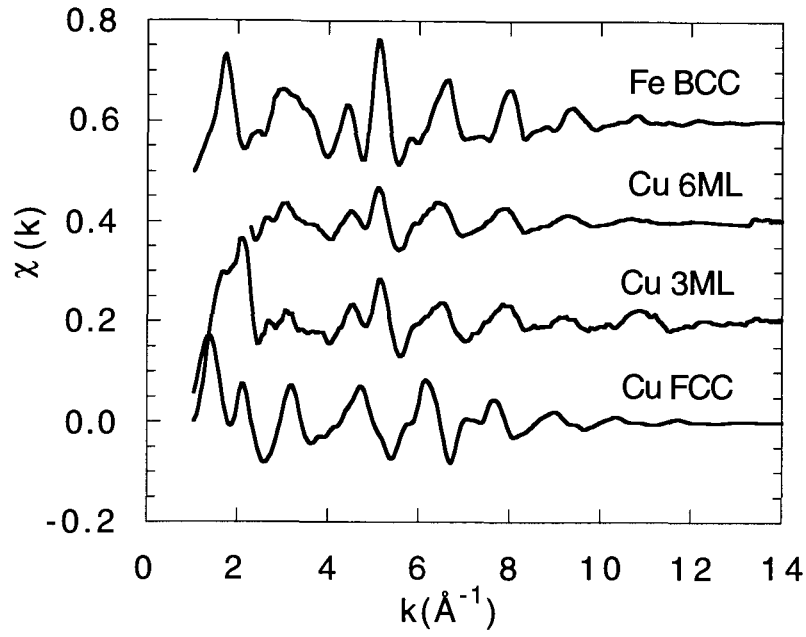

Figure 5.5. χ(k) of Cu FCC, Cu edge in 8.7 Fe/3 Cu/3 Cr/3 Cu/5 Fe sample, and 8.7 Fe/3 Cu/6 Cr/3 Cu/5 Fe sample, with Fe BCC as a comparison.

In Fig. 5.6 the spectra of the Cu edge in the 8.7 Fe/3 Cu/3 Cr/ 3 Cu/5 Fe sample has been plotted for two polarizations of the incident x-rays electric vector ($\vec{E}$ parallel and perpendicular to the sample's surface). In both polarizations the spectra show two peaks between 4 and 6Å^{-1}, confirming that the structures are BCC to a first approximation. However, the shape of the peak from 2 to 4Å^{-1} is greatly changed from that of the bulk, most likely demonstrating some distortion of the structure. The two Cu spectra show some differences in the same region, and the amplitude of the Cu 3ML with the electric vector of the radiation parallel to the film is smaller than that with the electric vector perpendicular to it.

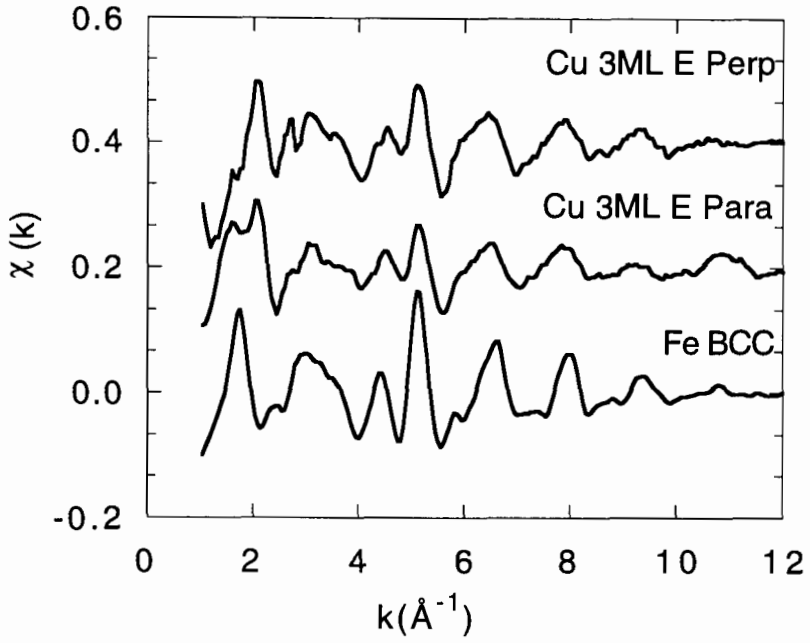

Figure 5.6. $\chi(k)$ of Fe BCC, Cu edge in 8.7 Fe/3 Cu/3 Cr/3 Cu/ 5 Fe sample with the $\vec{E}$ vector of the incident x-rays parallel (Para), and perpendicular (Perp) to the surface of the sample.

Further qualitative analysis can be done by observing the FT of the spectra of the samples. The differences and or similarities are more pronounced in the Fourier transforms of the interference function $\chi(k)$. In Fig. 5.7 we have the magnitude of the FT($k\chi(k)$) of an Fe foil showing the first peak which is the sum of the peak of the first nearest neighbours (the 8 body centers in the case of a BCC structure) and the second nearest neighbours (the 6 atoms on the corners of the cube). It must be pointed out at this point that the FT have not been corrected for the XAFS phase shift, so the arrows on the graphs do not correspond exactly to the real radial distances. We can see that the FT for the films (Fe, Fe in 8.7 Fe/3 Cu/6 Cr/3 Cu/

5 Fe, Fe in 5 Fe /10 Au) shows a wider (or broader) and smaller peak than that of the bulk BCC structure of Fe. There may be either more disorder in this structure than in the foil, or, the first two shells may be further apart than they are in BCC Fe. The high-R side of the first peak is as distinct as in the foil, and the higher shells are also very distinct. The structure is BCC, though not identical to that of the foil, and demonstrates good medium range order (0-5Å).

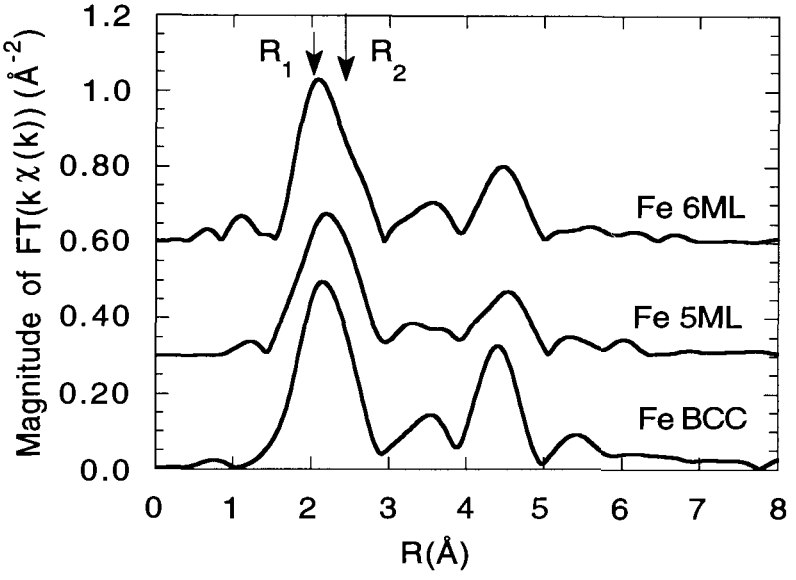

Figure 5.7. Magnitude of the FT(kχ(k)) for Fe BCC, 5ML of Fe in 8.7 Fe/3 Cu/6 Cr/3 Cu/5 Fe, and the Fe edge in the 5 Fe/ 10 Au sample. k space range: 1.45to 14.00Å^{-1}. A 10% Gaussian window was applied (Eq. 2.14.b). The arrows indicate the positions of the first two shells of a BCC structure (the XAFS phase shift has not been removed.)

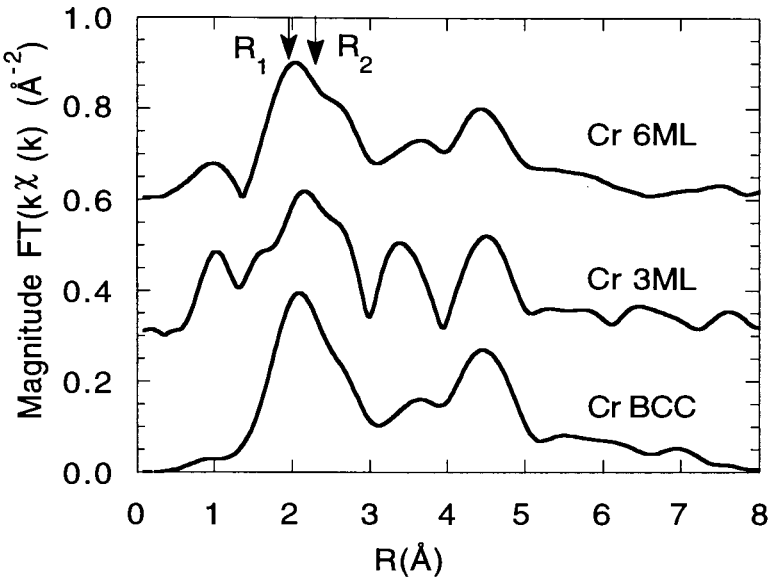

Figure 5.8. Magnitude of the FT(kχ(k)) for Cr BCC, and the Cr edges in the 8.7 Fe/3 Cu/6 Cr/3 Cu/5 Fe and 8.7 Fe/3 Cu/3 Cr/3 Cu/ 5 Fe samples. Range in k-space: 1.54 to 10.15 Å^{-1}. A 10% Gaussian window was applied (Eq. 2.14.b). The arrows indicate the positions of the first two shells of a BCC structure (the XAFS phase shift has not been removed.)

The Cr edge of the 8.7 Fe/3 Cu/6 Cr/3 Cu/5 Fe sample shows a broad and low intensity first peak in Fig. 5.8, with the two higher peaks resembling those of a BCC structure. Both the 3ML of Cr and the 6ML of Cr show a reduced amplitude of the first peak, as compared to the perfect BCC structure. However, the higher shells seem to have similar intensities to those of BCC Cr. In both cases the structure is a distorted BCC. The low R region (~ 1Å) in the 3ML Cr is due to residual low frequency background content of the XAFS, which the background removal scheme failed to eliminate.

The FT of the Cu edges in the 8.7 Fe/3 Cu/3 Cr/3 Cu/5 Fe and 8.7 Fe/3 Cu/6 Cr/3 Cu/5 Fe samples are shown in Fig. 5.9. Comparison shows that the positions of the first nearest neighbours are the same. The first peak is, however, broader for the case of the 3ML Cr sample than for the Fe foil, which is shown as a comparison. Both films show good medium range order as is evident by the intensity of the peaks from 4 to 5Å. The reduction in amplitude may indicate an increased structural disorder or a lower coordination in the films than in the BCC foil. The surface to volume ratio is sufficiently big that the average coordination in the film is less than in the infinitely thick bulk crystal

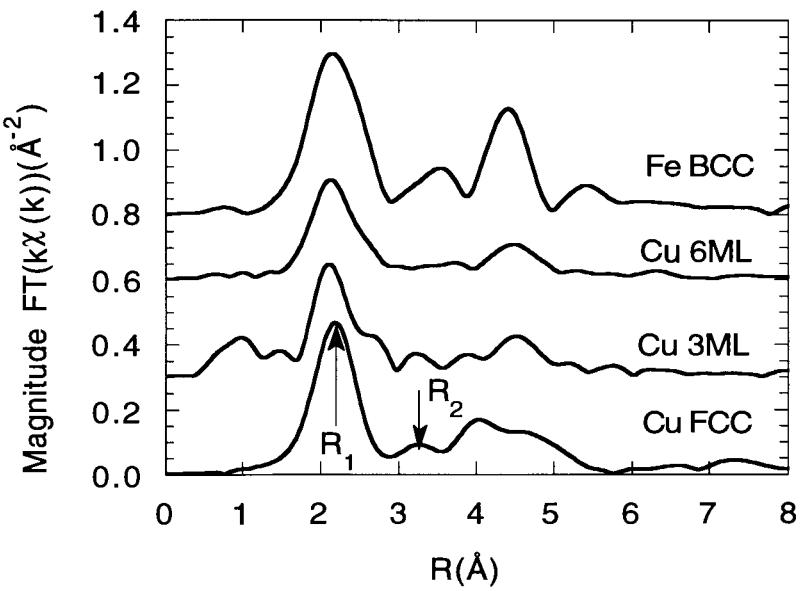

Figure 5.9. Magnitude of the FT(kχ(k)) for Cu FCC, and the Cu edges in the 8.7 Fe/3 Cu/6 Cr/3 Cu/5 Fe (Cu 6ML) and 8.7 Fe/3 Cu/3 Cr/3 Cu/5 Fe (Cu 3ML) samples with Fe BCC as a comparison. The k space range: 1.35 to 14.00Å^{-1}. A 10% Gaussian window was applied (Eq. 2.14.b). The arrows indicate the positions of the first two shells of an FCC structure, including the XAFS phase shift.

The FT of the $\chi(k)$ for the Cu edge for both polarization states shows (Fig 5.10) a first peak occurring at the same distance. The structure seems somewhat distorted in the plane of the surface of the sample ($\vec{E}$ Parallel), and less so in the direction of growth ($\vec{E}$ Perpendicular). More discussion of the effect of polarization is to be found in the curve fitting section for this sample (Chapter 5, Section 2.1).

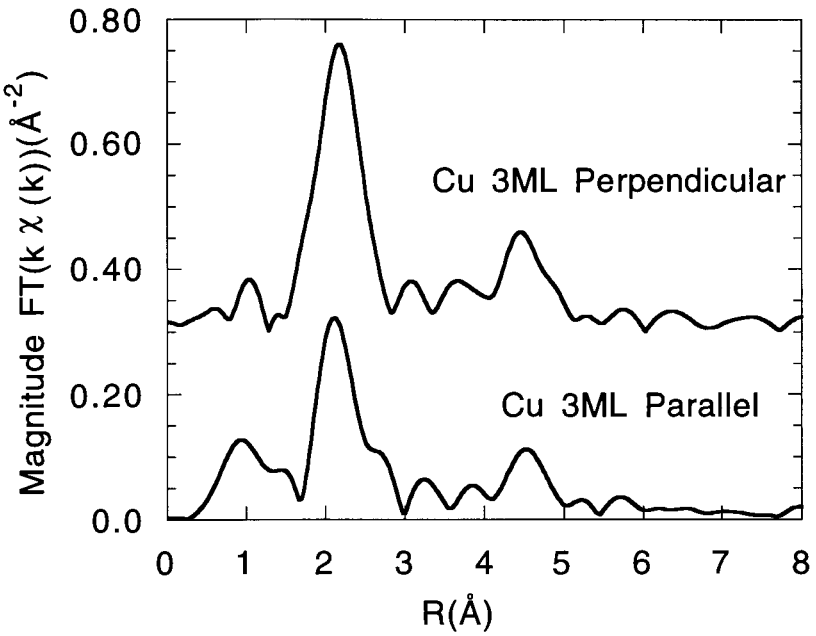

Figure 5.10. Magnitude of the FT($k\chi(k)$) for Cu in the 8.7 Fe/3 Cu/3 Cr/3 Cu/5 Fe sample, with the polarization vector of the electric field parallel, and perpendicular to the sample's surface, k space range: 2.40 to 14.25 $Å^{-1}$. A 10% Gaussian window was applied (Eq. 2.14.b)

From the Fourier transforms (FT) of the BCC metals examined so far, the first two shells of the BCC structure cannot be resolved. Both the first nearest neighbours (body centers) and the second nearest neighbours (corners of the cube) give rise to intensity under the first peak of the transform in their bulk BCC phases. The separation of these two shells is $\Delta R=0.386$Å for Cr and 0.384Å for Fe, where $\Delta R=R_1-R_2$. The presence of two shells under the first peak, as well as their separation, can be examined by beating analysis [2]. The data is back-transformed over the range of the first peak in R-space in order to isolate the amplitude and phase of the two combined shells. For two shells of identical scatterers the XAFS can be expressed in the following manner (equation 5.1) [3,8].

$$(5.1)\quad \chi(k)=\frac{1}{k}\tilde{A}\sin(2k\tilde{R}+\tilde{\phi}(k))$$

$$\tilde{A}(k)=A_1(k)\left[1+C(k)^2+2C(k)\cos(2k\Delta R)\right]^{1/2}$$

$$\tilde{\phi}(k)=\phi(k)+\tan^{-1}\left[\frac{1-C(k)}{1+C(k)}\tan(k\Delta R)\right]$$

In Eq. 5.1, the subscript 1 refers to the first shell, $\tilde{R}=(R_1+R_2)/2$ is the mean bond length of the shells, and the backscattering amplitude of shell 2 is designated by $A_2(k)=C(k)A_1(k)$.

Where there is no knowledge of either the backscattering amplitudes, or the phases for each shell individually, ΔR is found approximately from the minima or maxima occurring in the derivative of the phase of the back-transformed $\chi(k)$ with respect to k. Minima or maxima

will appear in the derivative due to the interference from the two shells. The positions of the kinks is given by the expression in Eq. 5.2.

$$(5.2)\quad k_{(n+1)} \simeq \frac{(2n+1)\pi}{2\Delta R} \qquad n=0,1,2,...$$

The so-called "beat nodes" correspond to changes of slope (kinks) in the amplitude or phase of the first peak of the Fourier transform. From the above equation (Eq. 5.2), it is straightforward to determine that all precision in ΔR is limited by the range of k-space data available. A quick rule of thumb is that $\Delta R \Delta k > 10$ will give us ΔR to within 0.02Å.

For the derivative of the phase shown in Fig. 5.11 the first beat occurs at 3.74 $Å^{-1}$ which gives ΔR=0.42Å, for both Fe BCC and Fe 6, which corresponds to the upper 5ML of Fe in the 8.7 Fe/3 Cu/6 Cr/ 3 Cu/5 Fe sample. The two first shells of the Fe edge in the 6ML of Cr sample are therefore expected to be separated by the same distance as that found in bulk BCC Fe.

Figure 5.12 shows the derivative of the phase of the first peak of the Cr edge from the two multilayer samples, 8.7 Fe/3 Cu/6 Cr/ 3 Cu/5 Fe and 8.7 Fe/3 Cu/3 Cr/3 Cu/5 Fe, as well as that of Cr BCC, which is expected to show a ΔR=0.386Å. It is found that the shape of the derivative for Cr 6ML and Cr BCC are similar, and that the beats are at values that give ΔR of 0.47Å for Cr 6ML, and 0.44Å for Cr BCC. The position of the beat in the derivative of the phase for Cr 3ML

gives a ΔR=0.40Å. This value is limited by the short range of data available, and may therefore only be within 20% of the real value in the film.

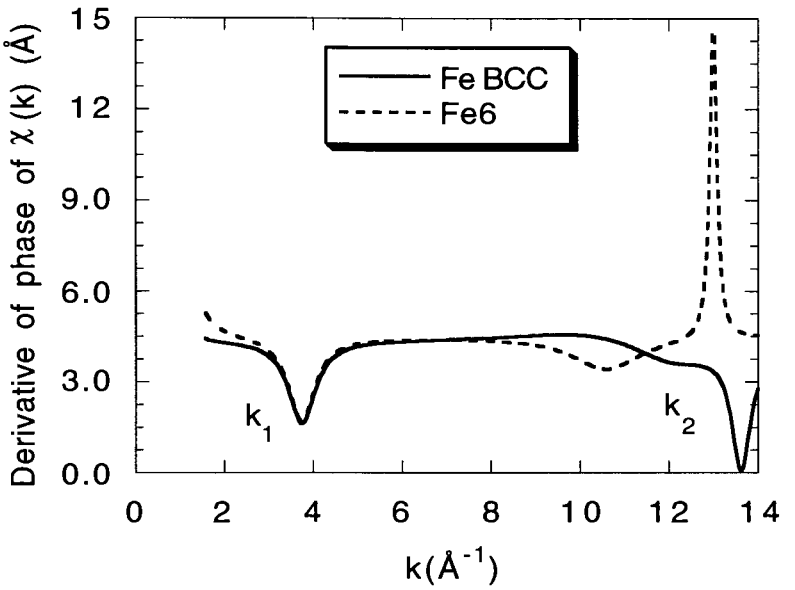

Figure 5.11. Derivative of the XAFS phase extracted from the FT of $k\chi(k)$ with a 10% Gaussian window over a k-space transform range from 1.50 to 14.20Å^{-1}. The filtered range in R-space was 1.5 to 2.86 Å. The first beat node, k_1, is at 3.74 for Fe 6ML, and 3.74 Å^{-1} for Fe BCC, k_2 is at 13.02 and 13.63 Å^{-1} respectively. Fe 6 refers to the upper 5 ML of Fe in the 8.7 Fe/3 Cu/6 Cr/3 Cu/5 Fe sample.

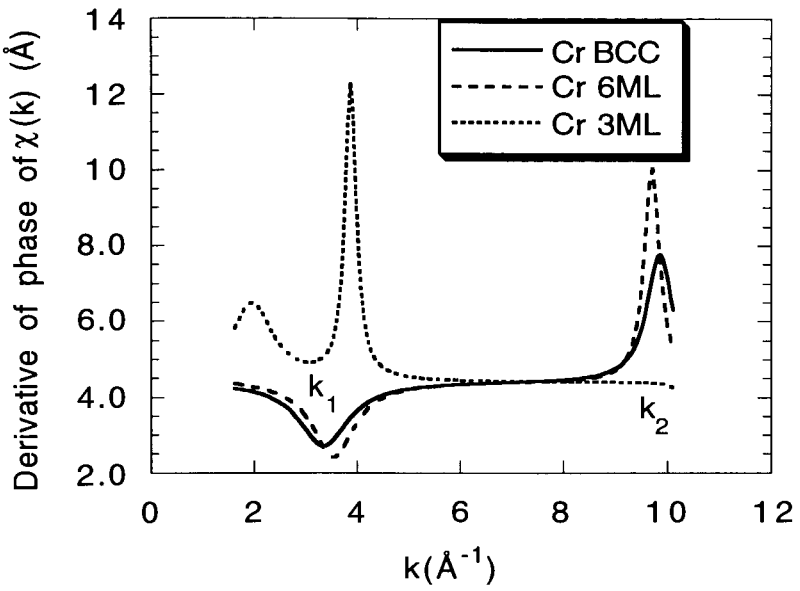

Figure 5.12. Derivative of the XAFS phase extracted from the FT of $k\chi(k)$ with a 10% Gaussian window over a k-space transform ranging from 1.55 to 10.15Å^{-1}. The filtered range in R-space was 1.65 to 2.75 Å. The first beat node, k_1, is at 3.58 for Cr 6ML, 3.89 for Cr 3ML and 3.36 Å^{-1} for Cr BCC, k_2 is at 9.71 and 9.89 Å^{-1} for Cr6 ML and Cr BCC respectively. Cr 6ML corresponds to the 8.7 Fe/3 Cu/6 Cr/3 Cu/5 Fe sample, and Cr 3ML to the 8.7 Fe/3 Cu/3 Cr/3 Cu/5 Fe sample.

The Cu in the 8.7 Fe/3 Cu/6 Cr/3 Cu/5 Fe sample (Cu 6ML) has grown in a BCC structure, therefore there are two shells present under the first peak of the FT. Figure 5.13 shows the derivative of the phase of the first peak, with beating at 3.60 and 3.72Å^{-1} for Cu 6ML and Fe BCC respectively, giving a ΔR=0.42Å and 0.40Å. These values are both precise to within ±0.02Å, which corresponds well to the range of available data. The two shells of Cu in the 6ML Cr

sample are therefore expected to be separated by roughly the same amount as the corresponding shells in Fe BCC.

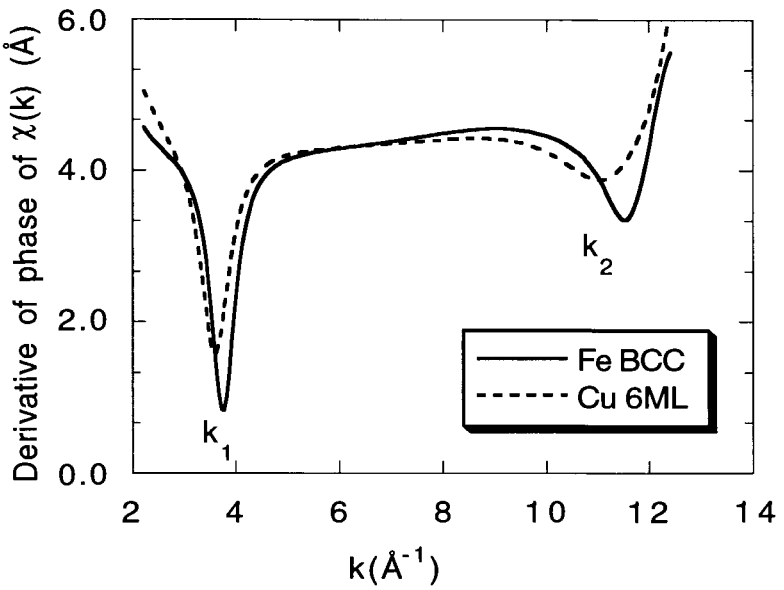

Figure 5.13. Derivative of the XAFS phase extracted from the FT of $k\chi(k)$ with a 10% Gaussian window over a k-space transform range from 2.13 to 12.46Å^{-1}. The filtered range in R-space was 1.3 to 2.84 Å. The first beat node, k_1, is at 3.60 for Cu 6ML (8.7 Fe/3 Cu/6 Cr/3 Cu/5 Fe), and 3.72 Å^{-1} for Fe BCC, k_2 is at 11.16 and 11.55 Å^{-1} respectively.

The spectra of the Cu edge in the 8.7 Fe/3 Cu/3 Cr/3 Cu/5 Fe sample were taken with the electric vector of the incident x-rays parallel and perpendicular to the sample's surface. In Fig. 5.14 the derivative of the phase is plotted for both these cases. The position of the beat gives a radial separation between R_1 and R_2 of 0.43Å when the electric vector is parallel to the surface, and 0.42Å when it

is perpendicular to it. The first peak does contain two separate shells, as is seen by the presence of a dip in Fig. 5.14.

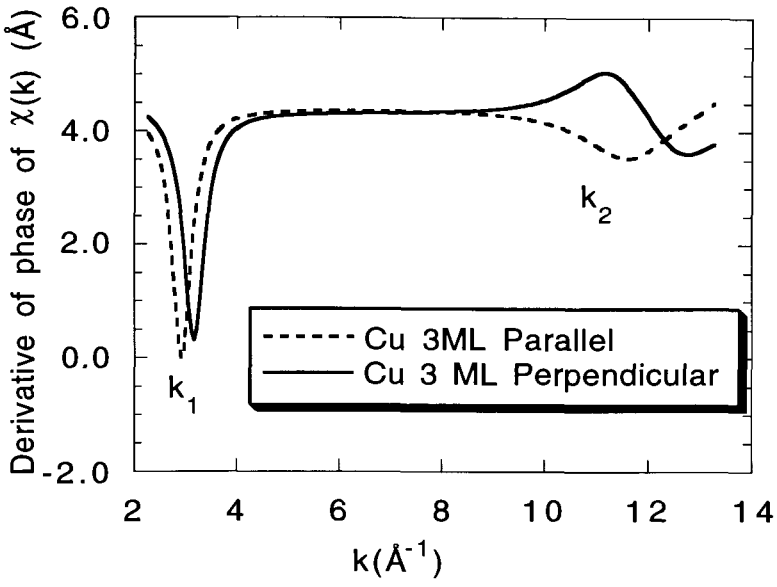

Figure 5.14. Derivative of the XAFS phase extracted from the FT of $k\chi(k)$ with a 10% Gaussian window over a k-space transform ranging from 2.20 to 13.30Å^{-1}. The filtered range in R-space was 1.58 to 2.72 Å. .The first beat node, k_1, is at 3.42 for Cu 3ML, and 3.17 Å^{-1} for Cu 3ML in $\vec{E}$ perpendicular, k_2 is at 10.94 and 11.28 Å^{-1} respectively. The Cu 3ML correspond to the upper Cu layers in the 8.7 Fe/3 Cu/3 Cr/3 Cu/5 Fe sample.

The beating analysis has given us a rough estimate of the separation of the first two shells of the Cu, Cr and Fe for the 8.7 Fe/3 Cu/6 Cr/3 Cu/5 Fe sample, and, the Cu and Cr for the 8.7 Fe/3 Cu/3 Cr/3 Cu/5 Fe sample. These values will prove useful in the first steps of the curve fitting of the first peak of each edge.

5.2.2. 4ML Cr/ 10 ML Au and 10ML Cr/ 10 ML Au samples

Figures 5.15 and 5.16 give the results of measurements from the Cr and Au edges for the Ag(001)/4ML Cr/10ML Au and the Ag(001)/10ML Cr/10ML Au samples. Though the Cr edge (Fig. 5.15) in the 10ML sample shows the two peaks (4 to 6$Å^{-1}$) of the BCC structure, it lacks oscillations in the 2 to 4$Å^{-1}$ region. The structure appears to be distorted. The 4ML Cr seems to lack structure entirely, though a semblance of two oscillations may be seen between 4 and 6$Å^{-1}$. It also appears to be distorted and attenuated, more so than the 10ML Cr. The Au structure in the films (Fig. 5.16) resembles that of FCC Au, to a first approximation. In both cases there is very little amplitude, and very few oscillations beyond 5$Å^{-1}$.

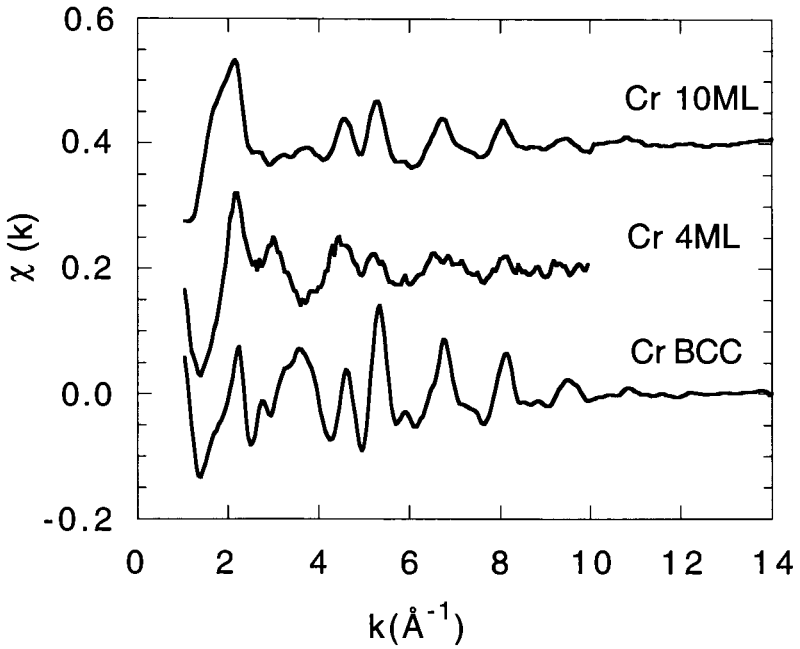

Figure 5.15. χ(k) of Cr BCC, Cr edge in 10ML Cr/10ML Au sample, and 4ML Cr/ 10ML Au sample.

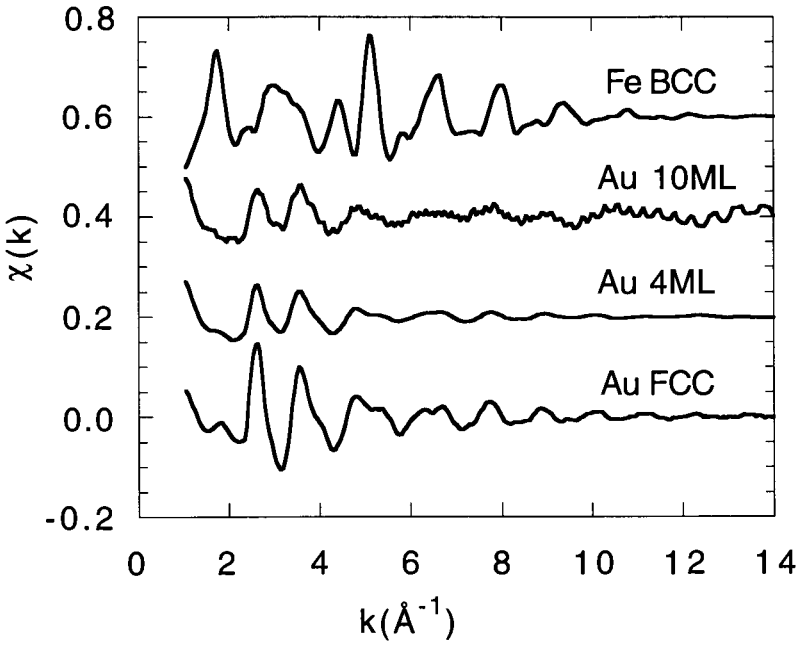

Figure 5.16. χ(k) of Au FCC, Au edge in 10ML Cr/ 10ML Au sample, and 4ML Cr/ 10ML Au sample. Fe BCC as a comparison.

The Fourier transforms of the Cr and Au edges (shown in Fig. 5.17 and 5.18) grown at RT on Ag demonstrate heavily distorted structures. Although the 10ML of Cr is that of a greatly disordered BCC structure, no argument can be made for the 4ML. The presence of peaks around 1Å in both spectra may possibly be attributed to scattering from heavier elements (such as Ag or Au). This is highly probable as the Cr and the Ag will intermix during the beginning of the deposition (see chapter III, section 1.3.d). In Fig. 5.18, the Au edges show the structures to be FCC to a first approximation. In both cases 10ML of Au were deposited on the Cr in order to passivate the surface. The Au will grow for 8-12 ML [4] at which point a reconstruction that corresponds to an FCC structure will be visible on the RHEED pattern. It can be argued, from the shape of the FT that the reconstruction does not seem to be complete after 10ML of deposition.

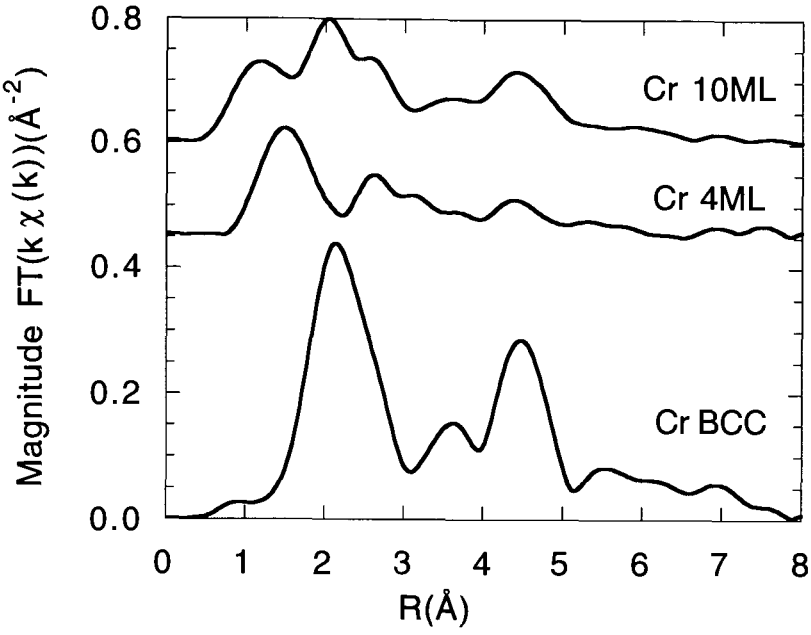

Figure 5.17. Magnitude of the FT(kχ(k)) for Cr BCC, and the Cr edges in the 4ML Cr/ 10ML Au, and 10ML Cr/ 10ML Au samples, k space range: 1.0 to 9.9Å^{-1}.

The derivatives of the phase for the first peaks of Cr 10ML and BCC Cr are shown in Fig. 5.19 to have a beat at 3.65Å^{-1}, which gives a separation of 0.43Å between the first two shells. The filtered range in R-space was 1.83 to 2.84 Å. The first beat node, k_1, is at 3.65 for both Cr in 10ML Cr/ 10ML Au and Cr BCC, and k_2 is at 9.84 Å^{-1}. This value is comparable to the value for BCC Cr over such a restricted range of data. To a first approximation, the Cr in the 10ML sample has two first shells which are separated by 0.43±0.02Å.

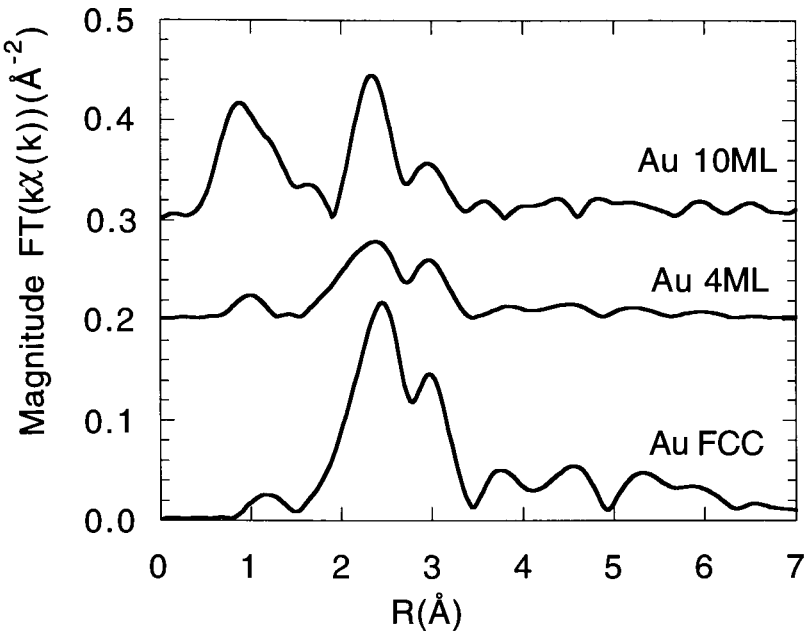

Figure 5.18. Magnitude of the FT(kχ(k)) is given for Au FCC, as well as the Au edge in the 4ML Cr/ 10ML Au and 10ML Cr/ 10ML Au samples. k space range: 2.40 to 13.2 Å^{-1}.

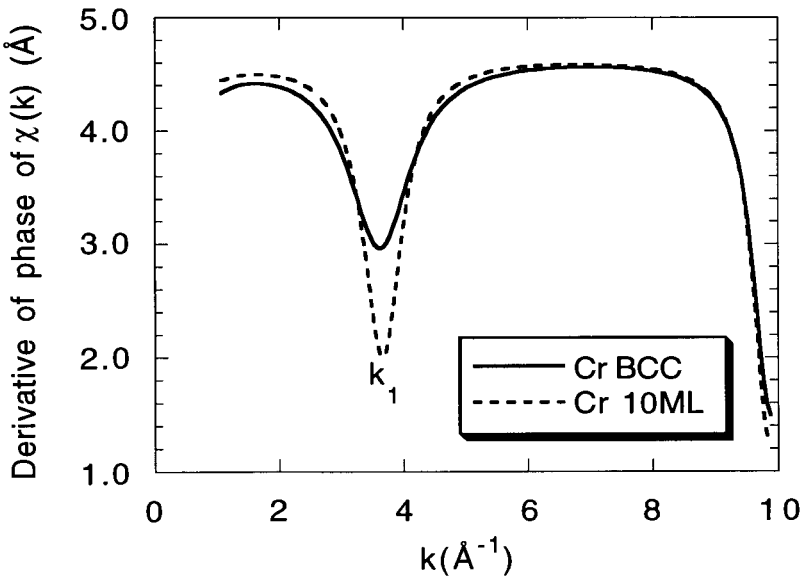

Figure 5.19. Derivative of the XAFS phase extracted from the FT of kχ(k) with a 10% Gaussian window over a k-space transform ranging from 1.00 to 9.90Å^{-1}.

5.3. Curve Fitting results

A fully detailed explanation of the least-squares fitting procedure used is given in Appendix A. There the fitting of the BCC Cr foil is described in detail. The fitting of its first neighbours peak shows the necessity of fitting to the triangular multiple scattering paths as well as to the first and second neighbours. This was not found to be the case for the BCC Fe, nor BCC Cu. In this section the fitting of the first neighbours peaks of the FT of the MBE films are described, the two samples containing 3ML and 6ML of Cr in a first instance (8.7 Fe/3 Cu/3 Cr/3 Cu/5 Fe and 8.7 Fe/3 Cu/6 Cr/3 Cu/5 Fe), and secondly the 5ML Fe/10ML Au and 10ML Cr/10ML Au samples.

The main steps involved in the fitting are given here in order to aid in the interpretation of the results contained in this section. The fitting of the data sets was done in R-space, simultaneously fitting the Real and Imaginary parts of the FT of the model to those of the data. The FT of both the data and the model were calculated in the same manner using the Fast Fourier Transform [2.13] in order to minimize transform artefacts. The program used is called EXAFIT [2.8], and the amplitudes and phases were calculated using FEFF6.10 [9]. The following expression was fit for the oriented single crystal MBE samples:

$$(2.7)\quad \chi^{\Gamma}(k) = \sum_{\Gamma} F^{\Gamma}(k) S_0^2(k) \frac{e^{\frac{-2R}{\lambda}}}{kR^2} e^{-2\sigma_{\Gamma}^2 k^2} \sin\left[2kR + \phi_T^{\Gamma}(k)\right]$$

where the summation over Γ implicitly includes a summation over the N_j identical paths. For polarization-dependent single scattering we use the coordination number from Eq. 2.8.

$$(2.8)\quad N_j^* = 3\sum_{i=1}^{N_j} \cos^2(\alpha_i)$$

In order to fit the data, S_0^2 was fixed at the value found for the bulk elements (between 0.8 and 0.85 for the transition metals studied here). The k-space range was shifted by the ΔE_0 of the bulk elements using Eq. 2.11:

$$(2.11)\qquad k_j = \left[k^2 - \frac{\Delta E_j}{\gamma}\right]^{1/2} \qquad \text{where } \gamma \equiv \frac{h^2}{8\pi^2 m_e} = 3.8095$$

where k is in $Å^{-1}$ and ΔE is in eV.

The ΔE_0 (necessary to adjust the theoretical potential to that of the data) were fixed to be equal for all shells having the same scatterers [5] and were found by either fitting the first peak of the FT of the corresponding bulk element, or by fitting the unknown data while allowing all parameters of the first two shells to vary. In a first

instance, all parameters were varied in order to find their minima in parameter space. For sets of two highly correlated variables (eg. R and ΔE) a subset of mutual minima were found by fixing one variable at its minimum and varying the other, then repeating the procedure after reversing the variables. This gives an area in parameter space over which both variables are minimized. The model $\chi(k)$ was then moved to the minima by setting each variable to its absolute minimum. The range of fitting was limited to a region in parameter space which doubles the χ^2. The model was then least-squares fit to the data using EXAFIT. The error bars for each parameter were found by observing the range of the variable which doubles the χ^2.

The asymmetry due to anharmonicity was investigated by curve fitting the polycrystalline materials, and found to be close to the theoretical values for the bulk [6]. The C_3 value for each shell was therefore set equal to its bulk value and remained fixed during the fitting. Only four parameters were allowed to vary during the fitting: R_1, R_2 and their corresponding mean-squared relative displacements σ_1^2 and σ_2^2.

The curve fitting results have been divided into two main sections, 5.3 and 5.4. In the first, the first peaks of the FT of the various edges of the samples (shown in Fig. 5.7, 5.8, 5.9, 5.10 and 5.17) were fit. In the second, the fitting of various shells is discussed. The fits outlined in Table 5.1 were performed for each sample.

Table 5.1. Edges fit for each sample. The integers refer to the number of layers of the element being probed, and the P to the perpendicular polarization of the electric field, all other edges having $\vec{E}$ parallel to the surface of the sample. The details of the samples are given in Chapter III, Figure 1. Here 6ML Cr refers to the 8.7 Fe/3 Cu/6 Cr/3 Cu/5 Fe sample, 3ML Cr to the 8.7 Fe/3 Cu/ 3 Cr/3 Cu/5 Fe sample, 5ML Fe to the 5ML Fe/ 10ML Au sample, and 10ML Cr to the 10ML/ 10ML Au sample

6ML Cr	3 ML Cr	5 ML Fe	10 ML Cr
3 Cu	3 Cr	5 Fe	10 Cr
6 Cr	3 Cu		
5 Fe	3 Cu P		

For ultrathin films, or small particles, the coordination numbers are less than those found in the bulk. The effective coordination numbers for thin BCC films from 3 to 10ML thick have been calculated for a square domain of 400Å^2, which represents a terrace of roughly the size found in the MBE films studied here [7]. The electric vector is considered to be parallel to the <110> direction of the layers. The results of the calculations are given in Table 5.2.

Table 5.2. Calculated values of the coordination numbers N_1^* and N_2^* for films 3-10 ML thick and 400Å^2 in surface, with $\vec{E}$ parallel to the <110> of the samples.

ML	N_1^*	N_2^*
3	5.28	5.94
4	5.94	5.94
5	6.33	5.94
6	6.60	5.94
7	6.78	5.94
8	6.93	5.94
9	7.04	5.94
10	7.12	5.94
BULK	8	6

For the ultrathin films of Cu in the MBE samples it was found by simulations using (FEFF6.10) that the adjoining layers of Cr account for ~5% of the value of N_1^* and N_2^* in the first neighbours peak of the FT. Interdiffusion was not considered, and the adjoining layers were assumed to have the same crystal structure of the lattice parameters as the film containing the Cu. The adjoining layers of Fe, however, do not contribute to the Cu N_j^*.

5.3.1. Fitting of the first peak of the FT

5.3.1.a. 8.7 Fe/3 Cu/6 Cr/3 Cu/5 Fe Sample

All three films examined (Fe, Cr, Cu) were found to have a tetragonal distortion. The $k\chi(k)$ were all transformed using a 10% Hanning window (Eq. 2.14.b) and the curve fitting was applied to both the real and imaginary parts of the FT in R-space. Allowing N_2^*/N_1^* to vary in the range from 0.75 to 1.0 gave essentially the same R_i values.

The *a* lattice constants were calculated from R_2 since for polarizations with $\vec{E}$ parallel to the sample's surface $R_2=a$, and we assume that $a=b$, see Fig. 5.1. The *c* lattice constants were calculated from R_1 and R_2 using the relation:

(5.3) $c=[4R_1^2-2R_2^2]^{1/2}$

$$\Delta c \simeq \frac{4R_1\Delta R_1}{c}\sqrt{1+\frac{1}{4}\left(\frac{R_2}{R_1}\right)^2}$$

The fit parameters obtained from the fitting of the 5ML of Fe in the 8.7 Fe/3 Cu/6 Cr/3 Cu/5 Fe sample are given in Table 5.3, and the result of the fit is shown in Fig. 5.20.

Calculations of the electric field intensity show that it is 50% lower in the lower layers of Fe at the Fe edge than in the upper layers, therefore the Fe sampled is the film just below the Au.

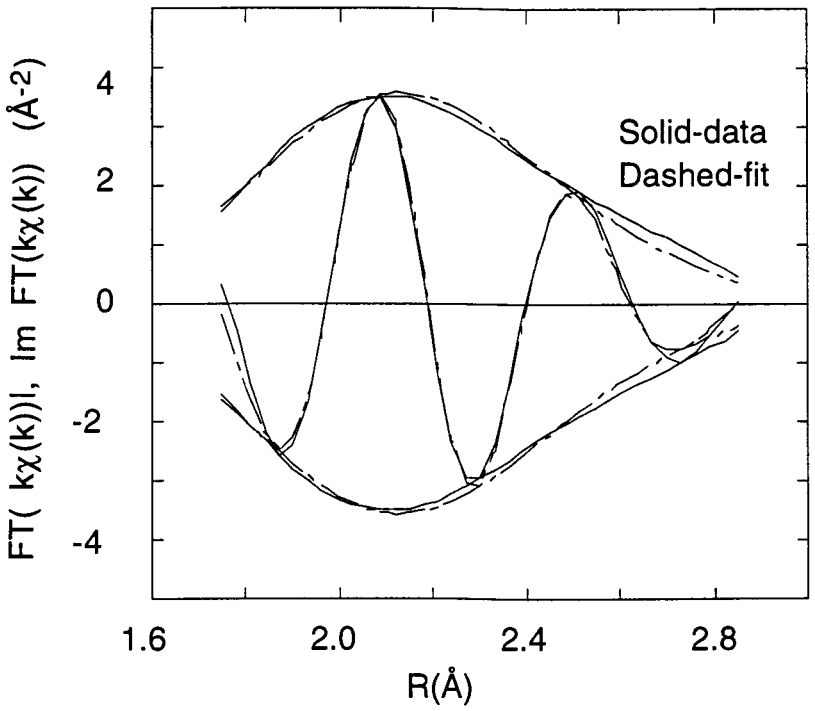

Figure 5.20. Fit of Fe edge of 5ML of Fe in 8.7 Fe/3 Cu/6 Cr/3 Cu/ 5 Fe sample. The Magnitude of the FT is the envelope, and the Imaginary part is the oscillatory part. $\chi^2(4V)=0.4\times10^{-3}$, calculated from Eq. 2.18.

Using Eq. 5.3 and the values in Table 5.3 gives c=2.86±0.03Å and thus c/a=1.010±0.012. Therefore, in the Fe above the Cu, c assumes the bulk value (2.86±0.01Å) but a is shortened by 0.036Å (or 1.3%).

Table 5.3. Fit parameters of Fe in the 8.7 Fe/3 Cu/6 Cr/3 Cu/ 5 Fe sample. The k-space range was 2.13 to 14.04Å^{-1}, and the R-space range was 1.76 to 2.86Å. S_0^2 was 0.80.

	5ML Fe	BCC Fe
R_1(Å) (±0.01Å)	2.46	2.4824
R_2(Å) (±0.01Å)	2.83	2.8665
σ_1^2 (x10^{-3}) (±0.3)	5.0	5.05
σ_2^2 (x10^{-3}) (±0.3)	8.0	6.6
N_1^* (±0.5)	6.0	8.0
N_2^* (±0.5)	5.4	6.0

The results of fitting Fe thus lead to a BCT structure. The analysis shows that there is effectively a higher σ_i^2 in the second shell (see analysis for Fig. 5.7), which corresponds to more disorder in the plane of the surface of the film than there is in the bulk material BCC Fe. The coordination numbers N_1^* and N_2^* listed in Table 5.3 are lower than those found in the bulk. They are, however, within 10% of those calculated for a film 5ML thick where N_1^*=6.3 and N_2^*=5.9 are expected [7], as is shown in Table 5.2.

The results of the fit of the Cu edge in the 8.7 Fe/3 Cu/6 Cr/ 3 Cu/5 Fe sample are given in Table 5.4. The fitting of the Cu edge shows Cu to have R_2=a=b=2.84±0.01Å and, using Eq. 5.3, c=2.91±0.03Å with c/a=1.024±0.012, as opposed to 3.61Å in the FCC structure, or 2.8839Å if it were to assume a perfectly lattice matched BCC

structure on bulk BCC Cr. The results of the fit are compared to those of a "BCC" Cu structure lattice matched to Cr. The resulting fit is shown in Fig. 5.21.

Table 5.4. Fit parameters of Cu in the 8.7 Fe/3 Cu/6 Cr/3 Cu/5 Fe sample. The k-space range was 2.2 to 15.04Å^{-1}, and the R-space range was 1.73 to 2.58Å. S_0^2 was 0.83. The parameters of an ideal BCC Cu grown on Cr are given as a comparison.

	3ML Cu	BCC Cu/BCC Cr
R_1(Å) (±0.01Å)	2.48	2.4975
R_2(Å) (±0.01Å)	2.84	2.8839
σ_1^2 (x10^{-3}) (±0.3)	8.0	7.2
σ_2^2 (x10^{-3}) (±0.3)	17.0	8.2
N_1^* (±0.7)	7.0	8.0
N_2^* (±0.7)	6.5	6.0

The fitting results show Cu has grown in a BCT structure with c/a=1.024±0.012, where the first two shells are separated by 0.36Å. Once again there is more disorder in the direction parallel to the surface of the film.

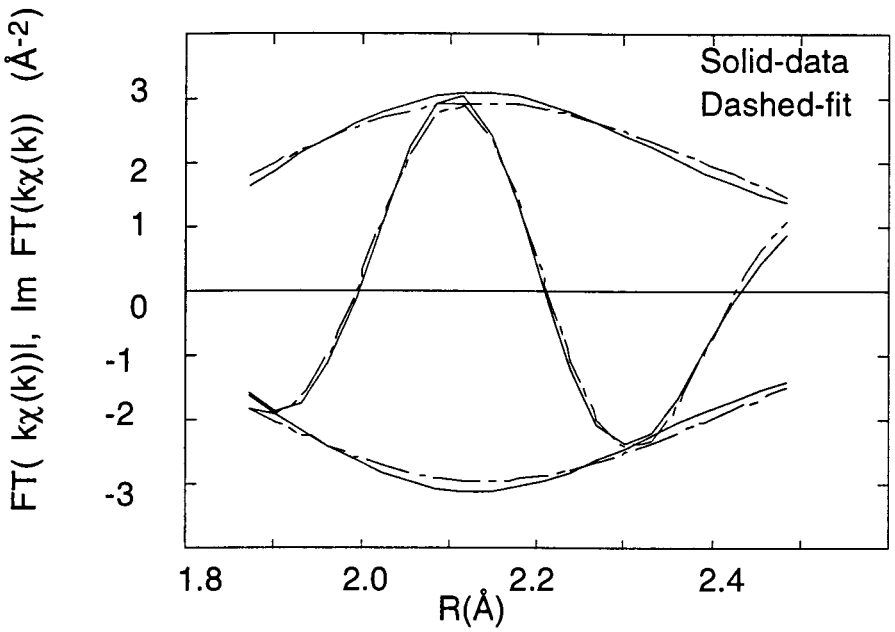

Figure 5.21. Fit of Cu edge of 3ML of Cu in the 8.7 Fe/3 Cu/6 Cr/ 3 Cu/5 Fe sample. The Magnitude of the FT is the envelope, the Imaginary part is the oscillatory part. $\chi^2(4V)=0.78\times10^{-4}$, calculated from Eq. 2.18.

The coordination numbers expected for 3ML Cu are $N_1^*=5.2$ and $N_2^*=5.94$ [7]: those obtained from fitting are much higher and lead to the assumption that more than just Cu contributes while measuring the Cu edge. The coordination numbers are more consistent with those of a 5ML thick film, and since there is Cr below the Cu, and Fe above it, it is possible that they contribute to the coordination numbers. Modelling of the sample with FEFF6.10 shows that 5% of the Cu N_j^* for j=1,2 can be attributed to the adjacent Cr layers. The overlayers of Fe are rejected on the basis of simulations having two overlayers of Fe on the Cu. The XAFS of the Cu is insensitive to their

presence. The ratio of $N_2^*/N_1^*=1.07$ is higher than the 0.90 calculated for thin films in the 5-10ML range.

Here the surface of the underlying Cr films has acted as a template for the growth of Cu. The deposited Cu layer has been forced to contract in the plane of the interface to lattice match the Cr. The Cu film therefore has a lattice constant *c* which is expanded with respect to the Cr film in order to keep the atomic volume of Cu equal to its bulk value: to a zeroth order the film accommodates the strain elastically. For the Cu the tetragonal distortion due to the Cr is such that it grows in a BCT structure, as opposed to its bulk FCC one. Nonetheless, the atomic volume of the Cu (number of atoms in the unit cell / volume of the unit cell) remains almost constant, decreasing by only 0.3%.

In order to fit the first neighbour peak of BCC Cr (Appendix A) it proved necessary to include the triangular multiple scattering paths. The triangular paths were also included while fitting the Cr edge of the 6ML of Cr in the 8.7 Fe/3 Cu/6 Cr/3 Cu/5 Fe sample, but will not be included in the table of results. The Cr edge fit led to the parameters shown in Table 5.5, where the bulk BCC Cr values are given for comparison, and the fit result is shown in Fig. 5.22. The *c* value for Cr was calculated from Eq. 5.3 to be c=2.92 (±0.03Å), where $R_2=a=b$=2.86±0.01Å and the ratio of c/a=1.020±0.012. Once again the structure is seen to be BCT. The first two shells are separated by 0.36Å, which is significantly smaller than the ΔR=0.386Å for bulk BCC Cr. The coordination numbers are within 10% of those calculated for a 6ML thick film, as is seen in Table 5.2. The tetragonal

distortion is particularly evident as the bump at 2.6Å on the high-R side of the first peak of the FT of Cr (Figure 5.8, Fig. 5.22). This bump has as its source the polarization-dependence of the single and multiple scattering paths.

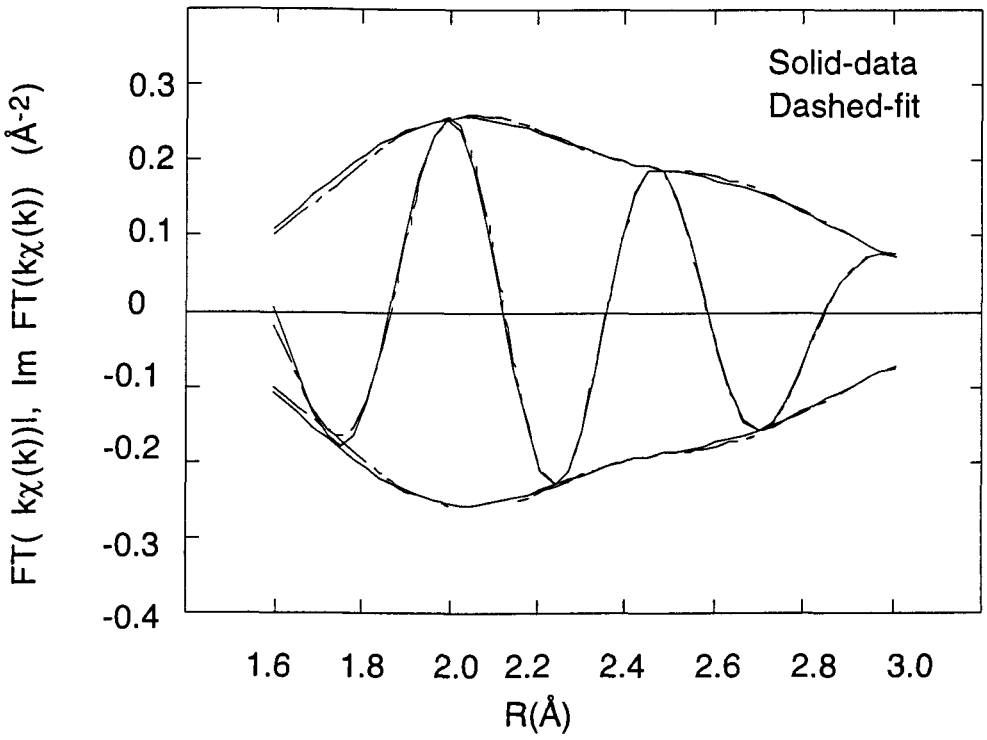

Figure 5.22. Fit of Cr edge of 6ML of Cr in the 8.7 Fe/3 Cu/6 Cr/3 Cu/5 Fe sample. The Magnitude of the FT is the envelope, and the Imaginary part is the oscillatory part. $\chi^2(5V)=0.8\times10^{-4}$, calculated from Eq. 2.18.

In summary, the layers of Cr, Cu and Fe of the 8.7 Fe/3 Cu/ 6 Cr/3 Cu/5 Fe sample are found to be contracted in the plane of the surface ($a_{FILM}<a_{BULK}$) and of BCT structure with $c/a>1.00$. The lattice parameters of the layers are given in Table 5.6. The

tetragonal distortion is seen to diminish (within error): as subsequent multilayers are grown on the Cr it decreases from 1.020 to 1.010.

Table 5.5. Fit parameters of Cr in 8.7 Fe/3 Cu/6 Cr/3 Cu/5 Fe sample. The fitting included the triangular multiple scattering paths. The k-space range was 1.544 to 10.15Å^{-1}, and the R-space range was 1.61 to 3.0Å. S_0^2 was 0.80. The parameters of an ideal BCC Cr are given as a comparison.

	6ML Cr	BCC Cr
R_1(Å) (±0.01Å)	2.50	2.4975
R_2(Å) (±0.01Å)	2.86	2.8839
σ_1^2 (x10^{-3}) (±0.3)	5.6	5.05
σ_2^2 (x10^{-3}) (±0.3)	6.5	6.6
N_1^* (±0.5)	6.1	8.0
N_2^* (±0.5)	5.7	6.0

Table 5.6. Lattice parameters of the layers of the 8.7 Fe/3 Cu/ 6 Cr/3 Cu/5 Fe sample.

	a(Å)±0.01Å	*c*(Å)±0.03Å	*c/a* ±0.012
Fe	2.83	2.86	1.010
Cu	2.84	2.91	1.024
Cr	2.86	2.92	1.020

5.3.1.b 8.7 Fe/3 Cu/3 Cr/3 Cu/5 Fe sample

The first nearest neighbours peaks of the FT shown in Figure 5.10 (Cu3, Cu3P) were fit in R-space using EXAFIT. The results for the fitting of the Cu edge in the 8.7 Fe/3 Cu/3 Cr/3 Cu/5 Fe sample are given in Table 5.7.

Table 5.7. Fit parameters of Cu in the 8.7 Fe/3 Cu/3 Cr/3 Cu/5 Fe sample. The k-space range was 1.35 to 14.00Å^{-1}, and the R-space range was 1.79 to 2.50Å. S_0^2 was 0.83. The N_i^* expected for 3ML with $\vec{E}$ perpendicular are 5.28 and 5.94 for the first and second shell respectively, as for the parallel case.

	Cu 3 with $\vec{E}$ Perpendicular	Cu 3 with $\vec{E}$ Parallel
R_1(Å) (±0.006Å)	2.466	2.471
R_2(Å) (±0.008Å)	2.894	2.829
σ_1^2 (x10^{-3}) (±0.7)	5.5	5.4
σ_2^2 (x10^{-3}) (±2.0)	16.0	18.0
N_1^* (±0.5)	7.1	6.2
N_2^* (±0.5)	6.4	5.6

The values given above for the parallel case result in a value of $R_2=a=2.829\pm0.01$Å and $R_1=2.471\pm0.01$Å, which gives $c=2.902\pm0.03$Å (which is within 0.008Å of the R_2, or c, value found with $\vec{E}$ perpendicular to the film). The structure is tetragonally distorted

for c and a found from $\vec{E}$ perpendicular are c=2.894, a=2.824Å, which gives c/a=1.0247±0.017. The ratio of c/a found from the value of *a* measured for $\vec{E}$ parallel, and from c with $\vec{E}$ perpendicular is 1.023±0.017, which is very close to those found with the $\vec{E}$ either in one orientation or the other. The results of the fitting are shown in Fig. 5.23 for Cu taken with $\vec{E}$ parallel, and Fig. 5.24 for $\vec{E}$ perpendicular to the substrate.

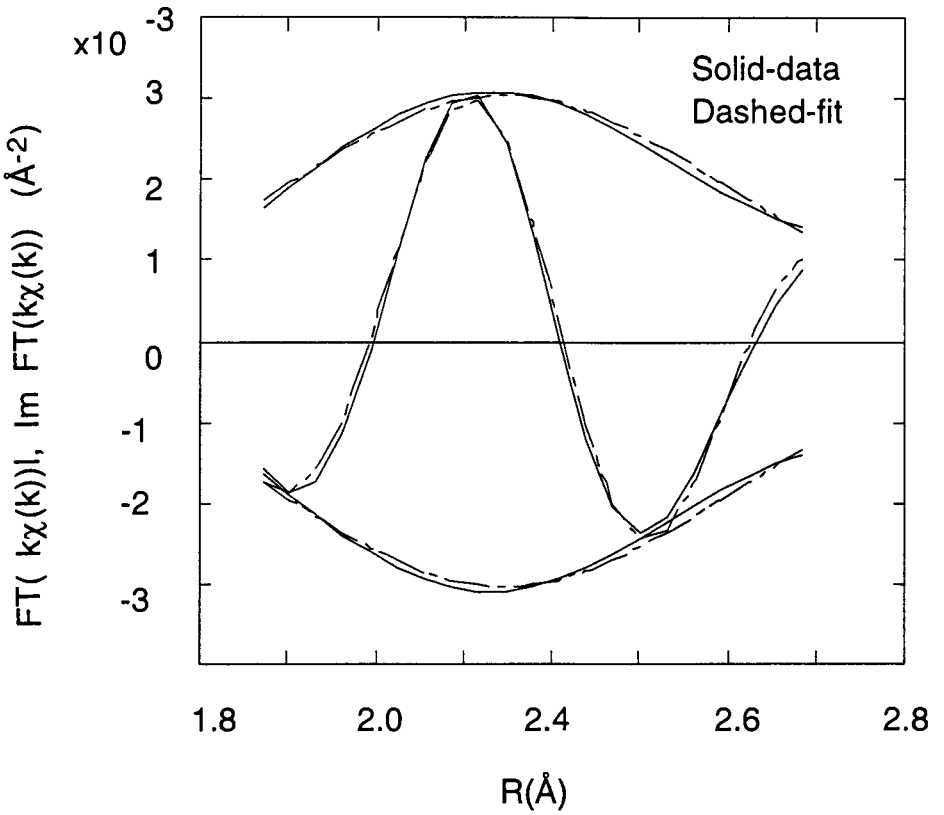

Figure 5.23. Fit of Cu edge of 3ML of Cu in 8.7 Fe/3 Cu/3 Cr/3 Cu/ 5 Fe sample with the $\vec{E}$ of the x-rays parallel to the substrate. The Magnitude of the FT is the envelope, and the Imaginary part is the oscillatory part. $\chi^2(4V)=0.2x10^{-3}$, calculated from Eq. 2.18.

The first peak of the FT of the Cr edge in the 8.7 Fe/3 Cu/ 3 Cr/3 Cu/5 Fe sample was fit. The results are listed in Table 5.8 where c=2.797±0.03Å, and c/a=0.985±0.012. The values of the coordination numbers are 45% and 15% larger than those calculated for a 3ML thick film (N_1^*=5.28, N_2^*=5.94), as was the case for the 3ML of Cu in the 8.7 Fe/3 Cu/6 Cr/3 Cu/5 Fe sample (5.2.1.a). This increase is attributed to scatterers in the Cu layers adjacent to the Cr.

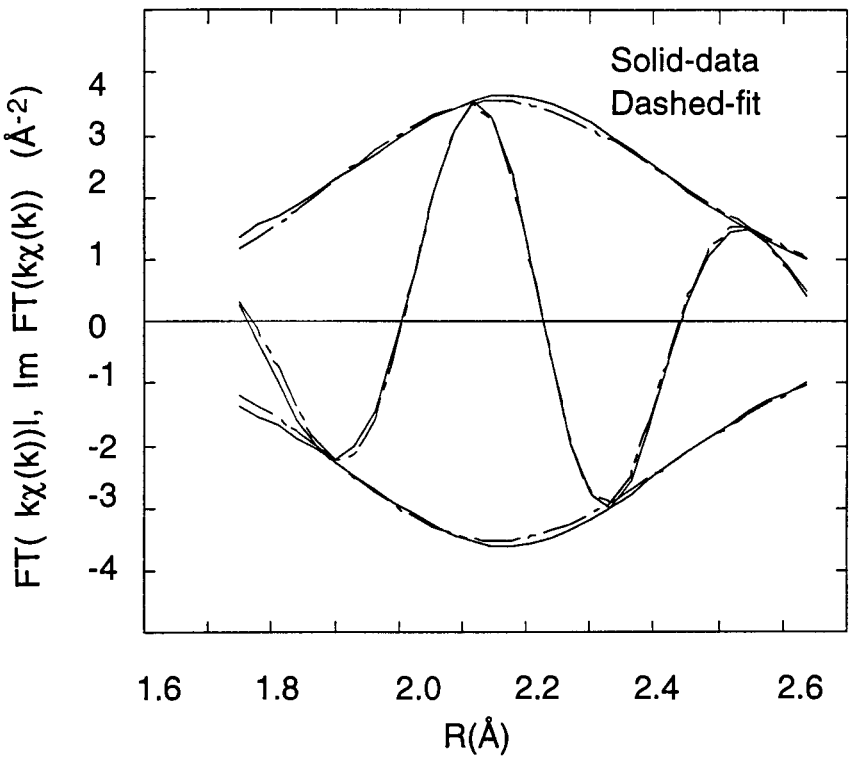

Figure 5.24. Fit of Cu edge of 3ML of Cu in 8.7 Fe/3 Cu/3 Cr/3 Cu/ 5 Fe sample with the $\vec{E}$ of the x-rays perpendicular to the substrate. The Magnitude of the FT is the envelope, and the Imaginary part is the oscillatory part. $\chi^2(4V)=0.7\times10^{-4}$, using Eq. 2.18.

Table 5.8. Fit parameters of Cr in the 8.7 Fe/3 Cu/3 Cr/3 Cu/5 Fe sample. The k-space range was 1.65 to 10.12Å^{-1}, and the R-space range was 1.73 to 2.79Å. S_o^2 was 0.80.

	3ML Cr	BCC Cr
R_1(Å) (±0.01Å)	2.47	2.4975
R_2(Å) (±0.01Å)	2.84	2.8839
σ_1^2 (x10^{-3}) (±0.3)	8.80	5.05
σ_2^2 (x10^{-3}) (±0.3)	10.3	6.60
N_1^* (±0.5)	7.0	8.0
N_2^* (±0.5)	6.3	6.0

5.3.1.c. 5ML Fe/10ML Au sample

Fitting the Fe edge of 5ML of Fe grown at RT on Ag(001) led to the parameters in Table 5.9, where the bulk BCC Fe values are given as a comparison. Here $R_2=a=b=2.869\pm0.02$Å, and the c value of Fe was calculated from Eq. 5.3 to be $c=2.905\pm0.03$Å which gives a BCT structure of $c/a=1.012\pm0.012$, with the first two shells separated by 0.37±0.01Å. The fit is shown in Fig. 5.25.

The values of the coordination numbers are within 10% (Table 5.2) of those expected for a film 5ML thick. The distortion of the 5ML Fe is larger than an elastic accommodation of the film to the lateral strains induced by the epitaxy on the Ag(001) single crystal substrate.

Table 5.9. Fit parameters of Fe in the 5ML Fe/10ML Au sample. The k-space range was 1.61 to 14.75Å^{-1}, and the R-space range was 1.68 to 2.76Å. S_o^2 was 0.80.

	5ML Fe	BCC Fe
R_1(Å) (±0.01Å)	2.495	2.4824
R_2(Å) (±0.01Å)	2.869	2.8665
σ_1^2 (x10^{-3}) (±0.3)	6.77	5.05
σ_2^2 (x10^{-3}) (±0.3)	9.08	6.60
N_1^* (±0.7)	6.9	8.0
N_2^* (±0.7)	6.2	6.0

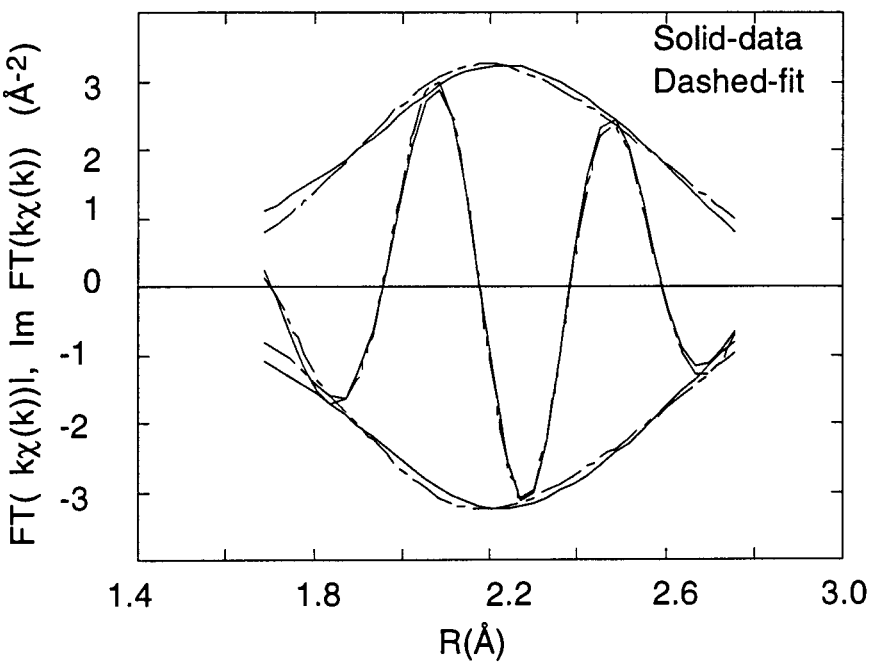

Figure 5.25. Fit of Fe edge of 5ML of Fe grown at RT on Ag(001). The Magnitude of the FT is the envelope, and the Imaginary part is the oscillatory part. $\chi^2(4V)=0.1x10^{-3}$, calculated from Eq. 2.18.

5.3.1.d. 10ML Cr/10ML Au Sample

The results of fitting the Cr edge of the 10ML Cr grown at RT on Ag(001) are given in Table 5.10 alongside the bulk BCC Cr values, and the fit is shown in Fig. 5.26. The *c* value of the Cr was evaluated from $R_2=a=b=2.895\pm0.02$Å and $R_1=2.527$Å, with Eq. 5.3, to be $c=2.96\pm0.03$Å giving a BCT structure with $c/a=1.022\pm0.012$. The $\Delta R=0.368\pm0.01$Å is smaller than that of bulk BCC Cr (0.386Å). The coordination number is, for the first shell, smaller than that calculated for a film 10ML thick (7.12 atoms), and for the second shell the measured and calculated (5.94 atoms) values are within 5% of each other, which is well within the error bars for this value. The value of N_1^* may be smaller than expected due to clustering of the Cr, as was seen in the literature [3.7].

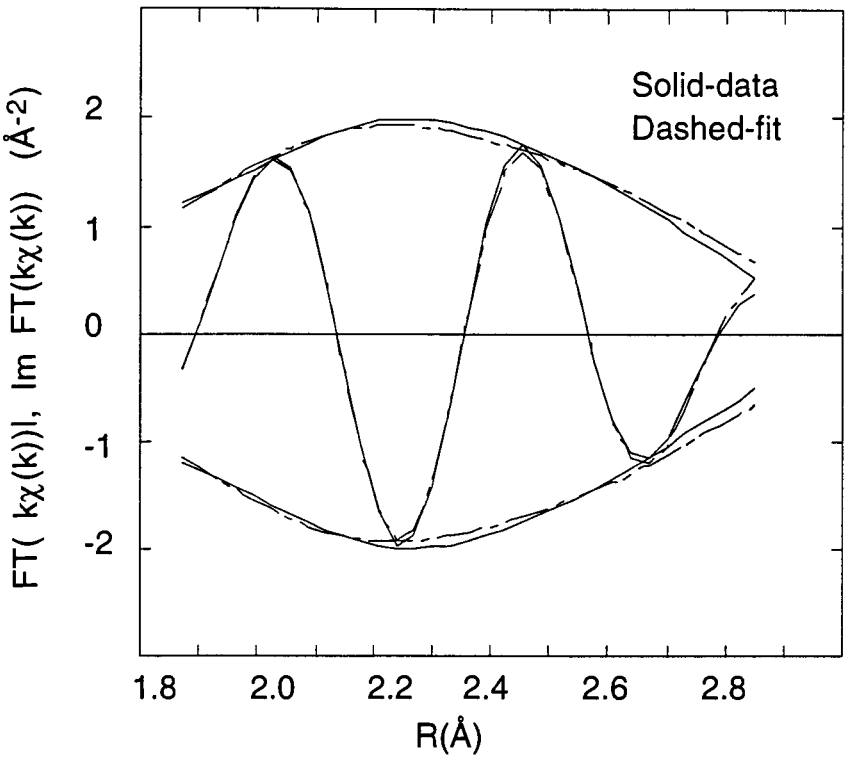

Figure 5.26. Fit of Cr edge of 10ML of Cr grown at RT on Ag(001). The Magnitude of the FT is the envelope, and the Imaginary part is the oscillatory part.

Elasticity theory fails to account for the expansion of the *c* axis of the Cr. Using the equations of elasticity theory from Chapter VII (Eq. 7.1) and Chapter I (Eq. 1.2), the misfit strain induced by the Ag(001) substrate will lead to a change in the c lattice parameter with respect to the substrate that is -0.14±0.05% (C_{12}/C_{11}=0.19 for Cr, $\Delta c/c=(c_{measured}-c_{bulk})/c_{bulk}$, and $\Delta a/a$ is the lattice mismatch). However, the measured value is +2.63±0.06%. One possible explanation for this is that the surface energy criterion for wetting is not met for Cr on Ag as was explained in Chapter III Section 1.3.d. Whereas the references quoted in Chapter III state that above 7ML Cr

grows in a BCC structure on Ag(001) at RT, it is noted here that even after 10ML of growth the structure is still slightly tetragonally distorted. The sample of 4ML of Cr on Ag(001) showed strong evidence of intermixing of Cr and Ag (note the low-R feature in the FT in Figure 5.17) and was not fit using the least squares technique. The results from the fitting of the 10ML Cr sample are given in Table 5.10 and correspond to those obtained from fitting the first peak at about 2.4Å to a polarization-independent model which included the triangular MS paths. Simulations show that the bump on the high R-side of the FT of 10ML of Cr, shown in Fig. 5.17, is associated with the polarization dependence of the triangular MS paths of the BCT structure, however, this fitting refinement was not pursued at this point.

Table 5.10. Fit parameters of Cr in the 10ML Cr/10ML Au sample. The k-space range was 2.10 to 13.13Å^{-1}, and the R-space range was 1.86 to 2.34Å. S_0^2 was 0.80.

	10ML Cr	BCC Cr
R_1(Å) (±0.01Å)	2.527	2.4975
R_2(Å) (±0.01Å)	2.895	2.8839
σ_1^2 (x10^{-3}) (±0.3)	10.0	5.05
σ_2^2 (x10^{-3}) (±0.3)	11.3	6.60
N_1^* (±0.7)	6.25	8.0
N_2^* (±0.7)	5.65	6.0

5.4. Modelling

5.4.1. Modelling of 6Cr/3Cu/5Fe

Though Cu and Cr are five elements apart in the periodic table, the differences in their amplitudes and phase shifts were not large enough to address easily the question of their possible interdiffusion. It was necessary to use the differences in their theoretical backscattering amplitudes and phases at low-k, as well as to model the films in order to distinguish one from the other. The model consisted of the first two shells around a Cu absorber in a system of Fe/3ML Cu/Cr. The Cu absorber was placed in the centre of each layer of Cu successively and the total $\chi(k)$ was calculated from the average of the three individual $\chi(k)$ (one from each layer of Cu). The number of neighbours are given in Table 5.11. The polarization of the $\vec{E}$ was along <110>. This direction was determined previously (in the introduction to chapter V) from the orientation of the Fe lattice with respect to the underlying crystal Ag(001) substrate. In this way it was found that neither Cr nor Fe was detected in the Cu, in the first peak of the FT (ie for R_1 and R_2) of the Fe/Cu/Cr/Cu/Fe multilayers, as is evident in Fig. 5.27.

The fact that the *c* and *a* lattice parameters obtained from the fitting of the Cu 3ML sample with $\vec{E}$ parallel, and also with perpendicular, are the same provides a consistency check of the analysis procedure. It also confirms that the model used for the

the first and second shell fit was valid: the underlayers and overlayers do not diffuse into the Cu layer inasmuch as the effective coordinations of Cu-Fe and Cu-Cr are too small to be detected in the presence of the Cu-Cu coordinations. To detect Cu-Fe and Cu-Cr coordination it is necessary to extend the analysis to higher shells. Further simulations showed that the excess intensity of higher Cr peaks in the multilayers (~4.5Å) could be directly attributed to the Cu overlayers, as is seen in greater detail in Section 5.4.2.

Table 5.11. N_i^* for the first two shells of Cr/3ML Cu/Fe. The absorber is in the center of each Cu layer, the $\vec{E}$=<110>, and $N_i^*=3(\vec{\varepsilon}\circ\vec{r}_1)$.

		N_{Cu-Cu}	N_{Cu-Fe}	N_{Cu-Cr}
Top	R_1	3	3	0
	R_2	6	0	0
Middle	R_1	6	0	0
	R_2	6	0	0
Bottom	R_1	3	0	3
	R_2	6	0	0

In the above perfect crystal model the percentage of the first coordination shell due to Cu-Cr, or Cu-Fe scattering is 6.6%, and that of the second coordination shell due to the over (under) layers is 0%. Were we to assume a random orientation of microcrystallites, the total Cu-Fe and Cu-Cr contribution to the first shell's coordination would be 6.0%, and similarily, that of Cu-Fe and Cu-Cr to the second shell's coordination would be 4.0%.

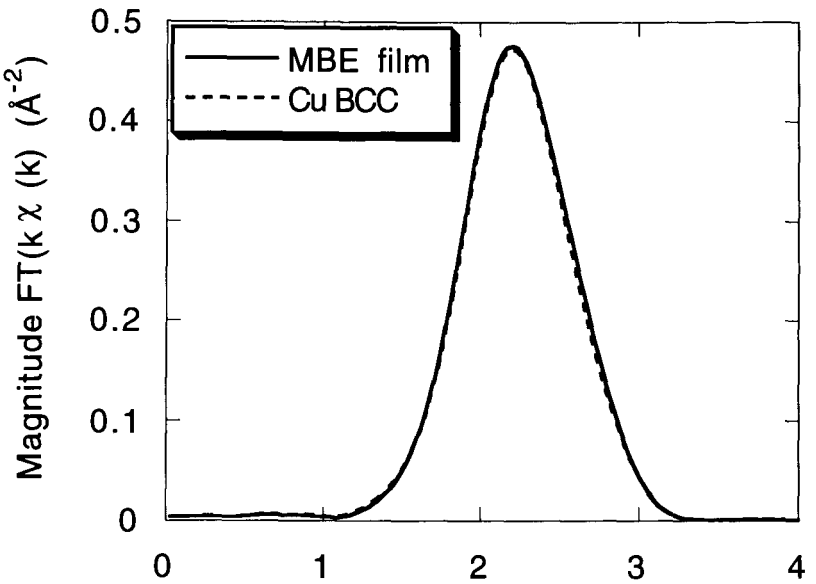

Figure 5.27. Magnitude of the FT(kχ(k)) for the first two shells of pure Cu and 6Cr/3Cu/5Fe.

5.4.2. Modelling of higher shells

Simulations of 6ML of BCT Cr sandwiched in between two 3ML layers of BCT Cu, out to radii of 6Å, confirm the BCT structure of the Cr by reproducing the bump on the high-R side of the FT of the 6ML Cr (in the 8.7 Fe/3 Cu/6 Cr/3 Cu/5 Fe sample). The simulations involved inputting the radii, and the mean square relative displacements obtained from a polarization-independent fitting (of the first nearest neighbours peak of the FT) in FEFF6.10. The results were optimized using a fully polarization-dependent simulation of the shells out to 6Å The structure simulated with FEFF6.10 is shown in Fig. 5.28. The x-ray interference function $\chi(k)_i$ was

calculated for the x-ray absorbing atom centered in the ith layer. The average $\chi(k)$ was obtained by summing over all layers. The Debye temperature of the combined layers was found by using the reduced mass formula, which, for $\Theta_D(Cu)=415K$, and $\Theta_D(Cr)=485$, gives $\Theta_D=461K$. The Debye temperature was considered to be that of Cr for the two middle layers of Cr, and the reduced value for the upper (lower) two layers. Changing the Debye temperature in this manner allows for a better simulation of the Cr layers by allowing for a different degree of static disorder in each layer. The FT of this average is shown in Fig. 5.29. The peak at 4.5Å in the FT of Cr in Fig. 5.29 is enhanced by the presence of the adjacent Cu and is not consistent with the formation of a Cu-Cr alloy, as is shown in Fig. 5.30.

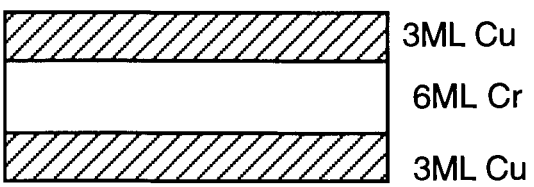

Figure 5.28. The simulated BCT Cu/Cr/Cu structure. The lattice parameters for the Cu are those given in Table 5.4, those of the Cr in Table 5.5.

Alloying was simulated by replacing Cr atoms with Cu atoms in each shell of the model. Linear combinations of bulk FCC Cu and BCC Cr showed that the 6ML of Cr (in the 8.7 Fe/3 Cu/6 Cr/3 Cu/ 5 Fe sample) contained less than 20% Cu in the 4th and 5th shells. In the closest fitting model, the number of substitutions was kept to

roughly 10% of the total number of atoms expected in each BCC shell. In other words there would be one atom of Cu in the first nearest neighbour shell of the Cr (represents 12.5% Cu in the Cr shell). However, as is seen in Fig. 5.30, the model shows a sharp peak at about 2.6Å, and much more intensity in the higher shells than the 6ML Cr data.

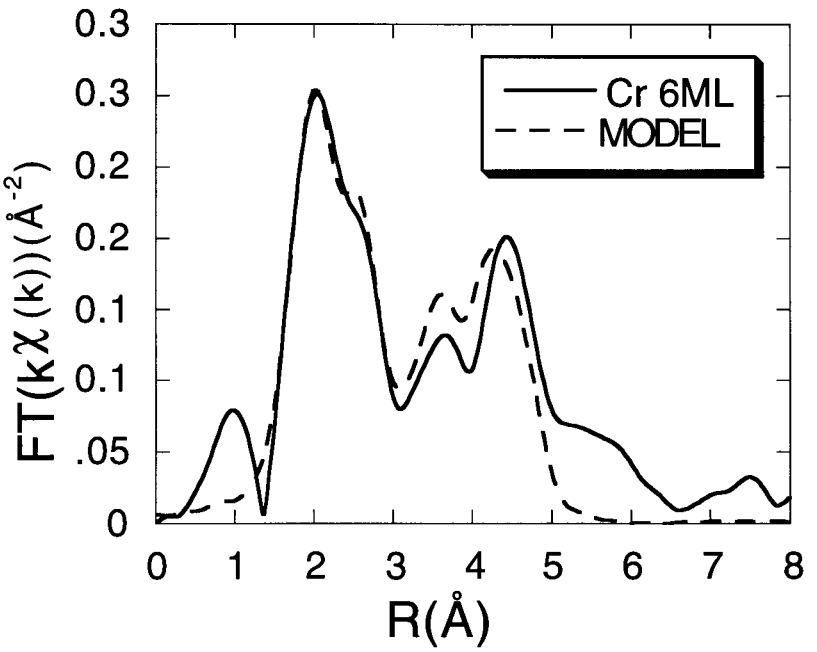

Figure 5.29. Full polarization-dependent model of 6ML Cr grown between two three layer-thick films of Cu. The parameters obtained from the fitting of the first peak of the FT were used in order to simulate the film out to 5Å. A 10% Gaussian window (Eq. 2.14.b) was applied over the k-space range 1.54 to 10.15Å^{-1}.

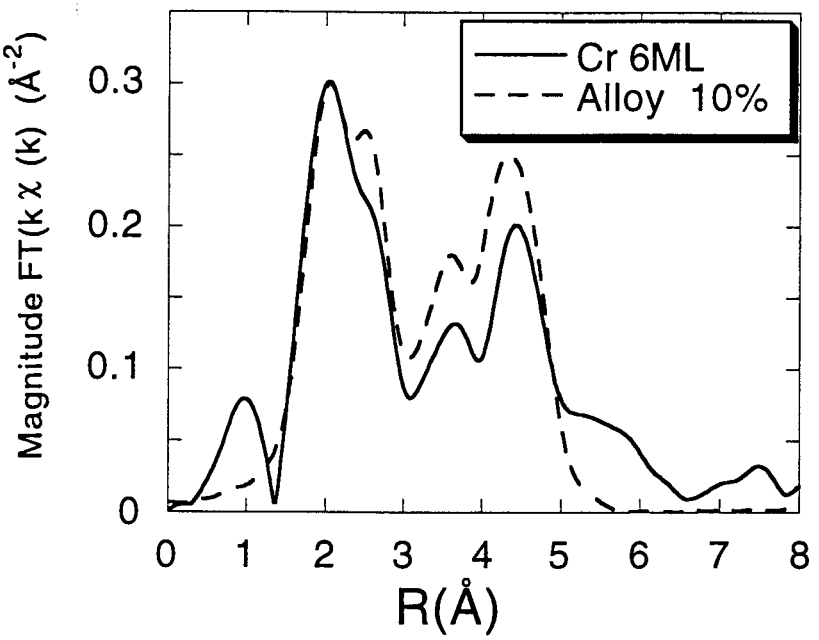

Figure 5.30. Full polarization-dependent model of 6ML of Cr grown between two three layer-thick films of Cu. A 10% Gaussian window (Eq. 2.14.b) was applied over the k-space range from 1.54 to 10.15Å^{-1}.

In order to assess the interdiffusion of the Cr in the Cu in the 8.7 Fe/3 Cu/3 Cr/3 Cu/5 Fe sample several models of $\chi(k)$ where considered. A model, which assumed a perfect epitaxial structure of 3ML Cu/3ML Cr/3ML Cu in which the bottom layer of the Cr (or the top layer since the sample is symmetric), has 4 Cu first nearest neighbours and 4 Cr first nearest neighbours, and the Cr in the middle layer has 8 first nearest neighbours which are Cr and 4 Cr and 2 Cu second nearest neighbours. The positions in the peaks of the FT were shifted to lower R than those in the film, and this perfectly epitaxial model was rejected. A second model assumed that there had been

interchanging of full layers and that the structure was 2Cu/1Cr/1Cu/1Cr/1Cu/1Cr/2Cu. This model was also rejected. Models assuming an interdiffusion of atoms along the Cu/Cr interfaces proved more realistic. Without extensive modelling it is impossible to decide how many atoms have been displaced, but it seems that roughly a quarter of the bottom Cr layer (top layer) has intermixed with the Cu.

CHAPTER VI: Data Analysis of Radio Frequency Sputtered Films

The data analysis of the RF sputtered films is divided into two sections. In the first the XAFS interference functions of the two samples are compared and discussed, as well as their Fourier transforms ($FT(k^3\chi(k))$). The beating analysis from the first peaks of the transforms will also be analysed.

The second section contains results from modelling. The samples are outlined in Chapter III, Section 2.3: Sample 1 is SiO_2/69.2ÅCo/40.2ÅRe, and Sample 2 is SiO_2/75.8ÅRe/24.4ÅCo/44.6ÅRe.

1. Comparisons of $\chi(k)$ and $FT(k^3\chi(k))$ and Beating Analysis

The K and L_{III} edge spectra, of Co and Re respectively, were taken with the polarization vector parallel and perpendicular to the surface of the sample. The background removal was performed using AUTOBK. Figures 6.1 and 6.2 show the results obtained from the Co edge with $\vec{E}$ parallel to the sample (Co1) and from a thin foil of Co taken in transmission (Co FOIL). The resulting $\chi(k)$ are shown in Figure 6.3.

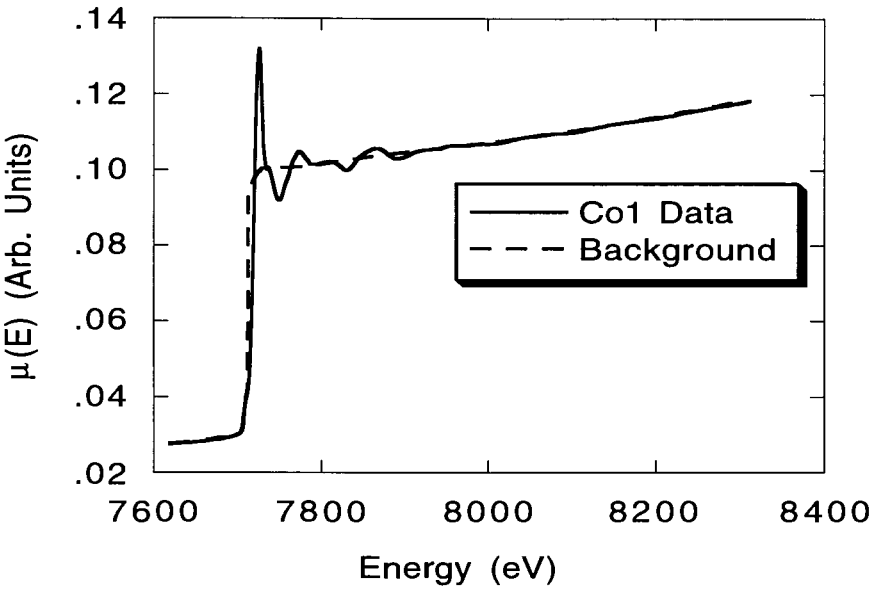

Figure 6.1 Background removal for Co1 K-edge with $\vec{E}$ parallel.

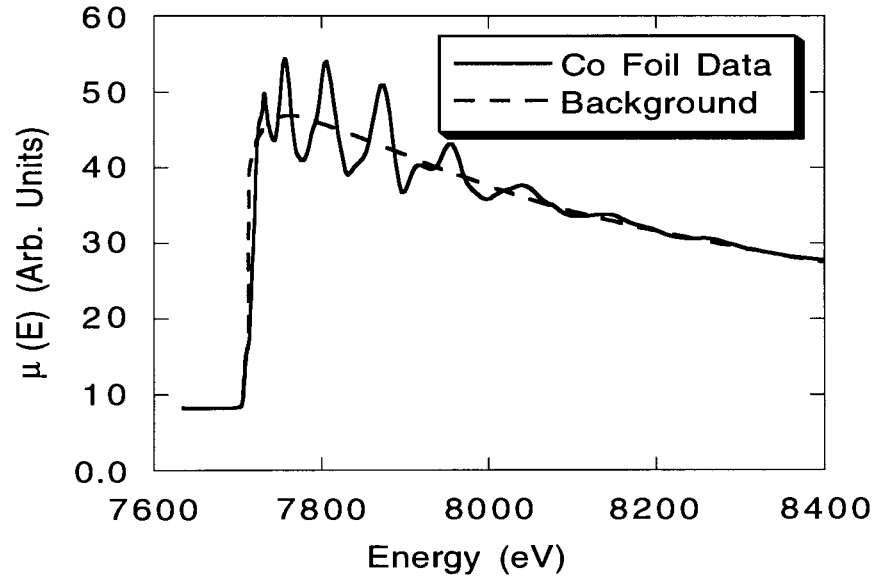

Figure 6.2. Background removal for Co K-edge in HCP Co foil taken in transmission.

The upper curve in Fig. 6.3 shows the $\chi(k)$ of HCP Co, the lower curves represent the Co edges in Sample 2 (Co2) and Sample 1 (Co1). A first evaluation of the spectra leads to the conclusion that Co1 and Co2 are not HCP, their interference function shows no resemblance to that of Co, nor is there any resemblance to the interference function obtained from FCC Cu (see Fig. 5.3). As was mentioned in Chapter V, Section 1.1, the $\chi(k)$ of a BCC structure has two distinct peaks in the region from 4 to 6 $Å^{-1}$ (see for example Fig. 5.1). There are two heavily attenuated peaks in that same range, the structures may be BCC. In Fig. 6.4 the $\chi(k)$ of the Co edge taken with $\vec{E}$ parallel are compared to those for $\vec{E}$ perpendicular, for both samples. The interference functions of the two samples resemble each other and are similar for both orientations of the electric field.

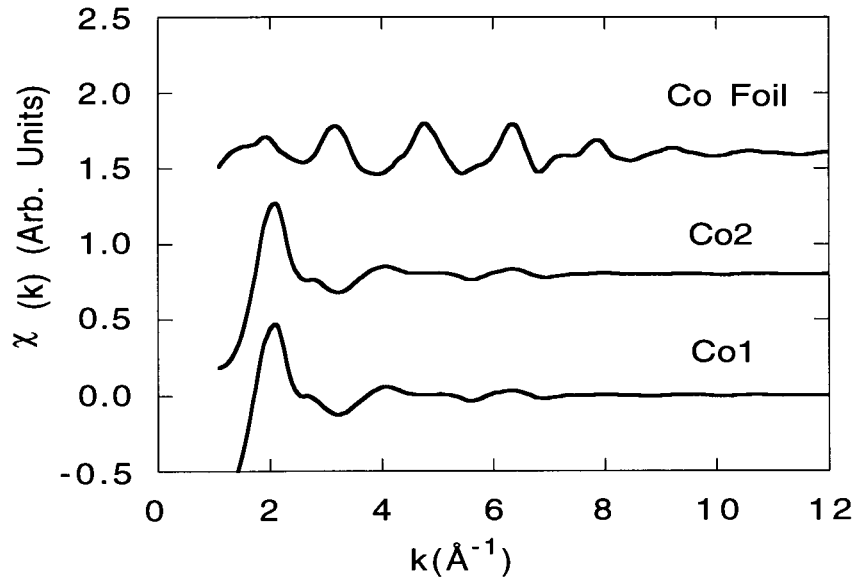

Figure 6.3. $\chi(k)$ of HCP Co, Co K-edges in samples 2 and 1, $\vec{E}$ parallel.

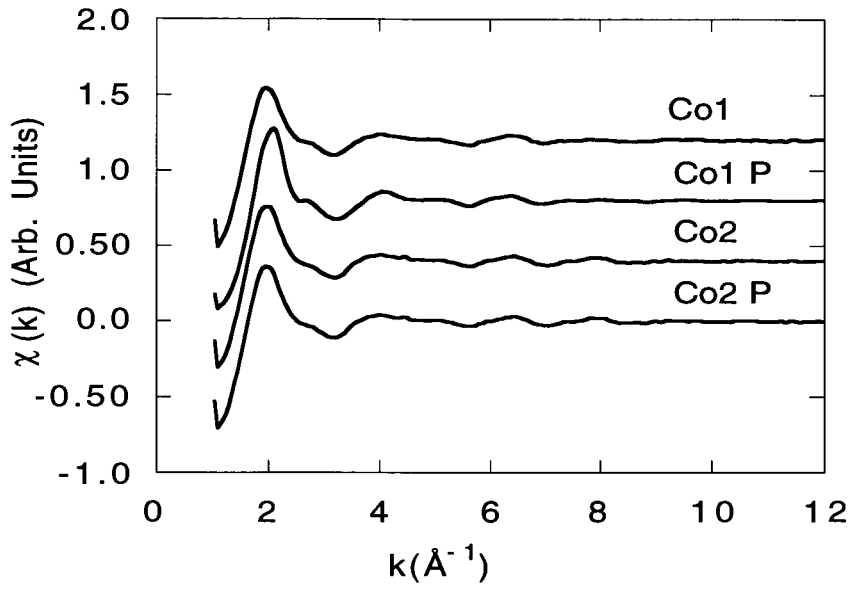

Figure 6.4. $\chi(k)$ of the Co K-edge of samples 1 and 2 with $\vec{E}$ll (Co1 and Co2) and $\vec{E}$ Perpendicular (Co1 P, Co2 P).

Figure 6.5 shows the transmission interference function of ReO_x taken at the L_{III} edge, the only Re standard available at the time of the data acquisition. The Re is oxidized (determined from the magnitude of the FT at a later point) but its oxidation state is unknown, therefore it will be referred to as ReO_x. The lower two spectra are those of the L_{III} edges of Re in the two samples. The only reliable information one obtains from their comparison is that the samples do not resemble the oxidized Re foil. In Fig. 6.6, the $\chi(k)$ of the Re edge from Sample 2 are shown for $\vec{E}$ parallel and $\vec{E}$ perpendicular (Re2, and Re2 P respectively). The two spectra resemble each other, though their intensities are different in certain regions.

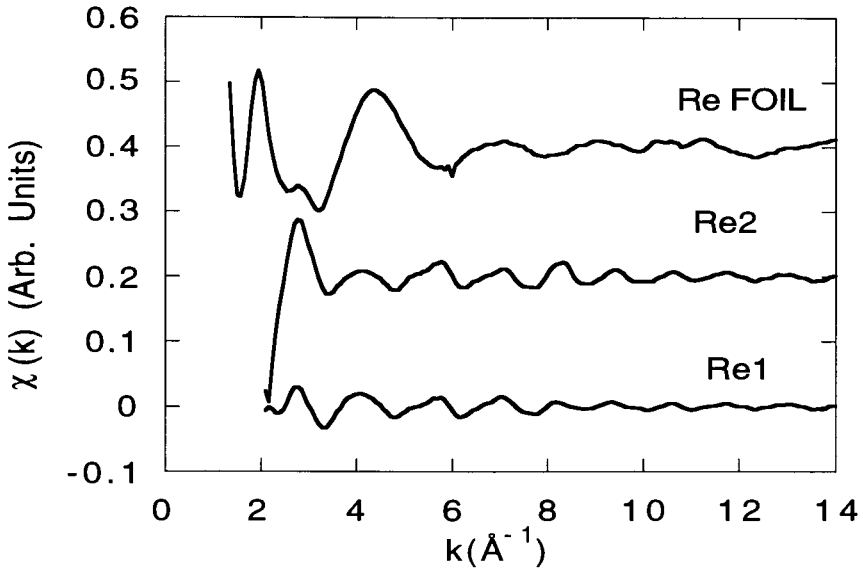

Figure 6.5. $\chi(k)$ Re L_{III} in ReO_x (taken in transmission) and Samples 1 and 2 with $\vec{E}$ parallel.

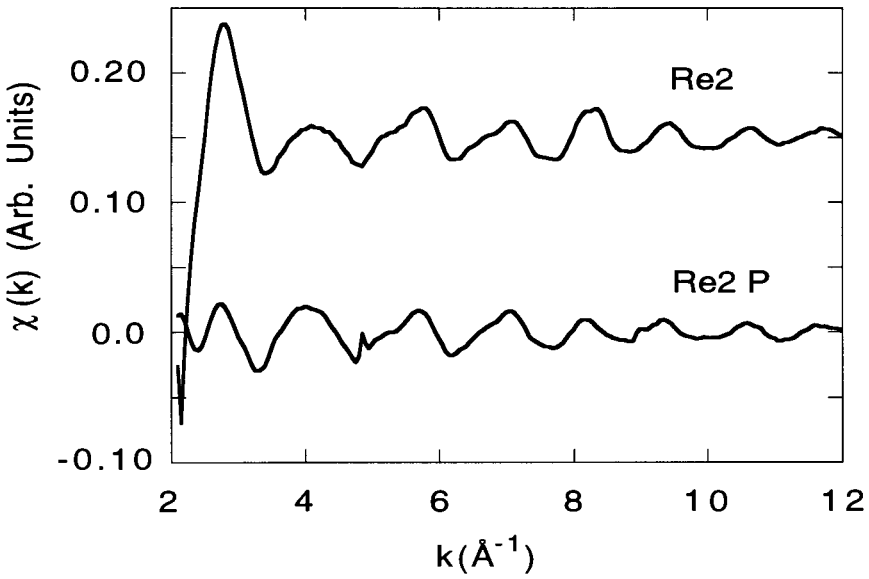

Figure 6.6 $\chi(k)$ of Re L_{III} edge of Sample 2 with $\vec{E}$ parallel and $\vec{E}$ perpendicular.

The FT of $k^3\chi(k)$ are shown in Fig. 6.7 to 6.10. The k^3 transforms were used to emphasize Co and Re over O. The FT of HCP Co is shown in Fig. 6.7 where the first peak contains the first two closely spaced shells of Co (R_1=2.494, R_2=2.505Å). The FT displayed below show two distinct peaks below 3.5 Å and no long range order. Their structure is shown in greater detail in Fig. 6.8 where the $\vec{E}$ parallel and $\vec{E}$ perpendicular configurations are given for each sample.

In all cases there seems to be the possibility of a peak at about 1.5Å, this is consistent with the presence of Co-O in the samples. The peak shown at roughly 2.3Å in the upper part of Figure 6.7, that of Co-Co in HCP Co and Co-Co in CoO which adopts the NaCl structure [1], seems to be mirrored in all FT of Fig. 6.8. The $\vec{E}$ parallel spectra show another clear peak, just below 3Å, which is also present in Co1P though absent in Co2P. This peak was attributed, through modelling of CoO (see Section 6.2 and Fig. 6.15), to the Co-Co peak in cobalt oxide's NaCl structure.

X-ray photoemission (XPS) results showed the Co in the samples to be 95% oxidized. The Re was determined to be roughly 95% Re and 5% ReO_2. These results were obtained from spectra taken at 90° and 30° of incidence. Ar^+ sputtering of the samples gave the following depth profiles:

Sample 1 $SiO_2/Co/Re \Rightarrow SiO_2/Re/ReO_2/Co/CoO$

Sample 2 $SiO_2/Re/Co/Re \Rightarrow SiO_2/Re/ReO_2/CoO$.

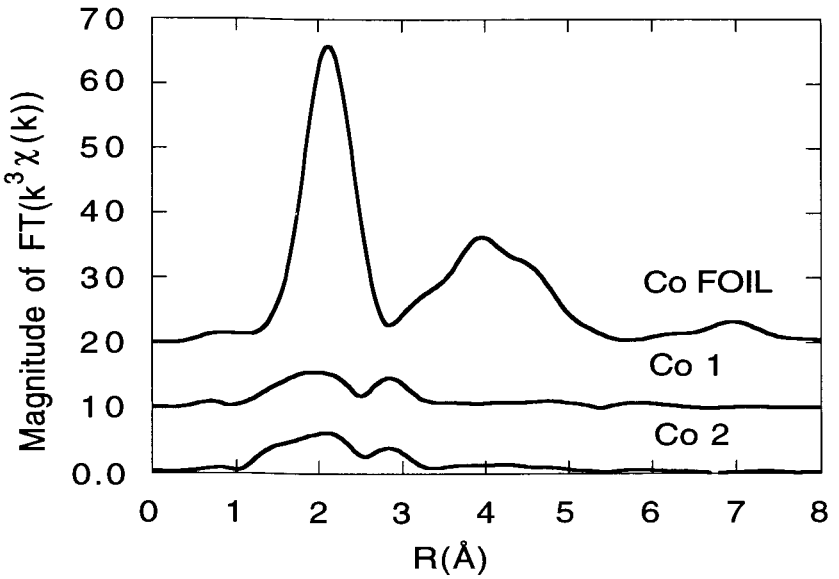

Figure 6.7. FT of $k^3\chi(k)$ of Co K-edge for HCP Foil, samples 1 and 2.

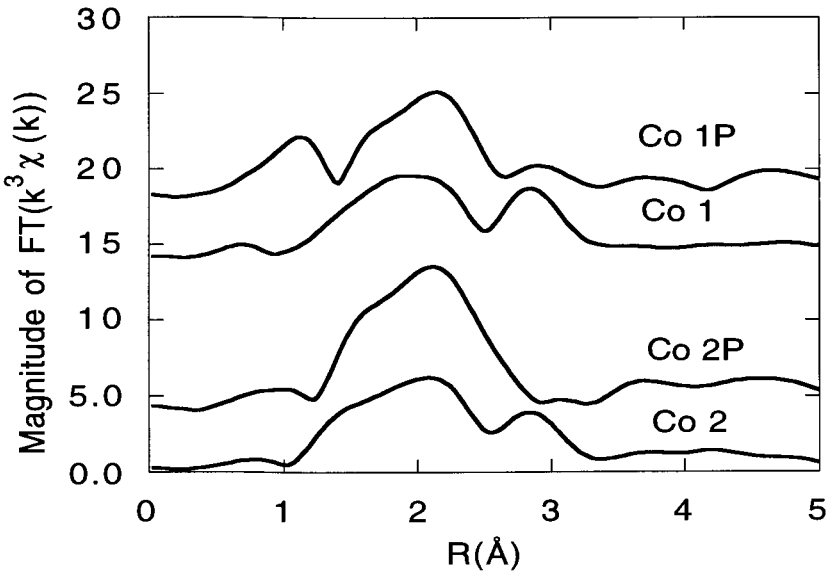

Figure 6.8. FT of $k^3\chi(k)$ of Co K-edge in samples 1 and 2 with $\vec{E}$ parallel (Co1, Co2) and $\vec{E}$ perpendicular (Co1P, Co2P).

There was no evidence of intermixing of the deposited layers with the substrate (XPS showed no SiO_2). All carbon found at the surface was C-C or C-O (adsorbates due to exposure). There was no evidence of the formation of carbides, even after Ar^+ sputtering. The result of sputtering was to clean the CoO off the surface leaving Co metal and Re metal.

The XPS results can be used in conjunction with the FT of the Co and Re edges in order to make a first assessment of their structures in the samples.

The FT in Fig. 6.9 shows the Re foil to be mostly ReO_2: generally in ReO_2 the Re-O bond lengths are between 1.0 and 2.10Å, the Re-Re are at 2.5Å [1]. This foil does not have a perfect ReO_2 structure, but rather presents a series of Re-O bond lengths. In Fig. 6.10, Re1 is compared to ReO_2: the Re-Re peak (2.5Å) in Re1 has higher magnitude than that of ReO_2. Both curves in the figure have a peak at 2.5Å which presents a small bump on the low-R side (~2Å): this may be an oxide (Re-O), or, it may be associated with the frequency content of the backscattering amplitude of Re associated with the Ramsauer-Townsend resonance. This small bump is quite evident in Fig. 6.11 on the FT of Re1, Re2 and Re2P. The differences in the FT obtained from the two polarizations are also shown in Figure 6.11 where Re 2P ($\vec{E}$ perpendicular to the surface) presents a single narrow peak, whereas Re 2($\vec{E}$ (parallel to the surface of the sample) shows some broadening, and a larger low-R bump. This reflects the anisotropy of the deposited film.

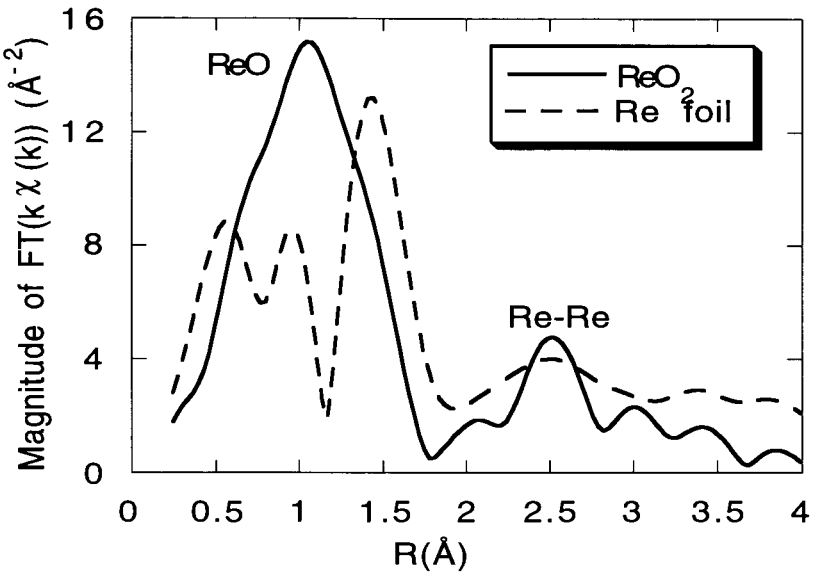

Figure 6.9. FT($k^3\chi(k)$) of Re L_{III} edge for the Re foil and theoretical ReO_2 (from FEFF6.10).

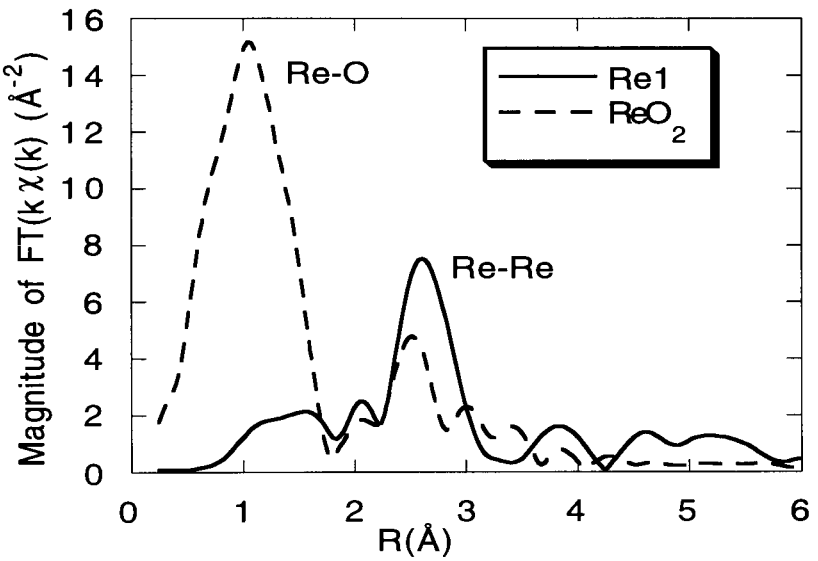

Figure 6.10. FT($k^3\chi(k)$) of Re L_{III} edge for Re1 and theoretical ReO_2 (from FEFF6.10).

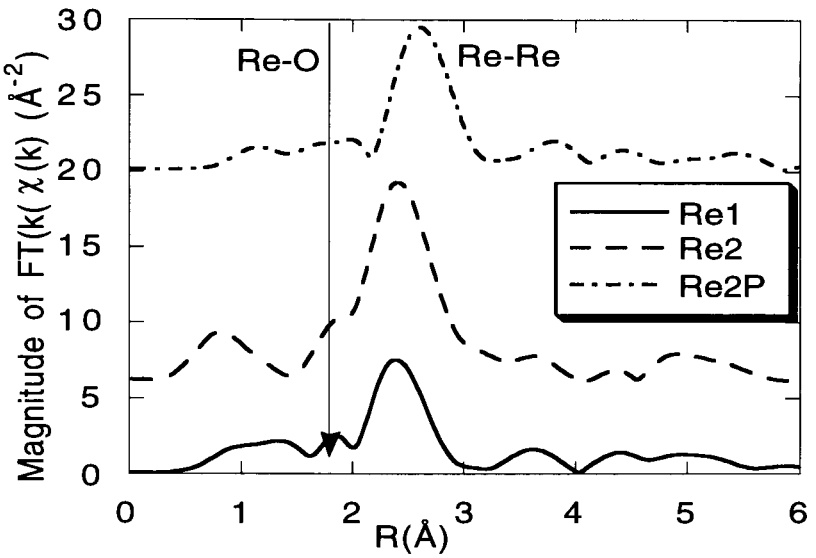

Figure 6.11. FT($k^3\chi(k)$) of Re L_{III} edge of Sample 2 with $\vec{E}$ parallel (Re 2), and $\vec{E}$ perpendicular (Re 2P).

Following the procedure outlined in Chapter V, Section 1.1, for the beating analysis, the FT of the data were back-transformed over a range of specific peaks in R-space. Once the amplitude and phase were isolated, the derivative of the phase was plotted, and the values of ΔR evaluated from the beat nodes (see Eq. 5.2).

The derivative of the phase for the HCP Co foil, plotted in Fig. 6.12, shows no nodes over the R-space range chosen that can be associated with R_1 and R_2. From the known crystal structure of HCP Co the difference between the first two shells is 0.011Å (R_1-R_2=0.011Å). The first beat node would occur at k_1=142.8Å^{-1}. The other curves in Fig. 6.12 show that Co1 and Co2 have two shells under the first peak

that are equally distant from one another in each sample ($k_1 \simeq 3.6$Å^{-1}). Within the error possible from the range of available data, the first two shells will be separated by 0.43Å in both samples. One of the two is Co-Co, the other Co-O, as can be seen from the first peak of the FT of Co1 in Fig. 6.15.

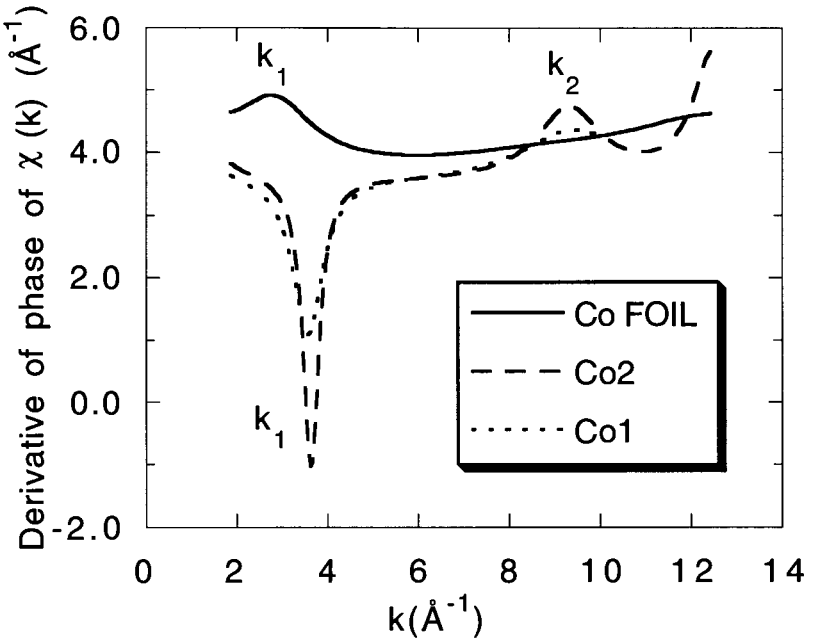

Figure 6.12. Derivative of the XAFS phase extracted from the FT of $k^3\chi(k)$ with a 10% Gaussian window over a k-space transform range from 1.71 to 12.44Å^{-1}. The filtered R-space was 1.18 to 2.29Å. The first beat node, k_1, is at 3.60^{-1}Å for both Co1 and Co2, k_2 is at 9.34Å^{-1}. The shallow inflection for Co is at k_1=2.87±0.12.

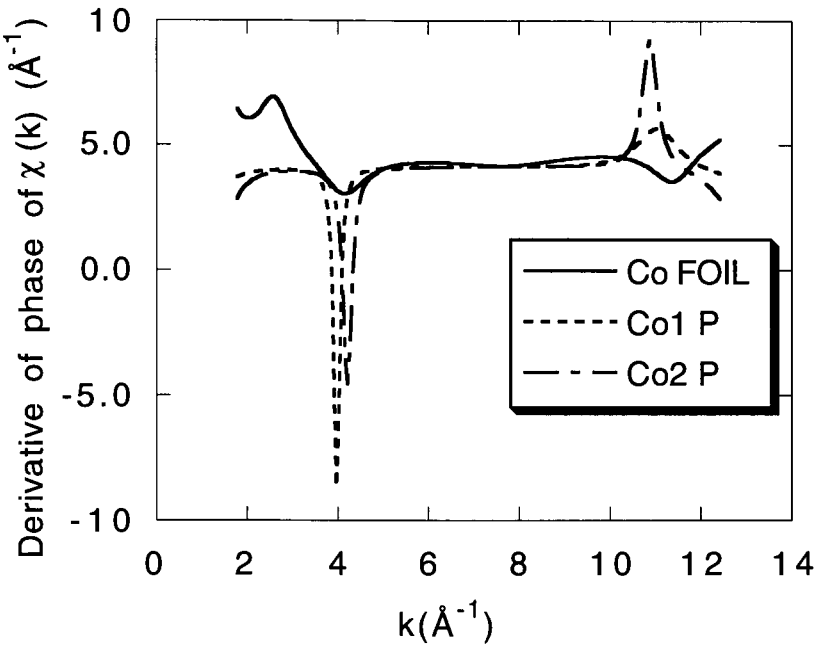

Figure 6.13. Derivative of the XAFS phase extracted from the FT of $k^3\chi(k)$ with a 10% Gaussian window over a k-space transform range from 1.71 to 12.44Å^{-1}. The filtered R-space was 1.538 to 2.647Å. The first beat node, k_1, is at 3.97, and 4.22Å^{-1} for Co1 and Co2, k_2 is at 11.08 and 11.89Å^{-1} respectively. The small dip in the HCP Co is at 2.87Å^{-1}

Figure 6.13 shows the derivative of the phase of the first peak of the Co edge for Co 1P and Co 2P, which correspond to data taken from samples 1 and 2 with the $\vec{E}$ vector perpendicular to the surface of the sample. The spacing of the first two shells is shown to be different from one sample to the other, contrary to the results obtained with $\vec{E}$ parallel to the sample. In Co 1P the position of the first beat node leads to a ΔR of 0.37Å, in Co 2P this distance is found to be 0.40Å. Where the Co Foil is concerned, the shallow dip at

$2.87\pm0.12\text{Å}^{-1}$ corresponds to a ΔR of 1.64 ± 0.07Å, which is the distance between the first two shells and the third of an HCP structure of Co, distance between Co-Co and Co-O in an NaCl structure.

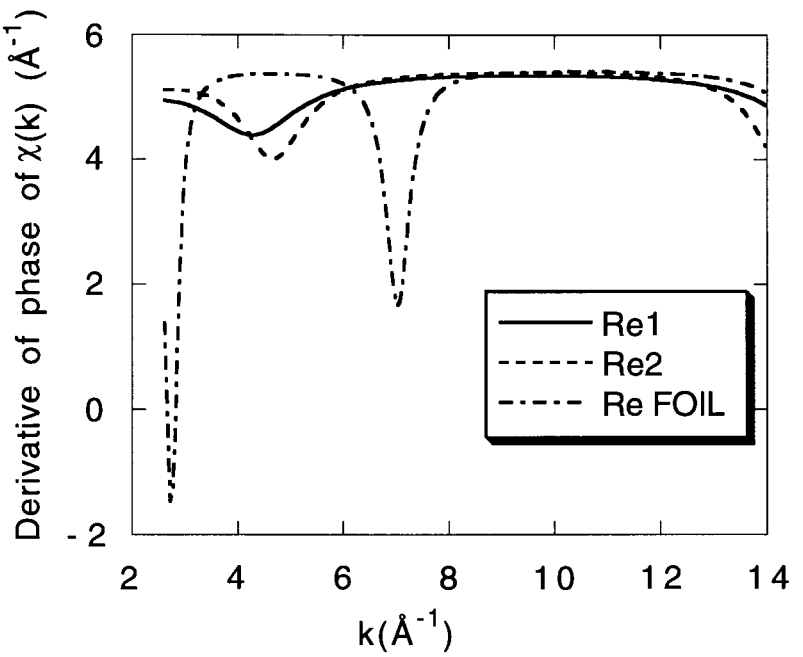

Figure 6.14. Derivative of the XAFS phase extracted from the FT of $k^3\chi(k)$ with a 10% Gaussian window over a k-space transform range from 2.57 to 14.00Å^{-1}. The filtered R-space was 2.36 to 3.12Å. The first beat nodes, k_1, are at 4.29, 4.72, and 2.78Å^{-1} for Re1, Re2, and Re FOIL respectively, k_2 is above 13.94 for Re 1 and Re2, and at 7.04 Å^{-1} for Re FOIL.

In Fig. 6.14 the derivative of the phase is plotted for a back-transform range which covers the peak in the FT that all three

samples have in common (see Fig. 6.11) and which extends from 2.36 to 3.12Å (ie the position of a metal peak composed of the first two shells of Re). The foil, which was determined earlier to be oxidized, has a small intensity peak in this region which is composed of two shells distant by 0.56Å (the Re-Re and Re-O) from one another. The Re 1 and Re 2 samples have two shells which are found to be 0.36Å and 0.33Å apart. Re 2P is found to have two shells spaced by 0.36Å in the same region. This value corresponds to that found for Re 1, but is higher than that for Re 2 with the $\vec{E}$ vector parallel to the sample.

The analysis of the beating for the main peaks of the FT of Co 1, Co 2, Re 1, and Re 2 shows two shells separated by roughly the same distance as is found in their oxides.

2. Modelling Results

The results of modelling are inconclusive. The Co in the bilayers does not seem to be in a perfect NaCl structure [1]. A combination of NaCl CoO and BCC Co is proposed for the Co edges of both films. Figure 6.15 shows the magnitudes of the FT for the first two shells of NaCl CoO, the two shells of HCP Co, and of the Co edge in sample 1.

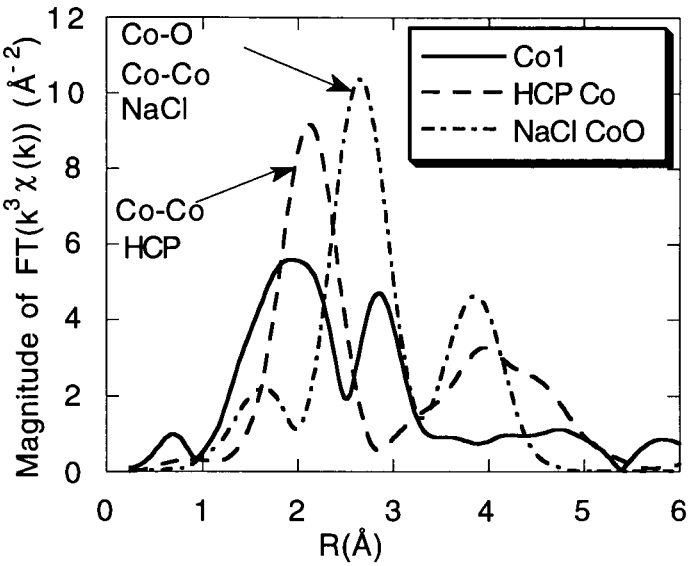

Figure 6.15. Magnitudes of the FT of $k^3\chi(k)$ of the first two shells of NaCl CoO, HCP Co and of Co1 (the Co edge in sample 1). The k-space range was 1.70 to 12.3Å^{-1}.

CHAPTER VII: Conclusions and Discussion

The structural properties of magnetic multilayers were investigated using XAFS. The modified Fe/Cu/Fe layers, as well as the Ag(001)/5ML Fe/10ML Au and Ag(001)/10ML Cr/10ML Au were found to have tetragonally distorted structures. Ferromagnetic resonance measurements were made on the Fe/Cu/Cr/Cu/Fe multilayers many months after the XAFS was performed, and no ferromagnetic signal attributed to the trilayer structures was observed.

It proved possible, using the total reflection technique, to probe 3ML, or 6ML, of Cr, buried under a total film thickness of 32Å. Without the total reflection of the x-rays in the sample it would not have been possible to obtain enough fluorescence from such a thin film of Cr in order to measure its structure.

From the results with $\vec{E}$ parallel to the substrate, the R_1 and R_2 values were used to calculate the lattice parameter *c* perpendicular to the films. From the $\vec{E}$ perpendicular measurements of the Cu K-edge in the 3ML Cr film it was seen that the structural disorder in the plane of the film is effectively larger than that perpendicular to it.

The results of the fitting of the first peak of the FT of the MBE films are given in Table 7.1.

Table 7.1. Parameters for the first two coordination shells of the MBE films obtained by curve fitting the first peak of the FT of the data. The values for the Cu edge in the 3ML Cr sample (8.7 Fe/3 Cu/3 Cr/3 Cu/5 Fe) are the values for $\vec{E}$ parallel. The 6ML Cr sample refers to the 8.7 Fe/3 Cu/6 Cr/3 Cu/5 Fe sample, the 5ML Fe to the 5ML Fe/ 10ML Au sample, and the 10ML Cr to the 10ML Cr/10ML Au sample.

Sample	Element	a (±0.01)	c (±0.03)	N_1±0.5	N_2±0.5	Δ(c/c)% Measured ±0.06%	Δ(c/c)% Calc. ±0.05%
6 Cr	5Fe	2.83	2.86	6.0	5.4	-0.23	+0.42
	3Cu	2.84	2.91	7.0	6.5	+0.91	+1.01
	6Cr	2.86	2.92	6.1	5.7	+1.25	+0.10
3 Cr	3Cu	2.83	2.89	6.2	5.6	+0.36	+0.53
	3Cr	2.84	2.80	7.0	6.3	-2.90	+0.35
5 Fe	5Fe	2.87	2.90	6.9	6.2	+1.17	+0.79
10 Cr	10Cr	2.90	2.96	6.25	5.65	+2.63	-0.14

It proved useful to fit the first peak of the FT to a polarization-independent model in order to determine the structure of the growths, then to optimize the results for higher shells with a fully polarization-dependent simulation of the films. The simulation of the higher shells required that the Debye temperature be added as a direct parameter in the model. Simulations using a θ_D which was a weighted average of those of the elements surrounding the absorber proved useful. In the case of the Cr edge in the 6ML of Cr sample, the effective Debye temperature of the film was estimated to be θ_D=461K by using the Cu-Cr reduced mass for the upper and bottom two Cr layers, and keeping the Cr θ_D for the middle two Cr layers.

Assuming that, to a zeroth order, a thin film can be considered an elastic continuum even when it is covered by another film, then elasticity theory can be used to predict the expansion of the lattice perpendicular to the substrate. Taking into consideration the uniaxial strain ($\varepsilon=\Delta a/a$ as described in Eq. 1.2) in the plane of the surface, measured with $\vec{E}$ parallel to the sample's surface, the expansion of the lattice along *c* is given by Eq. 7.1:

$$(7.1)\quad \frac{\Delta c}{c} = -2\frac{C_{12}}{C_{11}}\frac{\Delta a}{a}$$

where the coefficients C_{11} and C_{12} are the elastic coefficients in a cubic crystal, and the strain, or stress, are in the (001), or (100), directions. The values of the ratio $2C_{12}/C_{11}$ are 0.59, 0.72, and 0.19 for Fe, Cu, and Cr respectively [1], $\Delta c/c=(c_{measured}-c_{bulk})/c_{bulk}$, and $\Delta a/a$ is the lattice mismatch. The analysis of the MBE films leads to the conclusion that the in-plane lattice strains caused by the growth of the films are generally not sufficient to give the corresponding changes along *c*. In the case of the 6ML of Cr sample, the *c* lattice parameter gets larger as the in-plane lattice parameter increases, overall the volume of the unit cell decreases as further films are deposited on the sample. Since the structure is being measured after the entire multilayer system has been epitaxially grown, any effects of structural relaxation or reconstruction are thus included. This is in contrast with *in situ* measurements of layer-by-layer growths where the layers will be subjected to different stresses.

The 5ML of Fe, and the 10ML of Cr grown at RT, grow to a BCT structure which is much closer to the BCC one than an FCC, notwithstanding the underlying FCC Ag(001) substrate. The changes in the *c* parameter (from a perfect BCC structure) cannot be accounted for by the slight in-plane expansion in the case of 10ML Cr since the experimental *c* parameter increases, rather than decreases. Nor, in the case of the 5ML Fe, does the small in-plane lattice contraction explain the out-of-plane expansion.

Since the in-plane strain generally produces an expansion or contraction in the the vertical atomic layer spacing because such an effect reduces the change in atomic volume, the knowledge of both in-plane and vertical changes are necessary to uniquely determine the structure. During growth, the combination of RHEED (or LEED) and x-ray photoelectron or Auger electron forward scattering provide information on the morphology of the sample's growth. In this manner, it is possible to collect information on a few layers at a time. Ideally the strain ought to be measured layer-by-layer on a free surface. The addition of *in-situ* XAFS into the growth monitoring process would provide both in-plane and vertical information. Final structural information of the buried interlayers would be possible with XAFS, as opposed to the other techniques which provide information on only the top few layers.[2]

---

[2] These measurements will soon be possible on the UHV/MBE XAFS beamline that Professor Crozier is building for the Pacific Northwest Consortium Collaborative Access Team (PNC-CAT) beamline at the Advanced Photon Source.

In general, the coordination numbers in the ultrathin films were determined unambiguously by varying N_i and σ_i^2 over a range of their values and finding a corresponding region in parameter space where the χ^2 was minimized for both. The values of the coordination numbers found in this manner correspond to those found with theoretical models for thin films [1].

The structural disorder in the films was found to be greater than in the bulk elements, and in all cases it was greater in the plane of growth than perpendicular to it. Further studies of the surface roughness ought to be done using *in situ* XAFS reflectivity measurements. In this fashion it would be possible to grow coupled structures and determine the effect of atomic length-scale surface roughness on the coupling.

Though Cu and Cr are five elements apart in the periodic table, the differences in their amplitudes and phase shifts were not large enough to easily address the question of their possible interdiffusion. It was necessary to use their differences in the theoretical backscattering amplitudes and phases at low-k, as well as to model the films in order to distinguish one from the other. In this way it was found that neither Cr nor Fe was detected in the Cu, and no Cu was detected in the Cr in the first peak of the FT (ie for R_1 and R_2) of the Fe/Cu/Cr/Cu/Fe multilayers, as is evident in Fig. 5.26. Further simulations showed that the excess intensity of higher Cr peaks in the multilayers (~4.5Å) could be directly attributed to the Cu overlayers.

In general if a film with a higher melting point is grown on a film with a lower melting point there will be interdiffusion between

the two [2]. In the opposite case (the melting point of the adsorbed layer is lower than that of the substrate) no interdiffusion occurs. For Cr and Cu this would lead to interdiffusion when Cr is deposited on Cu. This was not detected for 6ML of Cr, but simulations of the 3ML of Cr sample showed that a quarter of the bottom Cr layer had intermixed with the Cu.

Not much is known about the effect of lattice strain in Cr on the magnetization of ultrathin films of Cr [2]. It is expected that the magnetization of the Cr in the 6ML Cr sample will be affected by the proximity of the Fe layers [3]. The magnetization state of ultrathin layers, whether of Cr or Fe, seems to depend primarily on interface roughness rather than on the lattice strain of the structure. In particular, the small strain percentages measured here are deemed to be insignificant with respect to the overall magnetization of the layers [3].

Appendix 1: Fitting Procedure

The following describes the fitting procedure used to obtain structural parameters from XAFS data. A brief summary of the steps followed in single scattering fitting is given in A.1.2, where the procedure followed in order to fit the first and second nearest neighbours of BCC Cr foil is detailed. Multiple scattering fitting is covered in A.1.3.

A.1.1. Summary of Single-scattering Fitting Procedure

The fitting of the data sets to a single-scattering model was done in R-space, simultaneously fitting the Real and Imaginary parts of the FT of the model to those of the data. The FT of both the data and the model were calculated in the same manner using the Fast Fourier Transform [2.13] in order to minimize transform artefacts. The program used is called EXAFIT [1], and the amplitudes and phases were calculated using FEFF6.10 [2]. The following expression was fit:

$$\chi(k) = S_0^2 \sum_j \frac{1}{k} A_j(k) \frac{N_j}{R_j^2} e\left(-\frac{2R_j}{\lambda}\right) e^{-2\sigma_j^2 k^2 x} \sin\left(2kR_j + \Phi_{Tj}(k) - \frac{4}{3} C_{3j} k^2\right) \tag{2.10}$$

S_0^2 was fixed at the value found for the bulk elements (between 0.8 and 0.85 for the transition metals studied here). The k-space range was shifted by the ΔE_0 of the bulk elements using Eq. 2.11:

$$(2.11) \qquad k_j = \left[k^2 - \frac{\Delta E_j}{\gamma} \right]^{1/2} \qquad \text{where } \gamma \equiv \frac{h^2}{8\pi^2 m_e} \simeq 3.81$$

for E in eV, and k in $Å^{-1}$.

The ΔE_0 (necessary to adjust the theoretical potential to that of the data) were fixed to be equal for all shells having the same scatterers [5.5] and were found by either fitting the first peak of the FT of the corresponding bulk element, or by fitting the unknown data while allowing all parameters of the first two shells to vary. In a first instance, all parameters were varied in order to find their minima in parameter space. For sets of two highly correlated variables (eg. N and σ^2, or R and ΔE) a subset of mutual minima were found by fixing one variable at its minimum and varying the other, then repeating the procedure after reversing the variables. This will give an area in parameter space over which both variables are minimized. The model $\chi(k)$ was then moved to the minima by setting each variable to its absolute minimum. The range of fitting was limited to a region in parameter space which doubles the χ^2. The model was then least-squares fit to the data using EXAFIT. The error bars for each parameter were found by observing the range of the variable which doubles the χ^2. The details of Eq. 2.10 are given in Chapter 2, Section

3.4. The asymmetry due to deviations from a Gaussian distribution of atomic positions was investigated by curve fitting, and found to be close to the theoretical values for the bulk [5.6]. The value for each shell was therefore set equal to its bulk value and remained fixed during the fitting. For the first and second nearest neighbours, only four parameters were allowed to vary during the fitting: R_1, R_2 and their corresponding mean-squared relative displacements σ_1^2 and σ_2^2.

A.1.2. First and Second Nearest Neighbours: Single Scattering

The example chosen is data taken in transmission through a BCC chromium foil. The background was removed using the standard procedure, and the data normalized, as was outlined in Chapter II, Section 3.

Beat analysis of the first peak of the Fourier transform of $k\chi(k)$ (k-space range from 1.1 to 13.9Å^{-1}and R-space from 1.07 to 3.00Å) revealed the presence of two peaks, separated by about 0.38Å. The fitting procedure therefore consists of fitting the first and second shell of Cr to the region in R space (both the Real and the Imaginary parts) from 0.932, to 3.01Å. The K-space range of data considered usable (no excessive noise) was from 1.85 to 13.70 Å^{-1}.

The amplitudes and phases were obtained from FEFF6.10 [2], setting RGRID to 0.01, giving the Debye temperature of bulk BCC Cr (485K),

and specifying that all possible paths were to be calculated. The crystallographic parameters of pure BCC Cr [3] are given in Table A.1, where R_j is the radius, N_j the coordination number, C_{3j} the asymmetry term, S_j the difference from the σ_j^2 of bulk Fe [4] (only value measured for a similar BCC metal), and Δ the energy shift required to correct the inner potential, for each shell j. These parameters were input into EXAFIT in order to fit the theoretical $\chi(k)$, Eq. 2.10, of BCC Cr to the BCC Cr data taken in transmission.

Table A.1. Crystallographic parameters for BCC Cr.

R_j(Å)	N_j	C_{3j}(x10^{-3}) (Å^3)	S_j(Å^2)	Δ(eV)
2.4975	8	0.027	0.0	0.0
2.8839	6	0.0342	0.0	0.0

Since no reported values of the mean square relative displacements (σ_j^2) of Cr are available, the experimental values of the σ_j^2 for Fe were used as a starting point to create the amplitudes rather than modelling them with the Debye model as done in FEFF 6.10. The theoretical values for Fe are 5.10 and 5.92x10^{-3} Å^2, and the experimental results are 5.05 and 6.6x10^{-3} Å^2. Since Cr and Fe are quite similar in structure, it is useful to start the fitting with the experimental σ_j^2 of Fe and thus preserve the ratio of σ_2^2 to σ_1^2. The program will therefore compute the differences from these values, S_j, which will allow us to evaluate the parameters σ_1^2, and σ_2^2 for Cr. The premise followed here was that all BCC metals have a mean

square relative displacement which is higher for the second shell than for the first one [6]. In order to conserve a ratio of σ_1^2 / σ_2^2 which is close to that of Fe the value of S_2 was controlled to move in the same direction as that of S_1 . The energy shifts are the same for the first and second shell ($\Delta E_1 = \Delta E_2$) and are set equal to zero to start. The values of C_{3j} were approximated using α, the thermal expansion coefficient of the bulk metal at room temperature, R, the radius of the corresponding shell, and T, the temperature at which the data was taken (room temperature in all cases): $C_{3j} \approx 2\alpha\sigma_j^2 R_j T$ ($Å^3$) [5].

Setting the parameters to the values outlined above leads to the fit shown in Fig. A.

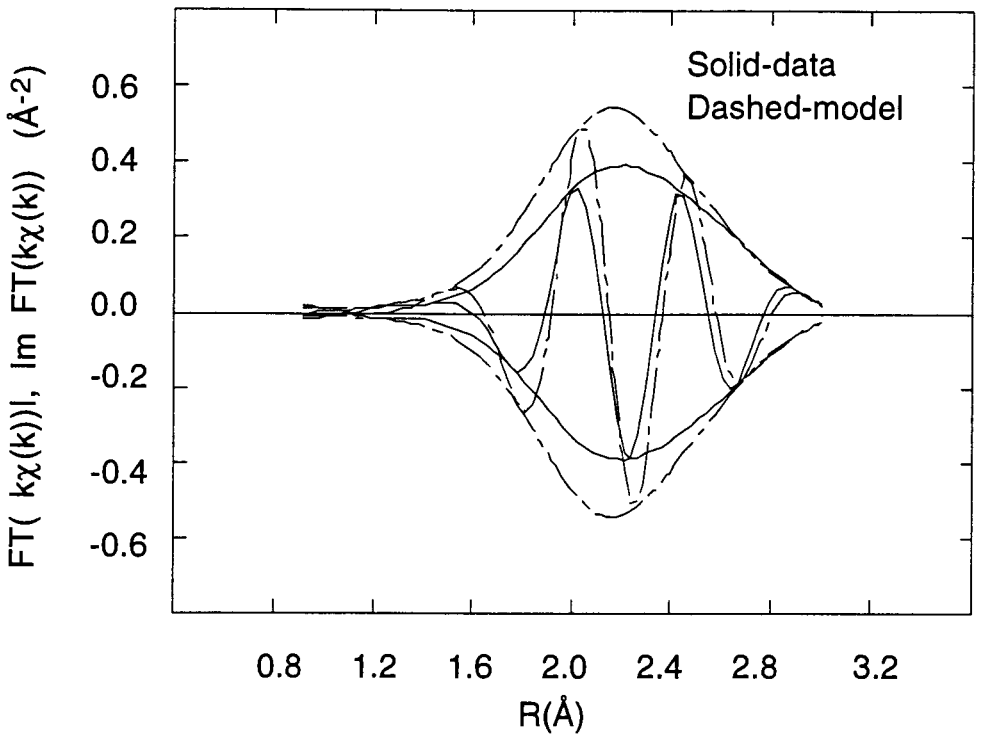

Figure A.1. Fit of Cr foil using the parameters outlined in Table A.1 The solid line is the data and the dashed line represents the trial fit. The k-space range is 1.85, to 13.70 $Å^{-1}$, the R-space range from 0.932 to 3.01Å, a 10% Hanning window was used (Eq. 2.14.b). The magnitude of the FT is the envelope, and the Imaginary part is the oscillatory part.

It is obvious that the amplitude of the fit, the theoretical amplitude, overestimates the real amplitude. This happens because no empirical value of S_0^2 has been used. We multiplied the theoretical amplitude by 0.85, by multiplying N_1 by 0.85, in order to better approximate the data. Figure A.2 shows the result of changing N_1 to 6.8, keeping $N_2/N_1=0.75$.

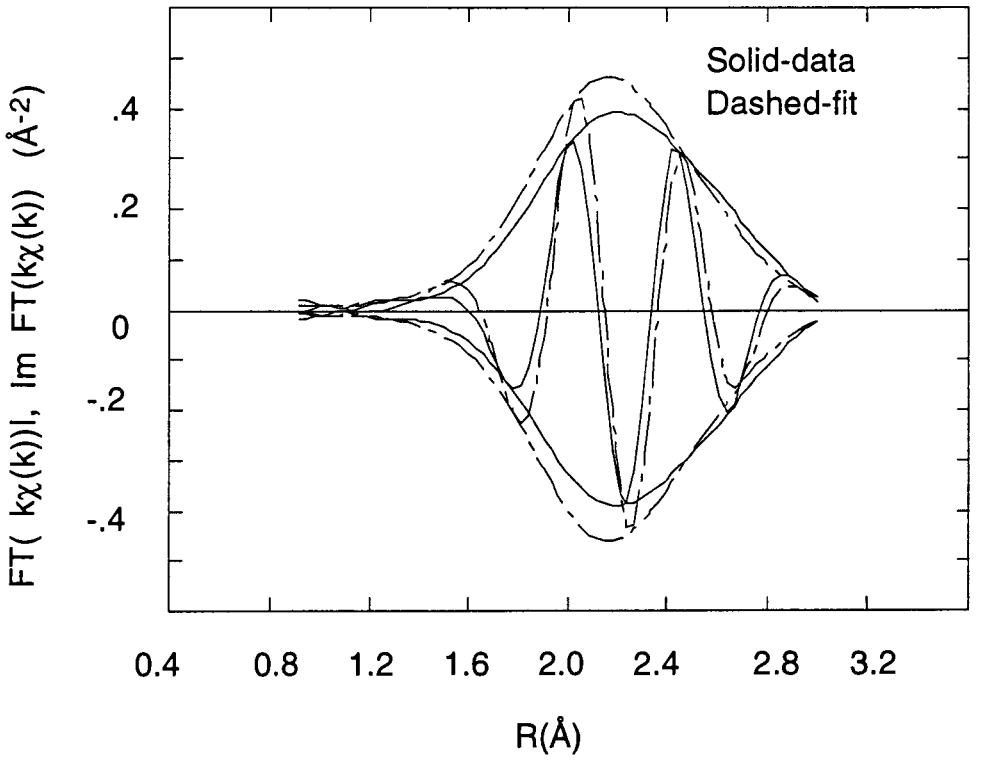

Figure A.2. Fit of Cr foil with $N_1=6.8$ (equivalent to $S_0^2=0.85$) and all other parameters as described in Table A.1. The window function, and the R- and k-space ranges are the same as in Fig. A.1. The magnitude of the FT is the envelope, and the Imaginary part is the oscillatory part.

It is evident that the E_0 of the model and the data do not coincide: in order to get the imaginary parts to coincide it is necessary to adjust E_0 for the model. Later on it will be necessary to verify this choice by allowing both E_0 and R_i to vary simultaneously. The result of a 4.6 eV shift is shown in Fig. A.3.

The amplitude still seems a bit high, so we fixed N_1=6.6. At this point the starting condition for the actual least-squares fitting has been reached, as is shown in Fig. A.4.

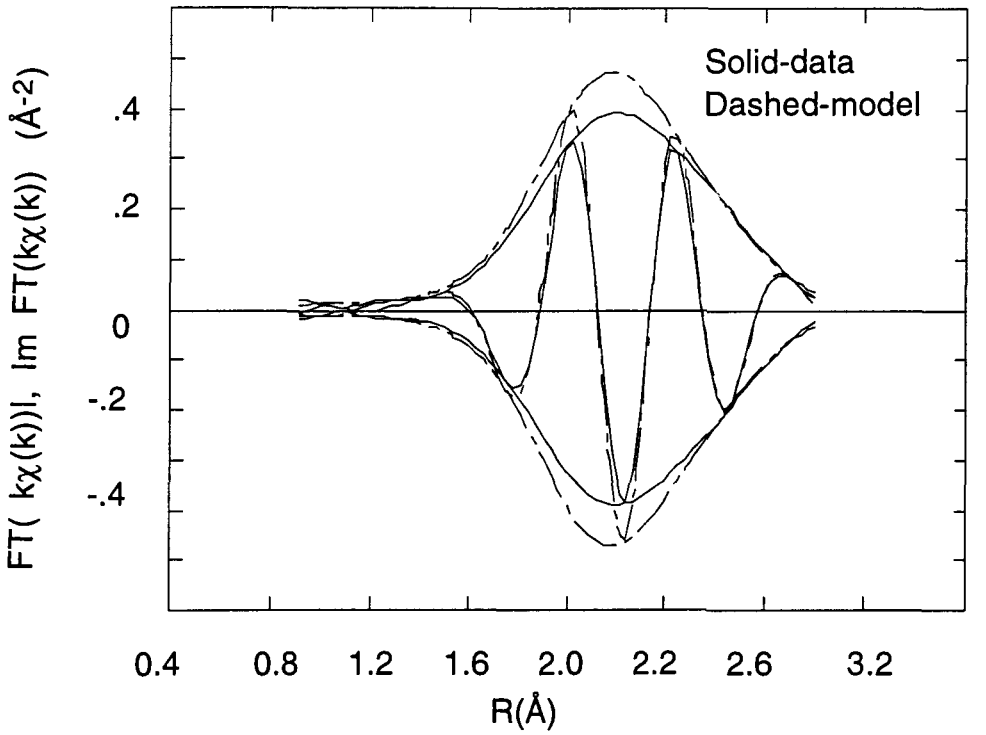

Figure A.3. Fit of Cr foil with ΔE_0=4.6 eV. The solid line is the data and the dashed line represents the trial fit. The window function, and the R- and k-space ranges are the same as in Fig. A.1. The magnitude of the FT is the envelope, and the Imaginary part is the oscillatory part.

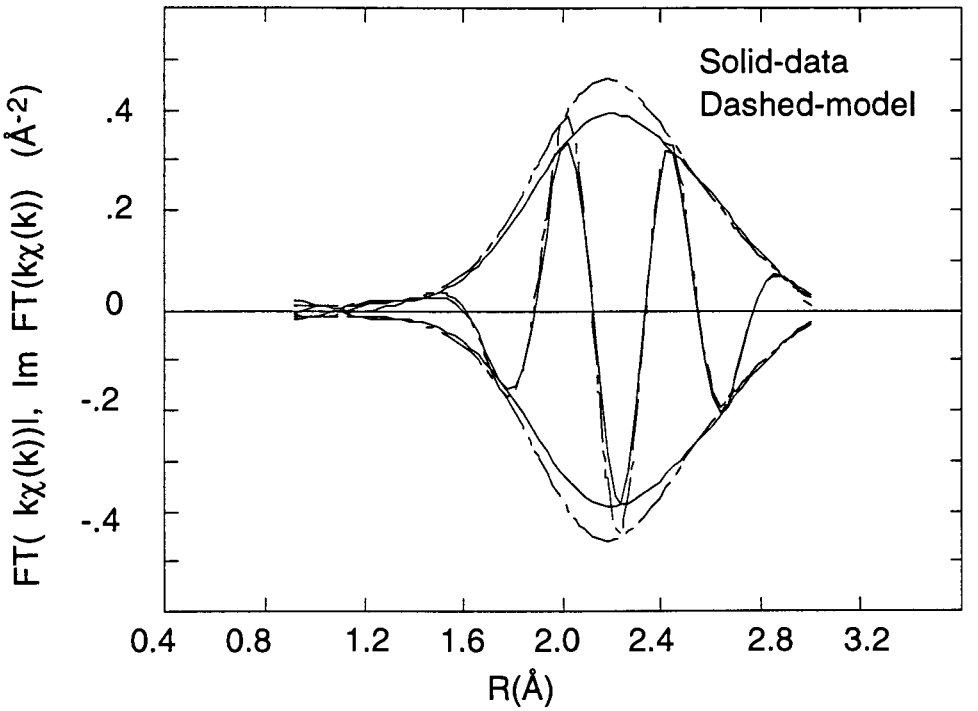

Figure A.4. Fit of Cr foil with N_1=6.6, ΔE_0=4.6 eV, and all other parameters as in Table 1. The solid line is the data and the dashed line represents the trial fit. The window function, and the R- and k-space ranges are the same as in Fig. A.1. The magnitude of the FT is the envelope, and the Imaginary part is the oscillatory part.

It now is possible to allow the various parameters to vary. One choice is to keep the region which seems to fit well, the second shell, constant. Varying ΔE_1, R_1, and σ_1^2, while keeping all the other parameters fixed at the starting points gives the following result, shown in Fig. A.5. The results of this fit are given in Table A.2.

It seems that there is a lack of amplitude on the high R side of the Fourier transform, as well as a problem with the amplitude of the first shell. The value of N_1 is lower by 12.5% than would be expected in a BCC structure, yet the amplitude of the model exceeds that of the data in the mid-R region.

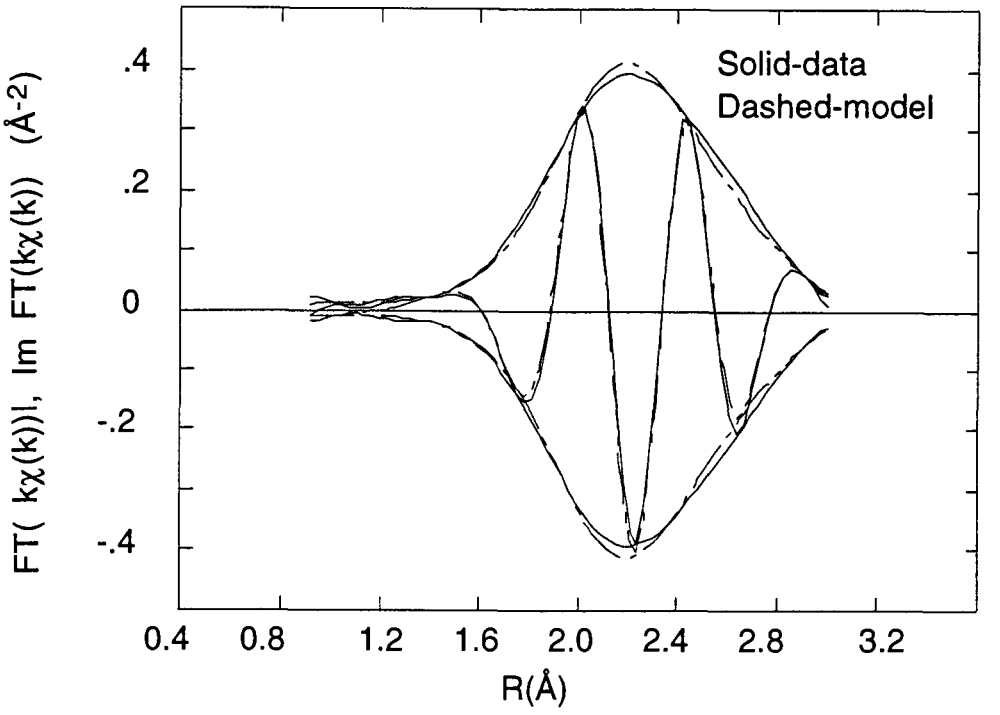

Figure A.5. Fit of Cr foil where ΔE_1, N_1, and R_1 vary. The solid line is the data and the dashed line represents the trial fit. The window function, and the R- and k-space ranges are the same as in Fig. A.1. The magnitude of the FT is the envelope, and the Imaginary part is the oscillatory part.

It seems that there is a lack of amplitude on the high R side of the Fourier transform, as well as a problem with the amplitude of the first shell. The value of N_1 is lower by 12.5% than would be expected in a BCC structure, yet the amplitude of the model exceeds that of the data in the mid-R region.

Table A.2. Fit parameters for BCC Cr using a two shell model. The ratio of R_2 to R_1 has been fixed at the crystallographic value of 1.15471, that of N_2 to N_1 at 0.75, the asymmetry terms are fixed at their theoretical values, the σ_j^2 are fixed at 0.0 ($Å^2$), and ΔE_2 is constrained to be equal to ΔE_1. The N values have been divided by the temporary value of S_0^2 (0.825) in order to make the comparison to the BCC values straightforward.

R_j(Å)	N_j	C_{3j}(x10^{-3}) ($Å^3$)	S_i($Å^2$)	Δ(eV)
2.504	7.0	0.0227	0.0	5.7
2.891	0.75xN_1	0.0342	0.0	5.7

Allowing R_1, N_1, R_2/R_1, σ_1^2, and N_2/N_1 to vary gives a reasonable quality fit through the whole R-space range as is shown in Fig. A.6, but, as can be seen from the results of Table A.3, the N_2/N_1 ratio (=1.06) is much higher than is physically possible for a BCC structure. However, fixing N_2/N_1 at 0.75 and varying the remaining parameters gives a value of R_2 which is 0.02Å larger than the XRD value (x-ray diffraction result) [3], given in Table A.1, and is therefore not a valid solution.

Table A.3. Parameters for the fit shown in Fig. A.6.

R_j(Å)	N_j	C_{3j}(x10^{-3}) ($Å^3$)	S_i($Å^2$)	Δ(eV)
2.509	7.8	0.0227	0.7	5.7
2.879	8.25	0.0342	3.58	5.7

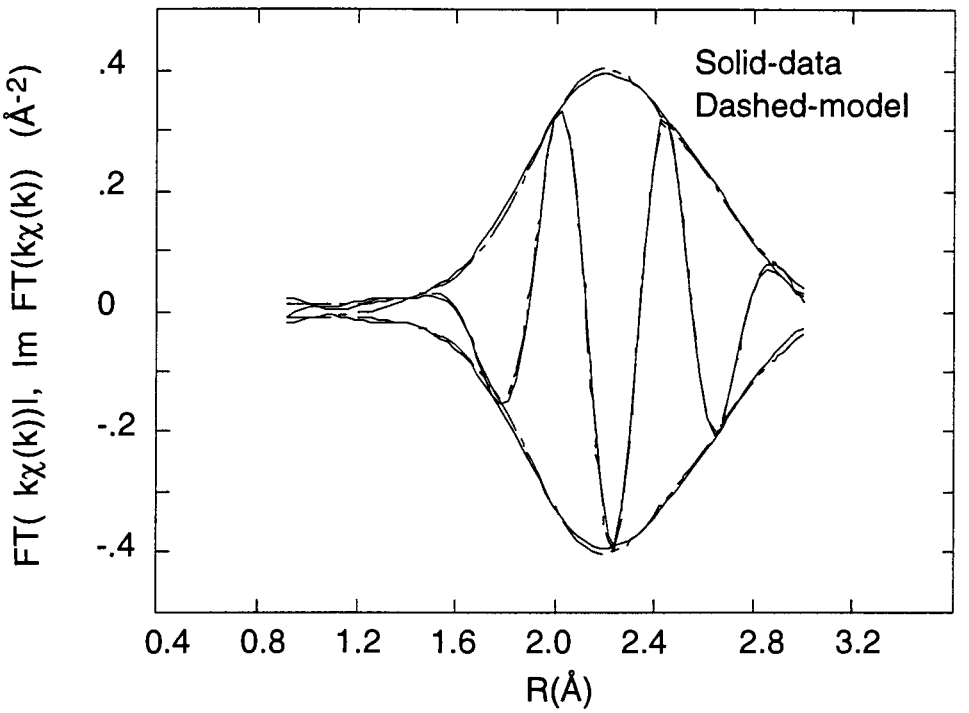

Figure A.6. Fit of Cr foil with R_1, N_1, R_2/R_1, σ_1^2, and N_2/N_1 varying. All other variables are fixed at the values of Table A.2. The solid line is the data and the dashed line represents the trial fit. The window function, and the R- and k-space ranges are the same as in Fig. A.1. The magnitude of the FT is the envelope, and the Imaginary part is the oscillatory part.

The value of N_2 may be artificially high (it should be $0.75 \times N_1$ in a BCC structure) because the σ_2^2 for the second shell may be too high. However, the lack of amplitude which is being compensated for by a high N_2 may reflect the presence of intensity coming from multiple

scattering paths[1] which are located just beyond the second shell, at 3.93Å. These paths have not yet been included in the model.

In order to determine whether the data requires the fitting of four shells to the first peak (two nearest neighbour paths, and two sets of multiple scattering paths) it is necessary, in a first instance, to carry the fit through in its present form, in other words without taking into account any multiple scattering, to evaluate how realistic it is for two shells only. It now becomes imperative to verify that these values are at an absolute minimum of the residual sum of squares, the $\chi 2$ given in Eq. 2.13, and not some local minimum. In order to do so the EXAFIT program can be used to calculate the $\chi 2$ for each parameter. The following figures show these calculations, the results of which will be given later on.

---

[1] The triangular multiple scattering paths are, for a BCC or BCT structure, paths leading from the absorber to a body center, then to a corner and back to the absorber, or, from the absorber to a body center, then to another body center one lattice parameter away, and back to the absorber.

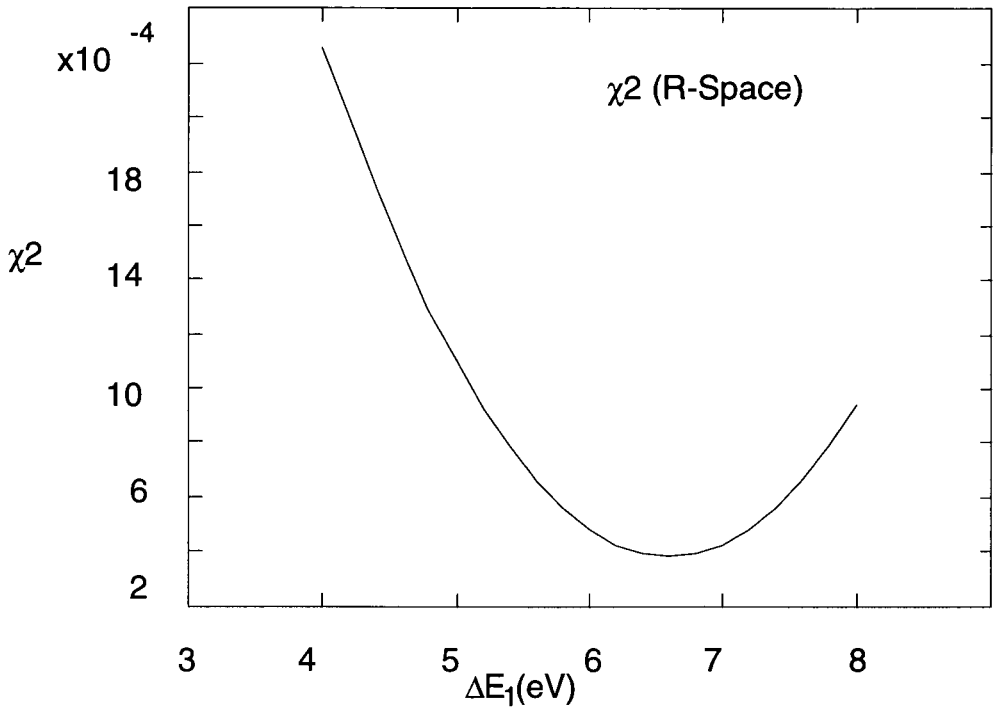

Figure A 7. χ^2 plot of ΔE_1 showing the region from 4.0 to 8 eV.

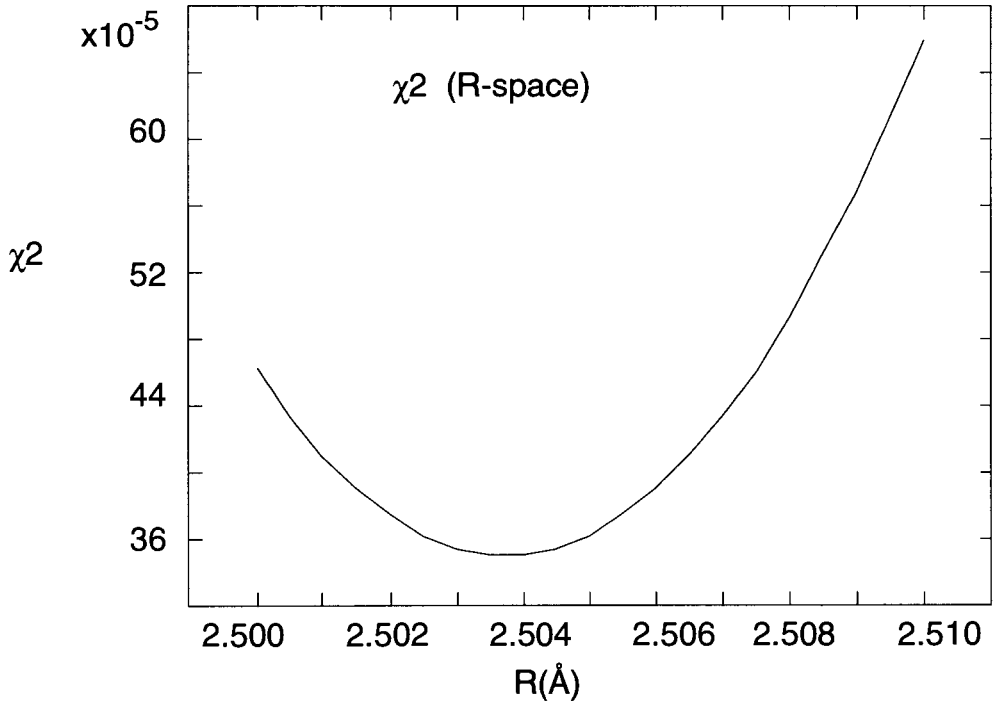

Figure A.8. χ^2 plot of R_1 showing the region from 2.50 to 2.51Å.

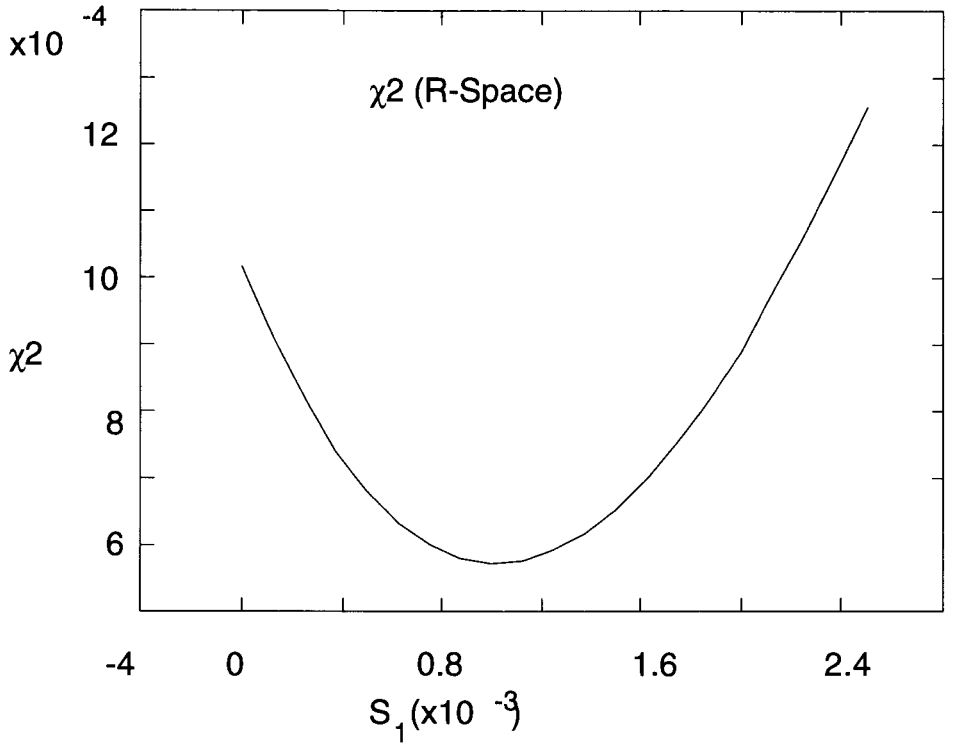

Figure A.9. χ^2 plot of S_1 showing the region from 0 to 2.4×10^{-3}.

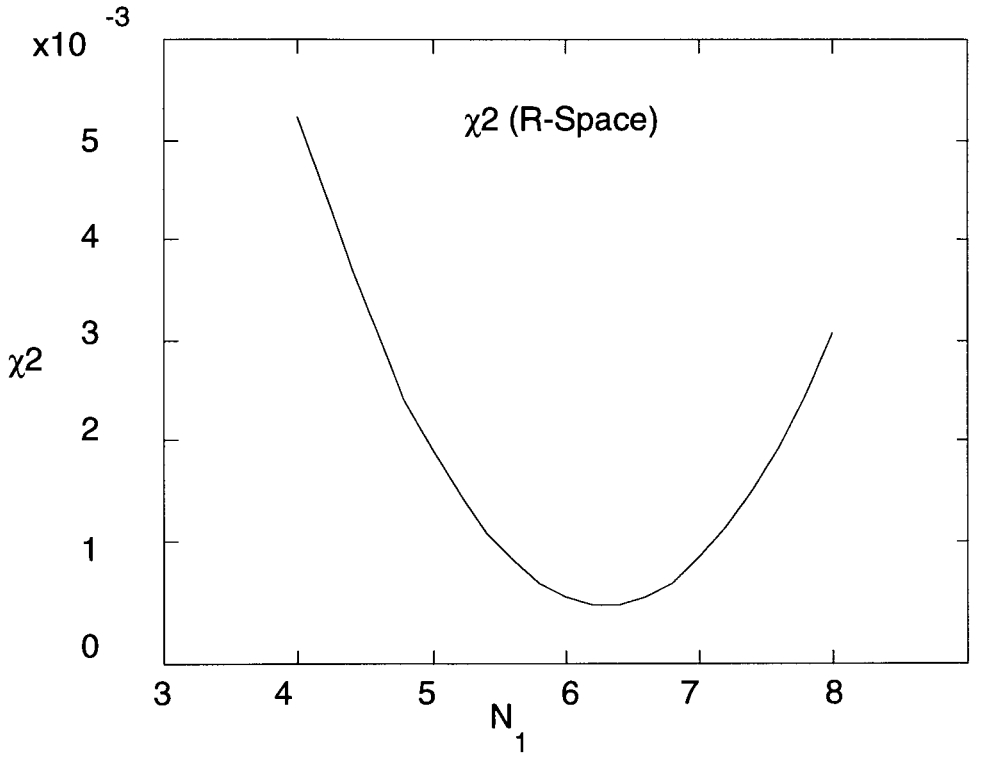

Figure A.10. χ^2 plot of $S_0^2 \times N_1$ showing the region from 4 to 8.

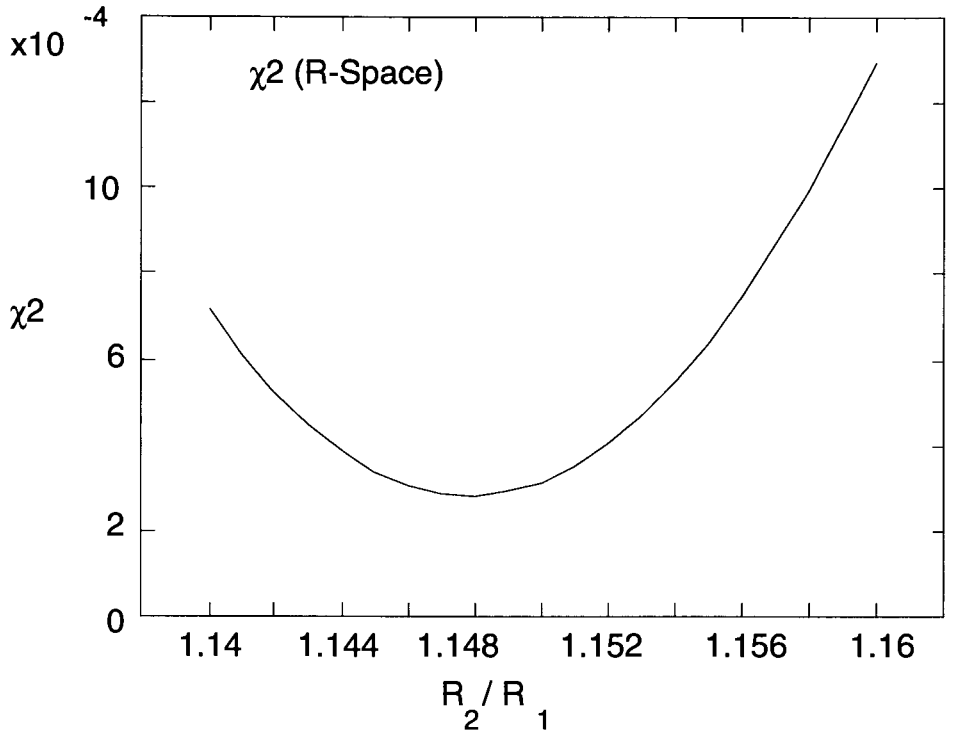

Figure A.11. χ^2 plot of R_2/R_1 showing the region from 1.14 to 1.16.

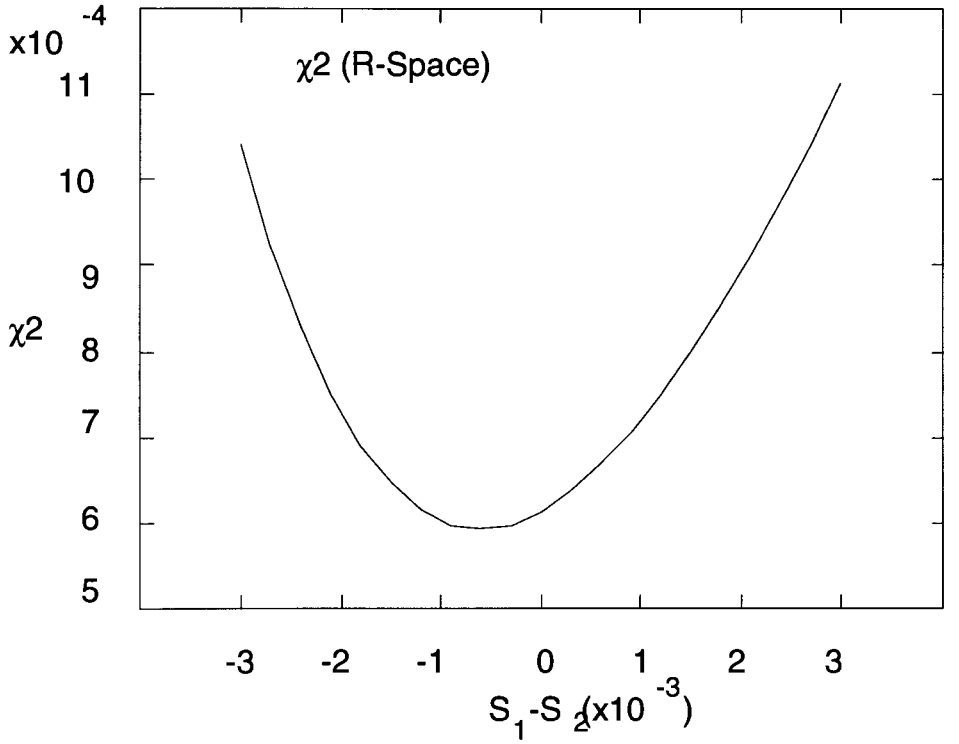

Figure A.12. χ^2 plot of S_2-S_1 showing the region from -3.0 to 3.0.

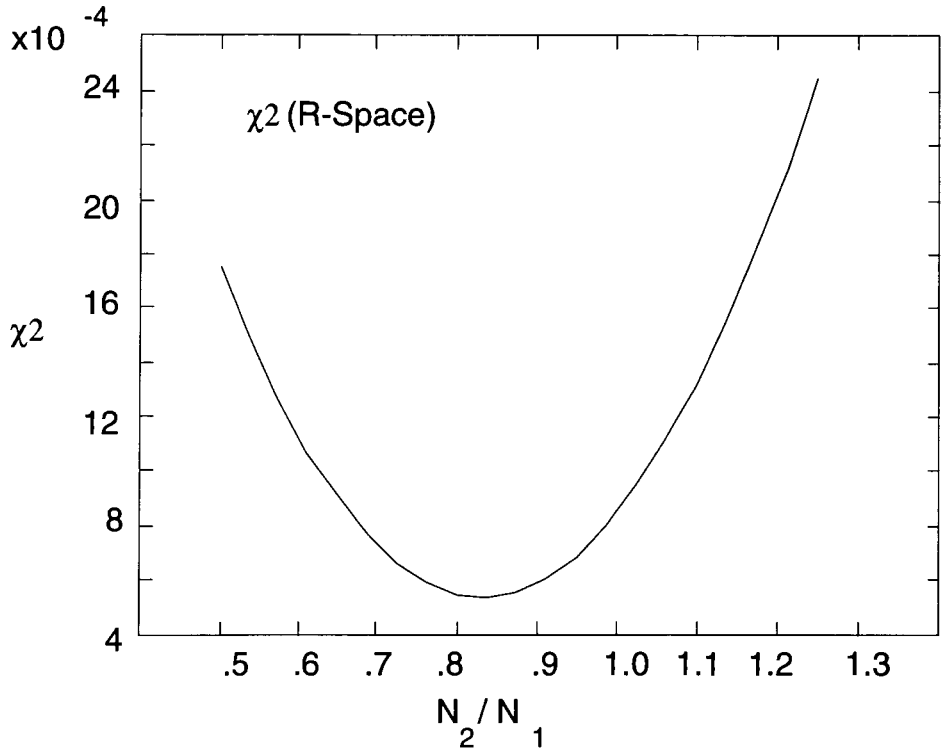

Figure A.13. χ^2 plot of N_2/N_1 showing the region from 0.5 to 1.3.

It should be noted that the program will not allow the other parameters to be varied while examining the χ^2 of the ratios of R_2 to R_1, as well as that of N_2 to N_1, therefore no real absolute values for the minima are available for these parameters (Fig. A.11, A.13). The graphs obtained while varying the ratios and keeping all other parameters fixed are given for reference only. It is of course possible that the minimum shown on them will correspond to an absolute minimum, though it may prove to be a local one. The following minima, given in Table A.4, were obtained while all other parameters varied. The asymmetry terms have minima within 10% of their calculated values and were therefore fixed at these values and will be given in italics in the tables from this point on.

Table A.4. Minima of fit parameters for a BCC two shell model from 1.85 to 13.70 $Å^{-1}$, and over an R-space region from 0.932 to 3.01Å.

R_j(Å)	N_j	$C_{3j}(x10^{-3})$ ($Å^3$)	$S_i(Å^2)$	Δ(eV)
2.504	7.5	*0.0227*	1.0	6.6
2.877	6.25	*0.0342*	-0.75	6.6

While holding the other parameters fixed it is possible to obtain minima for the ratio of the radii, 1.149, and the difference between the σ_j^2 for the two shells (S_2-S_1=-0.75). Though the precision of these values is doubtful, as they are heavily constrained, they nevertheless can guide our further choices. The high value of N_2/N_1 (=0.83) is in part due to compensation for the lack of amplitude at the high-R end of the spectra.

Moving all the parameters to the values given in Table A.4, with the result shown in Fig. A.14, gives a fit that is one order of magnitude worse (χ^2=0.95x10^{-3}) than that shown in Fig. A.6 (χ^2=0.7x10^{-4}).

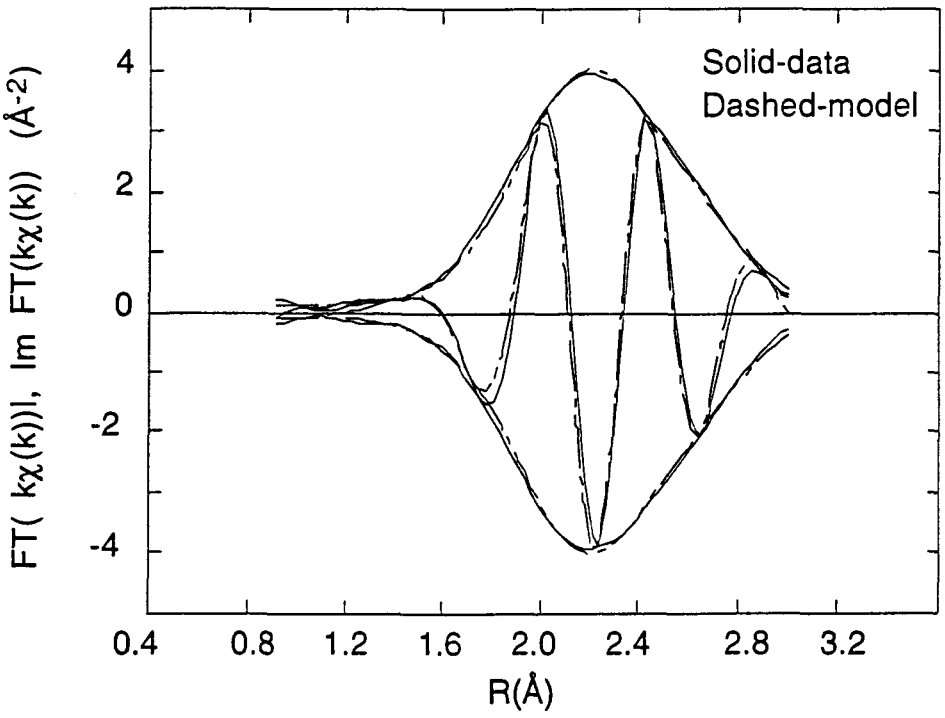

Figure A.14. Fit of Cr foil using the minima of the $\chi(k)$ outlined in Table 4. The solid line is the data and the dashed line represents the trial fit. The window function, and the R- and k-space ranges are the same as in Fig. A.1. The magnitude of the FT is the envelope, and the Imaginary part is the oscillatory part.

Starting from the values used in Fig. A.14, it is possible to obtain a fit of good quality (ie $\chi^2<0.5\times10^{-4}$) where all the parameters, aside from N_2, correspond well to their crystallographic values.

Though the sum of the coordination numbers is within 10% of that for a BCC structure (14), the value for the second shell continues to exceed $0.75\times N_1$ in order to compensate the lack of amplitude in the model in the high-R region.

If the ratio of N_2/N_1 is fixed to the crystallographic value then varying the position of the second shell fails to make up for the

amplitude which is lacking, and vice versa. When the radii are badly chosen (R_2 larger to compensate the lack of intensity in that region) there remains a problem in the fit of the Imaginary part of the spectrum. This problem cannot be fixed by simply changing the energy shift without moving R_1 more than 0.02Å from its known value.

Attempting to fit the high-R region by varying σ_2^2 gives a ratio of N_2/N_1 of 1.09, therefore that technique is rejected. An alternate technique of varying σ_2^2 was tried, with R_2 and N_2/N_1 also changing. This led to a value of N_2/N_1 of 1.00, and was therefore also rejected.

It seems at this point that any further improvements upon the quality of fit will necessitate the addition of multiple scattering (MS) paths which will add intensity in the high-R region where it is needed.

A.1.3. First and Second Nearest Neighbours: Multiple Scattering

The whole procedure outlined above was repeated while fitting in k-space. It proved necessary to add MS paths in order to fit the low k-region of the spectrum. The MS paths were seen to have intensity in the range from 1 to 4Å^{-1}, the area which fit badly with only the two first shells included in the model.

The multiple scattering paths of importance in this region of a BCC structure are the 48 triangular paths from the absorber to the body center, to a corner and back to the absorber along the edge of the cube, or the 24 triangular paths from the absorber to the body center, then across to another body center in a contiguous cell, and returning to the absorber along the body diagonal. These paths have an effective scattering length of $R=(2R_1+R_2)/2$, which, in the case of crystallographic BCC Cr, would be 3.9395Å. Figure A.15 shows a good fit of the Cr foil without the presence of the multiple scattering paths, whereas Fig. A.16 shows the result when the triangular paths are added to the model. The only differences are seen in the high R end of the spectrum where Fig. A.16 shows more intensity in the model than in the data. The fit parameters are given in Table A.5.

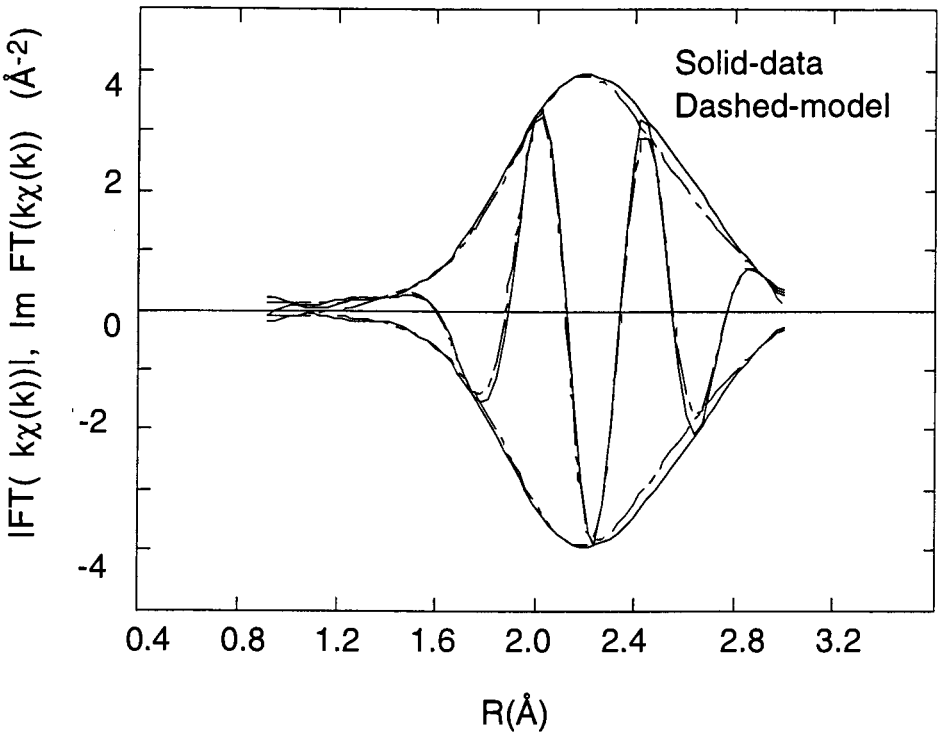

Figure A.15. Fit of Cr foil using the best fit parameters without multiple scattering paths. The parameters are in Table A.5. The solid line is the data and the dashed line represents the trial fit. The window function, and the R- and k-space ranges are the same as in Fig. A.1. The magnitude of the FT is the envelope, and the Imaginary part is the oscillatory part.

Table A.5. Fit parameters for Fig. A.15 (first two shells only) and Fig. A.16 (all 4 shells.)

R_j(Å)	N_j	$C_{3j}(x10^{-3})$ (Å^3)	S_i(Å^2)	Δ(eV)
2.504	8.0	*0.0227*	1.5	6.6
2.887	6.0	*0.0342*	-0.75	6.6
3.9387	24.0	*0.0934*	6.0	6.6
3.9387	48.0	*0.0934*	6.0	6.6

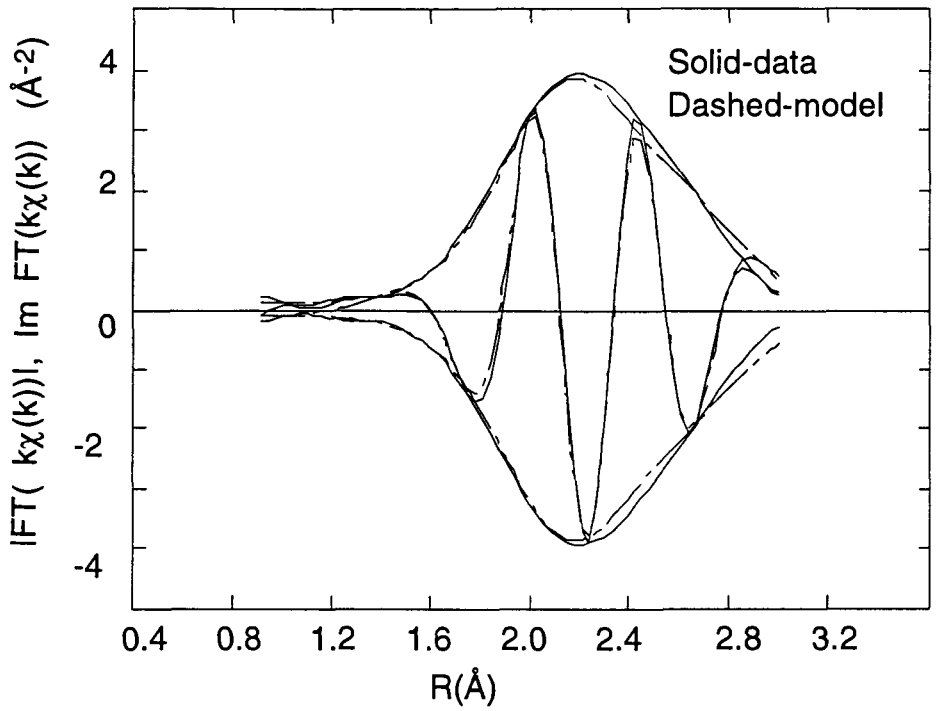

Figure A.16. Fit of Cr foil with parameters as in Fig. A. 15, but including the multiple scattering paths. The solid line is the data and the dashed line represents the trial fit. The window function, and the R- and k-space ranges are the same as in Fig. A.1. The magnitude of the FT is the envelope, and the Imaginary part is the oscillatory part.

Fitting the data with the parameters of Table A.5 as a starting point, and allowing the R values of the multiple scattering paths to vary as well as the parameters S_1, R_1, ΔE_0, and R_2/R_1, gives the result shown in Fig. A.17, with the final fit parameters given in Table A.6.

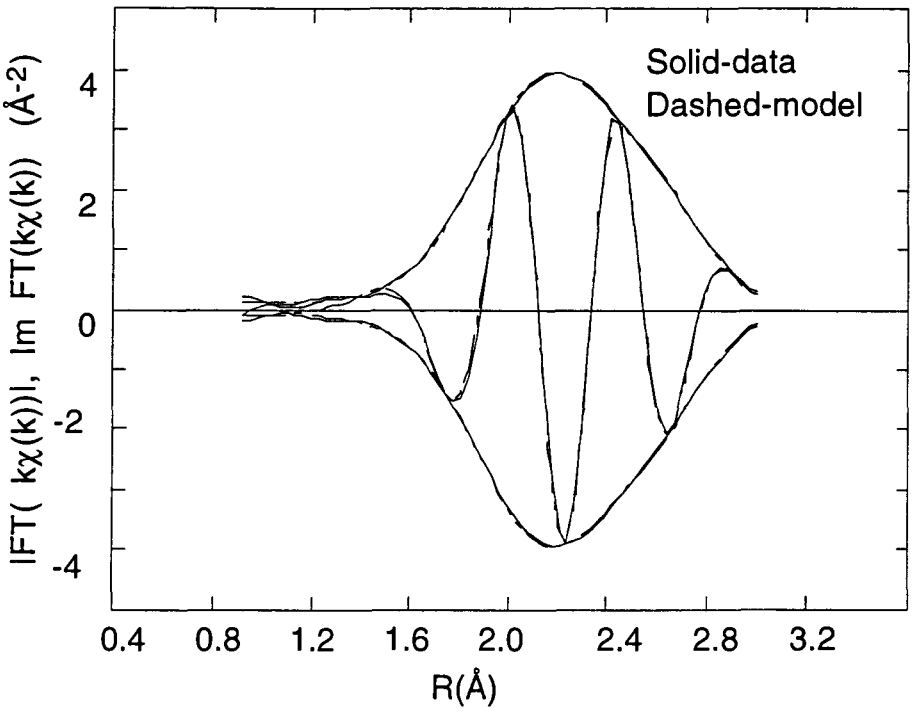

Figure A.17. Fit of Cr foil including multiple scattering paths. The results of the fit are given in Table A.6. The solid line is the data and the dashed line represents the trial fit. The window function, and the R- and k-space ranges are the same as in Fig. A.1. The magnitude of the FT is the envelope, and the Imaginary part is the oscillatory part.

Table A.6. Fit parameters for Cr foil for the fit shown in Fig. A.17. S_0^2 is then 0.81 for Cr.

R_j(Å)	N_j	$C_{3j}(x10^{-3})$ (Å^3)	S_i(Å^2)	Δ(eV)
2.506±0.1	8.0±0.5	*0.0227*	0.8±0.4	5.5±0.6
2.881±0.1	6.0±0.5	*0.0342*	-0.75±0.4	5.5±0.6
3.95±0.02	24.0±1.5	*0.0934*	6.0±1.0	5.5±0.6
3.94±0.02	48.0±3.0	*0.0934*	6.0±1.0	5.5±0.6

The σ_j^2 terms have the following values, based on the S_j values of the fit: for the first and second shell they are 5.85 and $6.65 \times 10^{-3} Å^2$; for the triangular paths the cumulative value is $13.4 \times 10^{-3} Å^2$. They are within 15% of those of Fe [4]. The values of the σ_j^2 calculated from their Debye temperatures are, for the first two shells of Fe, 5.10 and 5.92 $\times 10^{-3} Å^2$ for Θ_D=420, and for Cr, 4.28 and $4.97 \times 10^{-3} Å^2$ for Θ_D=485. The measured values for the BCC Cr foil are therefore within 30% of those calculated using FEFF6.10. The values of R_1 and R_2 were -0.02% and -0.40% from the associated crystallographic values. Note that the corrections to the radii due to the limited mean free path of the photoelectrons in the crystal were not removed (ie the term $-4k\sigma_j^2(1/R_j+1/\lambda)$ in Equation 2.11). For Cr this correction is 0.009Å, which represents roughly 0.4% of the radii's values. The result of the least-squares fitting gives values of the radii for the first two shells which are therefore 2.497 and 2.871Å. The asymmetric terms (C_3 terms) were of the order of magnitude of their theoretical values when they were allowed to vary.

In the above analysis knowledge of the errors on each parameter was necessary in order to deem any result to be reasonable or not. Errors were found by finding the range of values of the parameter necessary in order to double the residual sum of squares.

The above technique for fitting was used for a structure which is known to be close to the ideal crystallographic BCC. If the radii are thought to be very different from the ideal values many iterations of the above method must be made in order to find the

minima, and to ensure that they are all absolute, as opposed to simply local. The same scheme can be used to fit higher shells once the first two have been accurately fit over a reasonable range, and prior knowledge of a reliable standard for the amplitude and phases has been recorded.

References

Chapter I

[1] G.A. Prinz, J. Magn. Magn. Mater. **100**, 469(1991).

[2] B. Heinrich, Z. Celinski, J.F. Cochran, W.B. Muir, J. Rudd, Q.M. Zhong, A.S. Arrott, K. Myrtle, J. Kirschner, Phys. Rev. Lett. **64**, 673(1990).

[3] A.P. Payne, B.M. Lairson, S. Brennan, B.J. Daniels, N.M. Rensing, B.M. Clemens, Phys. Rev. **B47**, 16064(1993).

[4] B.C. Bolding, E.A. Carter, Surf. Sci. **268**, 142(1992).

[5] F.C. Frank, J.M. van der Merwe, Proc. R. Soc. **A198**, 205(1949).

[6] I. Markov, A. Milchen, Surf. Sci. **136**, 503(1984), ibid, 509(1984),and ibid, Surf. Sci. **145**, 313(1984).

[7] K.N. Tu, J.W. Mayer, L.C. Feldman, *Electronic Thin Film Science for Electrical Engineers and Materials Scientists*, Mac Millan, New York, 1992.

[8] B. Heinrich, Z. Celinski, L.X. Liao, M.From, J.F. Cochran, J. Appl. Phys. **75**, 6181(1994), M. From, L.X. Liao, J.F. Cochran, B. Heinrich, ibid, 6187(1994), A. Fert, P. Grunberg, A. Barthelemy, F. Petroff, W. Zinn, J. Magn. Magn. Mater. **140-144**, 1(1995).

[9] P. Grunberg, R. Schreiber, Y. Pang, M.B. Brodsky, P. Sowers, Phys. Rev. Lett.**57**, 2442(1986), and C. Carbone, S.F. Alvarado, Phys. Rev. **B36**, 2433(1987).

[10] G. Binasch, P. Grunberg, F. Saurenbach, W. Zinn, Phys. Rev. **B39**, 4828(1989), and M.N. Baibich, J.M. Broto, A. Fert, F. Nguyen van Dau, P. Petroff, P.Etienne, G. Creuzet, A. Friederich, J. Chazelas, Phys. Rev. Lett. **61**, 2472(1988).

[11] J.A. Brug, T.C. Anthony, J.H. Nickel, Mater. Res. Soc. Bull. **21**, 23(1996).

[12] S.S.P. Parkin, N. More, K.P. Roche, Phys. Rev. Lett. **64**, 2304(1990).

[13] G.A. Prinz, Phys. Today **48**, 58(1995).

[14] A.S. Arrott, *Ultrathin Magnetic Structures: An Introduction to the Electronic, Magnetic and Structural Properties*, J.A.C. Bland, B.Heinrich (eds), Springer-Verlag, 1994, and S.T. Purcell, B.Heinrich, A.S. Arrott, Phys. Rev. B **35**, 6458(1987).

[15] J.A. Stroscio, D.T. Pierce, R.J. Celotta, MRS Proceedings, April, 1993, and J.A. Stroscio, D.T. Pierce, R.A. Cragoset, Phys. Rev. Lett.**70**, 3615(1993).

[16] B. Heinrich, Z. Celinski, J.F. Cochran, A.S. Arrott, K. Myrtle, S.T Purcell, Phys. Rev. **B47**, 5077(1993), and B. Heinrich, J.F. Cochran, Advances in Physics **42**, 523(1993).

[17] B.M. Lairson, A.P. Payne, S. Brennan, N.M. Rensing, B.J. Daniels, B.M. Clemens, J. Appl. Phys. **78**, 4449(1995).

[18] Z.Q. Wang, S.H. Lu, Y.S. Li, F. Jona, P.M. Marcus, Phys. Rev. **B35**, 9322(1987).

[19] Y. Huai, R.W. Cochrane, M. Sutton, J. Appl. Phys. **73**, 5530(1993), and Y. Huai, R.W. Cochrane, X. Bian, M. Sutton, J. Appl. Phys. **75**, 6554(1994).

[20] W.F. Egelhoff, Jr., *Ultrathin Magnetic Structures: An Introduction to the Electronic, Magnetic and Structural Properties*, J.A.C. Bland, B.Heinrich (eds), Springer-Verlag, 1994.

[21] H. Glatzel, T. Fauster, B.M.V. Scherzer, V. Dose, Surf. Sci. **254**, 58(1991).

[22] S.M. Heald, H. Chen, G.M. Lamble, Physica **B 158**, 309(1989).

[23] P. Roubin , D. Chandesris, G. Rossi, J. Lecante, M.C. Desjonqueres, G. Treglia, Phys. Rev. Lett. **56**, 1272(1986), and H. Magnan, D. Chandesris, B. Villtte, O. Heckman, J. Lecante, Phys. Rev. Lett. **67**, 859(1991), and P. LeFevre, H. Magnan, O. Heckmann, V. Briois, D. Chandesris, Phys. Rev. **B52**, 11462(1995).

[24] Y.U. Idzerda, B.T. Jonker, W.T. Elam, G.A. Prinz, J.Vac.Sci. Technol. **A8**, 1572(1990).

[25] D.T. Jiang, E.D. Crozier, B. Heinrich, Phys. Rev.**B 44**, 6401(1991), and D.T. Jiang, N. Alberding, A.J. Seary, B. Heinrich, E.D. Crozier, Physica **B158**, 662(1989), and D.T. Jiang, N. Alberding, A.J. Seary, E.D. Crozier, J. de Phys. **47**, (**C 8**), 861(1986).

[26] Y.R. Bonin, Ph. D. Thesis, Simon Fraser University, December 1993.

[27] S. Turchini, M.G. Proietti, F. Martelli, L. Alagna, T. Prosperi, M.G. Simeone, J. Garcia, Jpn. J. Appl. Phys. **32**, 419(1993).

Chapter II

[1] B.K. Teo, *EXAFS: Basic Principles and Data Analysis*, Springer Verlag, 1986.

[2] C. Cohen-Tannoudji, B. Diu, F. Laloë, *Quantum Mechanics*, Volume II, John Wiley and Sons, New York, 1977.

[3] E.A. Stern, *X-Ray Absorption: Principles, apllications, techniques of EXAFS, SEXAFS and XANES*, D.C. Koningsberger, R. Prins (Eds.), Chemical Analysis, Vol.**92**, Wiley, New York, 1988.

[4] J.J. Rehr, R.C. Albers, Phys.Rev. **B41**, 8139(1990), and S.I. Zabinsky, J.J. Rehr, A. Andukinov, R.C. Albers, M.J. Eller, Phys. Rev. **B52**, 2995(1995).

[5] E.D. Crozier, Physica **B 208&209**, 330(1995).

[6] G. Bunker, Nucl. Inst. and Met. **207**, 437(1983).

[7] E.D. Crozier, *X-Ray Absorption: Principles, apllications, techniques of EXAFS, SEXAFS and XANES*, D.C. Koningsberger, R. Prins (Eds.), Chemical Analysis, Vol.**92**, Wiley, New York, 1988.

[8] K.R. Bauschpiess, Jpn. J. Appl. Phys. Vol. **32**, 131(1993).

[9] M. Newville, P. Livins, Y. Jacoby, J.J. Rehr, E.A. Stern, Phys. Rev. **B47**, 14126(1993).

[10] J.W. Cook, Jr., D.E. Sayers, J. Appl. Phys. **52**, 5924(1981).

[11] E.A. Stern, P.Livins, Z. Zhang, Phys. Rev. **B43**, 8850(1991).

[12] E.D. Crozier, A.J. Seary, Can. J. Phys. **58**, 1368(1980).

[13] B. Lengeler, P.Eisenberger, Phys. Rev.**B21**, 4507(1980).

[14] E.O. Brigham, *The Fast Fourier Transform*, Prentice-Hall, Englewood Cliffs, N.J.

[15] E. Sevillano, H. Meuth, J.J. Rehr, Physical Review **B 20**, 4908(1979).

[16] J.Stohr, *X-Ray Absorption: Principles, apllications, techniques of EXAFS, SEXAFS and XANES*, D.C. Koningsberger, R. Prins (Eds.), Chemical Analysis, Vol.**92**, Wiley, New York, 1988.

[17] L.Troger, T. Yokohama, D. Arvanitis, T. Leder, M. Tischer, K. Baberschke, Phys. Rev. B. **49**, 888(1994).

[18] T.Yokoyama, S. Kimoto, T. Ohta, Jpn. J. Appl. Phys.**28**, L851(1989).

[19] D.E. Sayers, B.A. Bunker, *X-Ray Absorption: Principles, apllications, techniques of EXAFS, SEXAFS and XANES*, D.C. Koningsberger, R. Prins (Eds.), Chemical Analysis, Vol.**92**, Wiley, New York, 1988.

Chapter III

[1] Alumina from Micro Mettalurgical, Richmond Hill, Ontario, Canada.
Nylon pads from Micro Mettalurgical, Richmond Hill, Ontario, Canada.

[2] R. L. Lyles, S.J. Rothman and W. Jager, Metallography **11**(3),361(1978).

[3] R.W.G. Wyckoff, *Crystal Structures*, Volume 1 Second Edition, Interscience Publishers, John Willey & Sons, New York, 1965.

[4] Z. Celinski, Ph. D. Thesis, Simon Fraser University, 1992.

[5] M. Z. Kowalewski, M. Sc. Thesis, Simon Fraser University, 1993.

[6] P.J. Schurer, Z. Celinski, B. Heinrich, Phys. Rev. **B48**, 2577(1993).

[7] Y.R. Bonin, Ph. D. Thesis, Simon Fraser University, December, 1993.

[8] A.P. Payne, B.M. Lairson, S. Brennan, Physical Review B **47,** 16064(1993).

[9] C. Krembel, M.C. Hanf, J.C. Peruchetti, D. Bolmont and G. Gewinner, Journ. Magn. Magn. Mat. **119,** 115(1993), and D. Rouyer, C. Krembel, M.C. Hanf, D. Bolmont and G. Gewinner, Surf. Sci. **287&289**, 935(1993), and D. Rouyer, C. Krembel, M.C. Hanf, J.C. Peruchetti, D. Bolmont and G. Gewinner, Surf.Sci.**322**, 34(1995).

[10] J. Gerkema and A. R. Miedema, Surf. Sci.**124**,(1983)351.

[11] C. Krembel, M.C. Hanf, J.C. Peruchetti, D. Bolmont, G.Gewinner, J. Vac. Sci. Technol. **A10**, 3325(1992).

[12] A. Zangwill, *Physics at Surfaces*, Cambridge University Press, 1988.

[13] J.Y. Tsao, *Materials Fundamentals of Molecular Beam Epitaxy*, Academic Press,1992, S.T. Purcell, B. Heinrich, A.S. Arrott, Phys. Rev. **B 35**, 6458(1987).

[14] B. Heinrich, Z. Celinski, J.F. Cochran,W.B. Muir, J. Rudd, Q.M. Zhong, A.S. Arrott, K. Myrtle, J. Kirschner, Phys. Rev. Lett. **64**, 673(1990).

[15] M.K. Mc Manus, M. Sc. Thesis, Université de Montréal, 1993.

[16] R. Morel, Ph. D. Thesis, Université de Montréal, 1991.

[17] A.R. Miedema, Philips Tech. Rev. **36**, 217(1976).

[18] F.A. Shunk, *Constitution of Binary Alloys*, 2nd Supplement. Mc Graw Hill, New York, 1969, p.495.

[19] Y. Huai, R.W. Cochrane, M. Sutton, J. Appl. Phys. **73**, 5530(1993), and Y. Huai, R.W. Cochrane, X. Bian, M. Sutton, J. Appl. Phys. **75**, 6554(1994).

Chapter IV

[1] D.T. Jiang, N. Alberding, A.J. Seary, E.D. Crozier, Rev. Sci. Instrum. **59**, 60(1988).

[2] D.T. Jiang, PhD Thesis, Simon Fraser University, May 1992.

[3] S.M. Heald, Rev. Sci. Instrum. **63**, 873(1992), H. Chen, S.M. Heald, J. Appl. Phys. **73**, 2467(1993).

[4] D.T. Jiang, E.D. Crozier, Nuclear Instrum. and Methods in Phys. Res. **A294**, 666(1990).

[5] K.H. Kim, W.T. Elam, E.F. Skelton, J.P. Kirkland, R.A. Neisler, Phys. Rev.**B42**, 10724(1990)

[6] B.K. Agarwal, *X-Ray Spectroscopy: An Introduction*, Springer Series in Optical Sciences, 2nd Ed, 1991.

[7] D.T. Jiang, Ph.D. Thesis, Simon Fraser University, May 1992.

[8] D.T. Cromer, D. Liberman, J. Chem. Phys. **53**, 1891(1970).

[9] ibid, Acta. Cryst. **A31**, 267(1981).

[10] D.T. Cromer, J. Appl. Cryst. **16**, 437(1983).

[11] D.T. Jiang, E.D. Crozier, Proceedings XAFS IX, submitted to Journ. Phys. Colloques, Sept. 1996.

[12] O. Heckmann, H. Magnan, P. leFevre, D. Chandesris, J.J. Rehr, Surf. Sci. **312**, 62(1994).

Chapter V

[1] K. R. Bauchspiess, Ph.D. Thesis, Simon Fraser University, February 1991.

[2] E.D. Crozier, Physica **B 158**, 14(1988).

[3] B. K. Teo, *EXAFS: Basic Principles and Data Analysis*, Springer Verlag, Berlin, 1986, p.151

[4] Z. Celinski, Ph.D. Thesis, Simon Fraser University, May 1992.

[5] E.A. Stern, M. Newville, B. Ravel, Y. Yacoby, D. Haskel, Physica **B 208&209**, 117(1995).

[6] E.D. Crozier, Physica **B 208&209**, 330 (1995).

[7] E.D. Crozier, A.J. Seary, M.K. Mc Manus, D.T. Jiang, Proceedings XAFS IX, submitted to Journ. Phys. (Colloques), Sept. 1996.

[8] G. Martens, P. Rabe, N. Schwentner, A. Werner, Phys. Rev. Lett. **39**, 1411(1977).

[9] J.J. Rehr, R.C. Albers, Phys. Rev. **B41**, 8139(1990), and S.I. Zabinsky, J.J. Rehr, A.Andukinov, R.C. Alber, M.J. Eller, Phys. Rev. **B52**, 2995(1995).

Chapter VI

[1] R.W.G. Wyckoff, *Crystal Structures*, Volume 1, Second Edition, Interscience Publishers, John Willey & Sons, New York, 1965.

Chapter VII

[1] K.N. Tu, J.W. Mayer, L.C. Feldman, *Electronic Thin Film Science for Electrical Engineers and Materials Scientists*, Mac Millan, New York (1992).

[2] E. Fawcett, H.L. Alberts, V. Yu. Galkin, D.R. Noakes, J.V. Yakhmi, Rev. Mod. Phys. **66**, 25(1994).

[3] B. Heinrich, Private Communication.

Appendix A

[1] K.R. Bauchpiess, Jpn. J. Appl. Phys. Vol.**32**, 131(1993).

[2] S.I. Zabinsky, J.J. Rehr, A. Ankudinov, R.C. Albers, M.J. Eller, Phys. Rev. **B52**, 2995(1995).

[3] R.W.G. Wyckoff, *Crystal Structures*, John Wiley and Sons, 1963, p.16.

[4] E. Sevillano, H. Meuth, J.J. Rehr, Physical Review **B20**, 4908(1979).

[5] E.D. Crozier, Physica **B 208&209**, 330(1995), and L. Troger, T. Yokohama, D. Arvanitis, T. Leder, M. Tischer, K. Baberschke, Phys. Rev. **B 49**, 888(1994), and T. Yokohama, S. Kimoto, T. Ohta, Jpn. J. Appl. Phys. **28**, L851(1989).

[6] G. Beni, P.A. Lee, P.M. Platzman, Phys. Rev. **B13**, 5170(1979).